Working Group 3 - Deliverable 3.2

Development of experimental prototypes and field trials for the evaluation of proposed solutions under different environmental conditions

Main contributors: Stanislav Zvanovec, Beatriz Ortega, Zabih Ghassemlooy, Xiaodan Pang, Shivani Rajendra Teli, and Vicente Matus

1. Introduction

The continuous research and application of optical wireless communications (OWC), including free space optics (FSO), optical camera communications (OCC) and visible light communications (VLC) for mid-range links, have brought several new prototypes as well a number of technologies have been tested under environmental conditions.

This deliverable aims to present the recent advances in prototypes and field trials proposed for such systems by several collaborations between research groups from different partners especially for vehicular communications, radio over FSO or OCC sensors in COST action CA19111 NEWFOCUS.

2. Free Space Optical Systems

2.1. FSO System with Polar Codes

As part of linear codes, polar codes, which are defined using a generator matrix in a recursive manner, offer lower encoding and decoding complexity (i.e., O(Nlog2(N)), where N is the code length [1] and O is the notation indicating the performance of the algorithm, and have been used in several applications including relay transmission, multiple access channels, quantum key distributions [1,2], etc. In the context of FSO communications, the performance of polar codes over the turbulence channel was analysed in [3]. The authors have proposed a channel state information (CSI) evaluation scheme that is utilised to calculate the log-likelihood ratio (LLR) using a 2000-bit pilot sequence, which is the soft input to the polar decoder. It was experimentally determined that, under weak turbulence, polar codes performed better than low density parity check (LDPC) codes, and under moderate and strong turbulence using Monte-Carlo simulations, polar codes outperformed LDPC. In [4], the performance of a deep learning-based neural network is investigated under the turbulence regime. Under fixed turbulence conditions, the decoder performance is reported to be stable. In [5], the concept of the polar coded multiple input multiple output (MIMO) FSO communications system is introduced to combat turbulence induced fading. The MIMO-polar coded system using a successive cancellation list decoder (SCL) offered an improved net coding gain when compared with LDPC with and without spatially correlated fading scenarios. For finite code lengths, LDPC and turbo codes perform better than polar codes, for which several decoding schemes [6,7] have been proposed to improve the error correcting performance at the cost of increased complexity. In this work, we determine the optimum code-rate R for the scintillation indices σ_I^2 of 0.12, 0.2, and 0.31 for the SC decoder and compare its performance with the SCL decoder under weak turbulence in terms of the bit error rate (BER) with the assumption that the channel state information at the receiver (Rx) is not known. As shown in Fig. 2.1(a), a random message bit sequence $\boldsymbol{m}$ in the non-return to zero OOK format is applied to the polar code encoder to generate a fixed length codeword $\boldsymbol{d}$ with N of 1024-bits for intensity modulation of the optical source. The channel follows log-normal and GG distributions for $\sigma_I^2 \leq 0.3$ and > 0.3, respectively. Following transmission over the free space channel, the codeword $\boldsymbol{y}$ is received at the optical Rx. Using $y(t) = h(t) * x(t) + n(t)$, the log-likelihood ratio (LLR) of the received signal $\boldsymbol{y}$ is computed and decoded using the SC/SCL decoder to obtain $\boldsymbol{m_{est}}$. Although narrow transmit beams are preferred in FSO links, for short-range FSO links, wide divergence angle

light sources are highly desirable to ease the alignment requirement and therefore compensate for the pointing loss at the cost of increased geometric loss [8]. Typically, the beam divergence is in the range of 2-10 mrad for the non-tracking systems, which translates to a beam spot of 2-10 m for a 1 km link. In this work, we have assumed a beam with a wide divergence for ground-to-train communications as described in [9], which is practical, therefore offsetting the pointing loss at the cost of increased geometric loss [10]. However, for a point-to-point long range FSO link, misalignment must be considered.
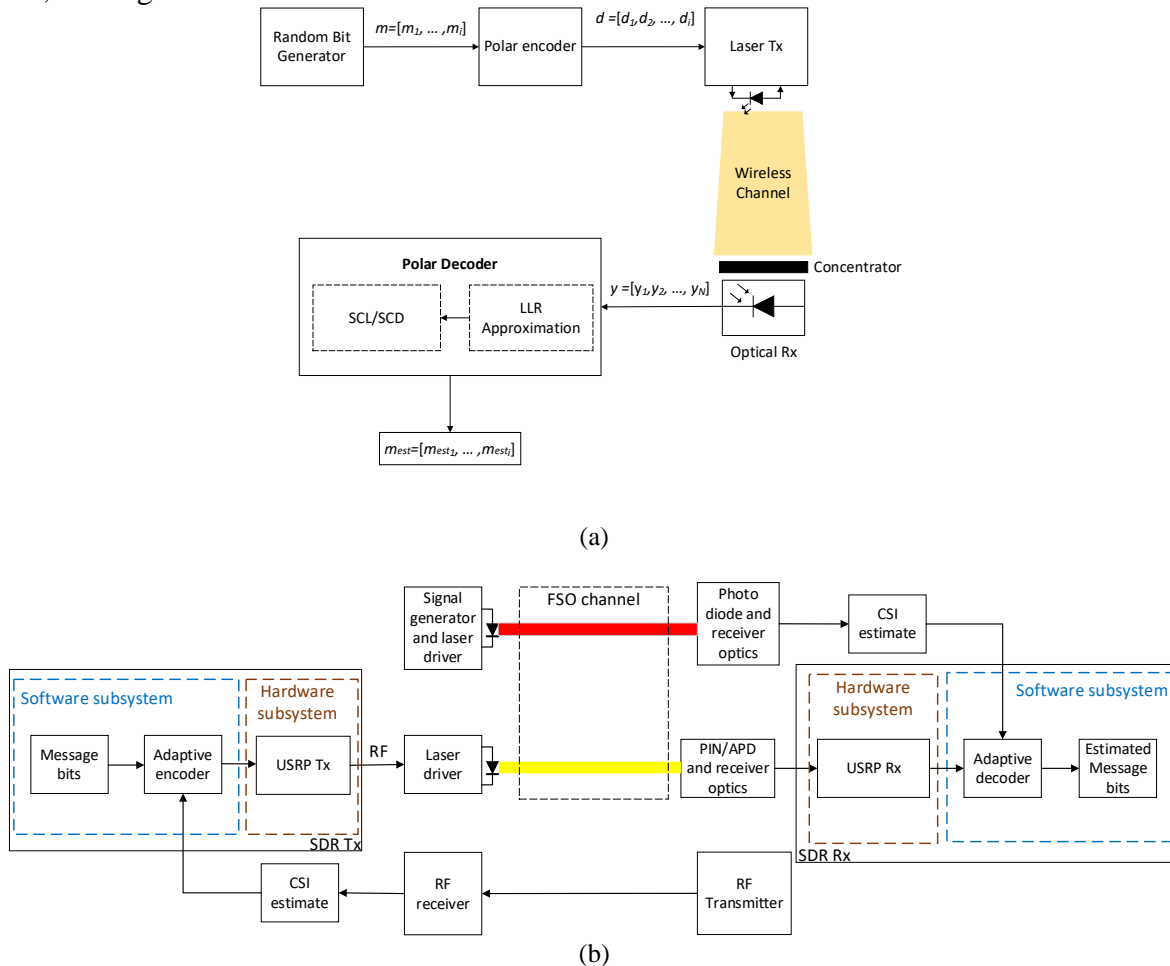

(a)

(b)

Fig. 2.1. System block diagram for: (a) the proposed system, and (b) adaptive coding using SDR.

From a practical system's perspective, adaptive coding could be considered as a prudent approach to mitigate turbulence/scintillation experienced by the FSO link. The practical implementation of the proposed system can be carried out using purpose-built modules or FPGA, which will involve using the radio frequency (RF) link for the feedback signal on channel state information. Alternatively, the adaptive coding part could be readily implemented using software defined radio (SDR), see Fig. 2.2. In the SDR-based transmitter (Tx), the message bits are encoded using an adaptive Polar encoder, which adjusts the code rate based on the strength of the turbulence estimated by the CSI estimate block. The CSI is estimated by determining the variance (scintillation index) of the fluctuating optical intensity of a modulated red laser transmitted from the Rx side. The resulting signal from the adaptive encoder is fed to the USRP Tx which is modulated onto an RF carrier. The RF carrier is directly modulated and transmitted across the FSO channel using a laser driver.

Results - The objective is to determine the optimum code rate for the weak turbulence regime, which maintains the BER at 10^{-9} with the 95% confidence limit for each scintillation index mentioned in Table 1. The OOK data stream, polar encoder, decoder, and turbulence channel are implemented in C++. Using Monte-Carlo simulation, the optimum code rate under the weak and moderate turbulence regimes was determined utilizing the system parameters provided in Table 3.1, and the results of the simulation are described in Table 3.2.

<table>
<tr><td colspan="2" align="center">Table 3.1 System parameters.</td></tr>
<tr><td align="center">PARAMETER</td><td align="center">VALUE</td></tr>
<tr><td>Codeword length</td><td align="center">1024</td></tr>
<tr><td>Iteration</td><td align="center">$\dfrac{3 \times 10^6}{R}$</td></tr>
<tr><td>N_{bits}</td><td align="center">3×10^9</td></tr>
<tr><td>BER confidence level</td><td align="center">95%</td></tr>
<tr><td>Target BER</td><td align="center">10^{-9}</td></tr>
<tr><td>Scintillation index σ_I^2</td><td align="center">0.12, 0.2, 0.31</td></tr>
</table>

Table 3.2 Results of Monte-Carlo simulation.

σ_I^2	MESSAGE BITS TRANSMITTED	MSG BITS/FRAME	R
0.12	3×10^9	615	0.6
0.2	3×10^9	345	0.33
0.31	3×10^9	209	0.2

In each iteration, 1024-bit codewords are generated by the polar encoder for a specific R and transmitted over a log-normal (LN)/ Gamma-Gamma (GG) turbulence channel for a range of scintillation indices provided in Table 1. The received bit stream is decoded and the BER is evaluated $\frac{3 \times 10^6}{R}$ times to estimate the BER with a 95% confidence level. To determine the optimum R for each scenario, an initial R of 0.5 was used. The simulation was terminated, and R was decremented by 0.1~0.05 once the simulation reached 100 errors. The decrement in R depends on the number of iterations needed to reach 100 errors. Note that for each trial and the error scenario, a total of N encoded bits were generated. If no errors were detected, R was incremented by 0.05. Based on Monte-Carlo simulation results, performance comparisons between SC and SCL decoders are demonstrated for $\sigma_I^2 = 0.12$, 0.2, and 0.31 in Figs. 2.2(a), (b), and (c), respectively. In all turbulence scenarios, SCL with cyclic redundancy check (CRC) is adopted with a list size of 4, a CRC length of 11 [11], and N of 1024. Also shown are the plots for the link with no coding and turbulence for reference. Under the turbulent condition, corruption of some bits allows for the message bits to be extracted from other uncorrupted bits. Because of this, the forward error correction (FEC) limit of 3.8×10^{-3} is achieved above a certain SNR level. This tendency is more pronounced in capacity achieving codes such as Polar codes. The error propagation problem is severe, with multiple bit errors occurring at lower SNR. At higher SNR, as the occurrence of bit errors is reduced and therefore the performance in terms of coding is improved, i.e., sharp fall in the BER plots for the links with coding, which is depicted in Fig. 2.2. In Fig. 2.2(a), for $\sigma_I^2 = 0.1$ the coding gain between uncoded OOK under turbulence with respect to SC decoder with $R = 0.6$ is 7 dB measured at the BER of 10^{-5}. The coding gain for the SC decoder with $R = 0.7$ is around 4 dB, which is 3 dB less than $R = 0.6$. SCL with $R = 0.6$ has improved performance with the coding gain of 6 dB, i.e., 2.5 dB improvement over the SC decoder for the same R measured at the BER of 10^{-5}. For $\sigma_I^2 = 0.2$, see Fig. 2.2(b), the coding gain of 10 dB is observed between uncoded OOK under turbulence and the SC decoder for $R = 0.33$. The SC decoder with $R = 0.5$ shows deteriorated performance compared with the case with $R = 0.33$ with a coding gain of 5 dB with respect to uncoded OOK under turbulence, 5 dB worse off than $R = 0.33$ as measured at the BER of 10^{-4}. The SCL decoder has an improved performance with a coding gain of 10.3 dB with respect to uncoded OOK under turbulence and 0.3 dB improvement over the SC decoder for the same R measured at BER of 10^{-6}.

For the case of $\sigma_I^2 = 0.31$, as shown in Fig. 2.2(c), the SC decoder with $R = 0.2$ has a coding gain of 13 dB with respect to the uncoded OOK under turbulence. The coding gain of 9 dB is observed for R of 0.3 with a degradation of 4 dB compared with $R = 0.2$. Note, the SCL decoder offers lower performance compared with the SC decoder for the same R with a coding gain of 10 dB, i.e., 2.5 dB lower than the SC decoder.
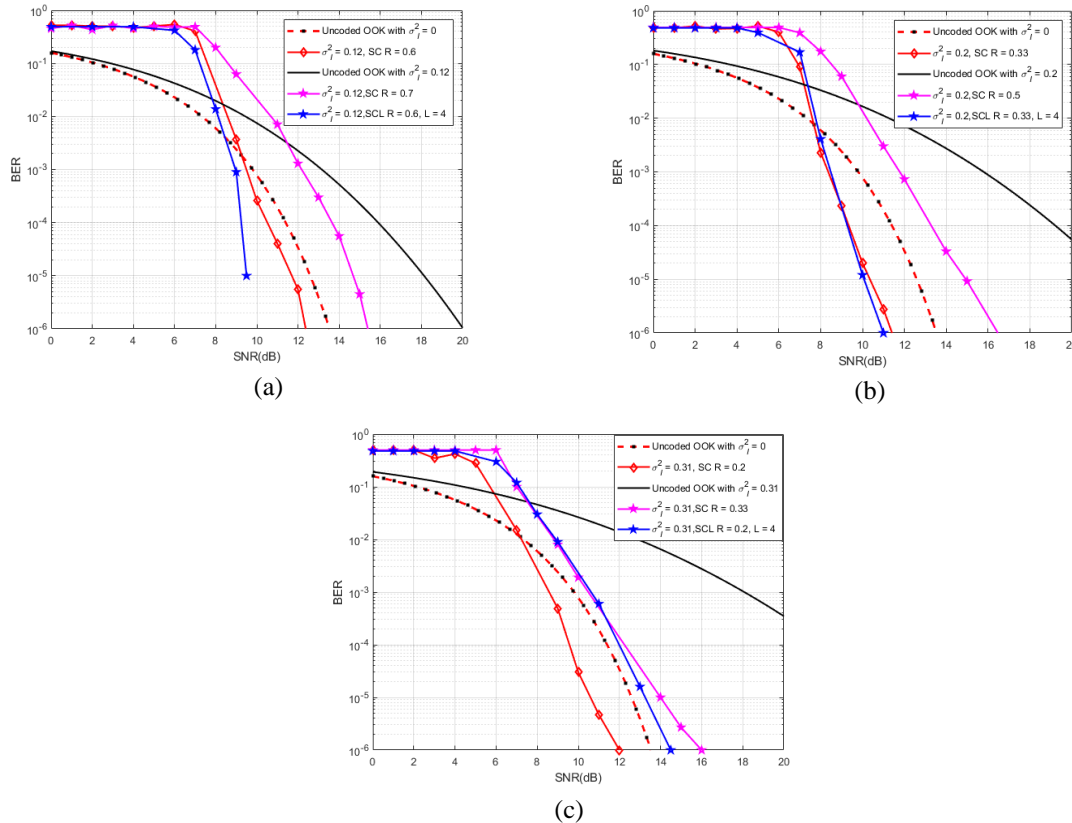

(a)

(b)

(c)

Fig. 2.2. BER performance as a function of the SNR for the link with SCL and SC decoders for σ_I^2: (a) 0.12, (b) 0.2, and (c) 0.31.

2.2. A Real-Time FSO System

One of the key challenges in FSO systems is that of changing weather conditions causing link outages and impairments, resulting in many reports in this area. Fog can cause reduced visibility [12] acting as a neutral density filter. Turbulence impacts the refractive index along the signal path, resulting in beam wandering at the Rx due to optical power deflection from the direction of propagation [13]. To address this challenge, significant research effort has been put into comparing modulation formats and digital signal processing (DSP) techniques to see how they compare. For instance, there have been reports of quadrature amplitude modulation (QAM) [14], orthogonal frequency division multiplexing (OFDM)[15], differential phase shift keying [6] and sub-carrier intensity modulation [16]. More recently, the performance of carrier-less amplitude and phase modulation (CAP) modulation has been evaluated in an FSO link [17]. Each of them offers bespoke advantages and disadvantages, indicating that a system capable of switching between different modulation formats would be an advantage.

Unfortunately, most real-time links demonstrated have utilised small form-factor pluggable (SFP) devices operating at gigabit speeds but restricting links to NRZ or PAM4 modulation

inflexibly [18]. This is a substantial disadvantage because it means that adaptation to specific weather conditions is impossible. In recent years, CAP (and its multi-band counterpart, m-CAP) have also been the focus of a huge amount of research interest within the optical wireless community, with a high number of demonstrations performed on visible light communications links [19]. CAP utilises a basis function (normally a square-root raised cosine (SRRC)) and a Hilbert pair to transmit information over the channel. Lately, there have recently been reports of systems where different pulse shapes have been tested as the basis function for the Hilbert pair.

One of the most interesting is the Xia pulse, which is valid for both Nyquist and root-Nyquist operations simultaneously. Most of the power in its side-lobes is retained in the pre-cursor, and the post-cursor side-lobe decays much faster than the SRRC. This is an interesting aspect as it will impact on system performance; recent literature has shown that using the Xia pulse as the basis function can yield performance gains over the SRRC in offline systems [20]. Therefore, we compare the SRRC with the Xia pulse in a real-time FSO system. Our real-time system is not based on an SFP module. We utilise an FPGA and a high-performance digital-to-analogue and analogue-to-digital pair, allowing us to test analogue modulation in real-time. The proposed m-CAP FSO platform is evaluated using an indoor controlled atmospheric chamber that emulates the foggy conditions that would occur outdoors. We have investigated a simulated fog environment by utilising neutral density filters (NDFs). Using NDFs to simulate fog is a valid approach that has been reported previously in the literature [21-26]. This approach allows us a more consistent approach than previous reports that have used fog machines – we can ensure our power received is consistent without relying on a network of external atmosphere monitors that require repeated calibration and custom controls. The reason we do refer to received power in our results and not to visibility, despite them being intrinsically interlinked, is because there are several fog regimes that could be selected for a given received power, and hence, the particle size considered would be different in each case.

The schematic block diagram for the proposed experimental testbed is illustrated in Fig. 2.3. The FPGA platform used is a low-cost Xilinx Zynq ZCU102 system-on-chip (SoC), which features both an FPGA and a quad core ARM Cortex A53 processor. We note, however, that the system should be portable to other Xilinx UltraScale+ architectures with minor adjustment provided the replacement board has similar transceivers. In this system, we have built the data generator via Analog Devices industrial input-output library (LibIIO) and the respective Python bindings (PyADI-IIO). By using this package, we can generate and process pseudo-random data streams in a flexible way via the embedded Linux platform, ensuring compatibility with any variety of m-CAP without having to perform the time-consuming reprogramming of the FPGA. The SoC has two parts, the programmable logic (traditional FPGA) and the processing side. Data is passed between the two through direct memory access; the data stream is saved into shared memory on the logic in the FPGA.
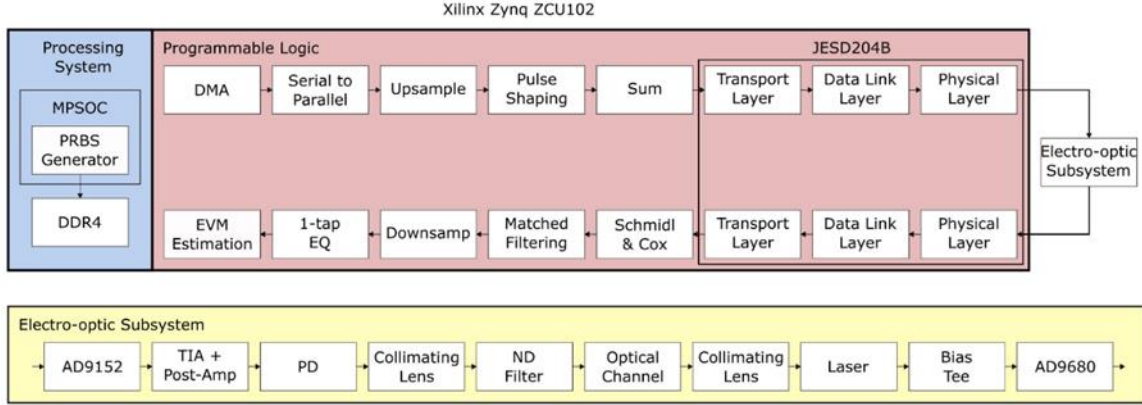
Fig. 2.3. The simplified block diagram of: (a) the system under test and the *m*-CAP modulation format. Abbreviations used: DDR4: double data rate 4, PRBS: pseudorandom binary sequence, DMA: direct memory access, AD: Analog Devices, PD: photodiode, TIA: transimpedance amplifier, ND: neutral density, EVM: error vector magnitude, EQ: equalization**.**

We are interested in analysing the performance of the FSO link using *m*-CAP modulation with different pulse shapes and in different atmospheric scenarios. The maximum bandwidth available in the link was ~300 MHz and we vary our data rate via the modulation cardinality. We select *k* = 2, 4 and 6 bits/symbol. Alternatively, we could have selected an oversampling rate of 2, causing the useful bandwidth to double. During our initial tests, however, we found that the analogue bandwidth of the electro-optic components in the proposed system was better suited to an oversample rate of 4, thus limiting us to 300 MHz. After the data is loaded, it is mapped onto the appropriate QAM constellation. The symbols are then up-sampled and pulse shaped using one of the two candidate filters under test, as will be described below. The first candidate basis function for the pulse shaping filter is the SRRC pulse, given by [20]:

$$g_s(t) = \frac{2\beta\left[\cos\left(\frac{(1+\beta)\pi t}{T_s}\right)+\sin\left(\frac{(1-\beta)\pi t}{T_s}\right)\left[\frac{4\beta t}{T_s}\right]^{-1}\right]}{\pi\sqrt{T_s}\left[1-\left(\frac{4\beta t}{T_s}\right)^2\right]},$$
(2.1)

where T_s is the symbol period, *t* is the instantaneous time sample and β is the filter roll-off factor. Similarly, the first-order Xia pulse is defined by [20]:

$$g_x(t) = \frac{\sin\left(\frac{\pi t}{T_s}\right)\cos\left(\frac{\pi t\beta}{T_s}\right)}{\left(\frac{\pi t}{T_s}\right)(2\beta t+T_s)}.$$
(2.2)

The pulse shapes of (1) and (2) with β = 0.35 and 300 MHz bandwidth are illustrated in Fig. 2.4. The Xia pulse is an asymmetric pulse with its peak slightly before the sampling instance. The majority of the power in its side-lobes is retained in the pre-cursor, and the post-cursor side-lobe decays much faster than the SRRC, offering advantages that have been demonstrated in visible light communications systems [20] but never in FSO. The excess energy factor β spreads the energy over the range of pulse shapes. Increasing values of β result in decreased sub-band transmission speeds following:
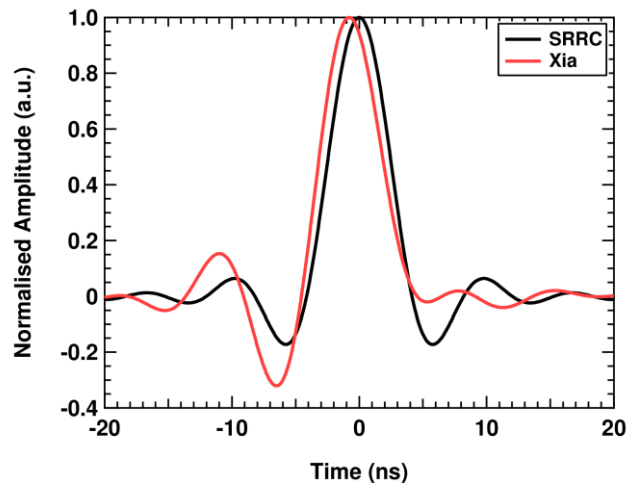
$$R_s = \frac{BW}{m(1+\beta)}.$$
(2.3)

Fig. 2.4. The two pulse shapes under test with a roll-off factor of 0.35.

Clearly, setting the value of β excessively will puncture the data rate, while setting it insufficiently will not provide a satisfactory guard band for the sub-bands. Therefore, we set this parameter to 0.1, 0.35, and 0.5 in order to test its impact on real-time links. We set the value of m from the set {1, 5, 10, 20}, following up studies performed in visible light communications that showed improved error performance with an increasing number of sub-bands [14]. We the effect on varying m on the system bandwidth in Fig. 2.5. Clearly, splitting the bandwidth into increasingly smaller sub-bands approaches an OFDM-like solution where each sub-band has lower performance requirements. This combination of values results in baud rates ranging from 205-280 MBd for our link. Thus, when we select $k = 2$ (4-QAM), the system is effectively operating at ~0.5 Gb/s. Likewise, for $k = 4$ (16-QAM), the transmission rate is ~1 Gb/s, and for $k = 6$ (64-QAM), it is approximately 1.5 Gb/s.
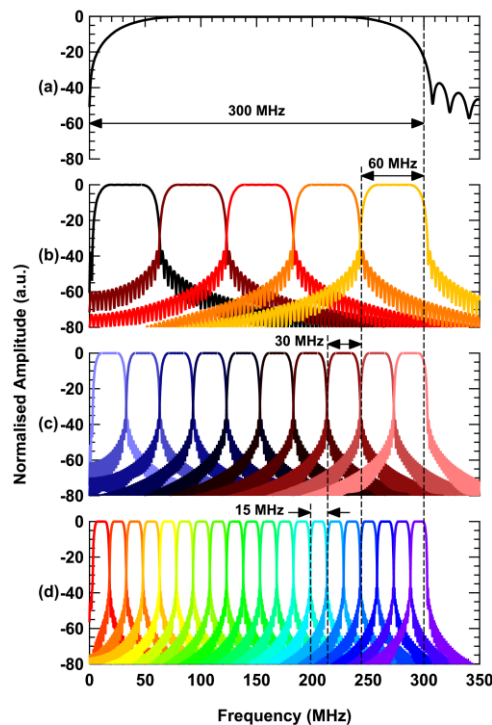

Fig. 2.5. Illustration of the concept of multi-band CAP: (a) 1-CAP, (b) 4-CAP, (c) 10-CAP and (d) 20-CAP. The same bandwidth is divided into an increasing number of sub-bands in each case. As the number of sub-bands increase, the baud rate is reduced but the overall transmission speed remains the same.

Next, the candidate pulse shapes are shaped to form a Hilbert pair, meaning they occupy the same frequency range but are separated in phase by 90∘. The final pulse-shaping filters of the in-phase and quadrature parts are given by $p_l^I(n)$ and $p_l^Q(n)$, respectively, which are given by:

$$p_l^I(n) = g(n)\cos(2\pi f_l n),$$
$$p_l^Q(n) = g(n)\sin(2\pi f_l n),$$
$$(2.4)$$

where $g(n)$ is one of the two candidate pulse shapes, i.e. the square-root raised cosine (SRRC) or Xia pulse, and f_l is the carrier frequency of the lth sub-band, given by [20]:

$$f_l = \frac{2l-1}{2m}BW. \qquad (2.5)$$

Finally, the transmitted signal $x(n)$ is given by:

$$x(n) = \sqrt{2}\sum_{l=1}^{m} X_l^I(n) * p_l^I(n) - X_l^Q(n) * p_l^Q(n), \qquad (2.6)$$

where $X_l^I(n)$ and $X_l^Q(n)$ correspond respectively to the in-phase and quadrature components of the data symbol to be carried on the lth sub-band. Following modulation, the data is framed and prepared for the DAC according to the JESD-204B standard. We have used a 16-bit DAC (i.e., AD9152) with a maximum sample rate of 2.25 GS/s that is connected to the ZCU102 via the mezzanine connector. Note, we select our sampling frequency f_s as 1.25 GS/s to match the analogue-to-digital (ADC) converter maximum sampling frequency. Next, the converted data stream is amplified prior to intensity modulation of an 850 nm laser diode (Laser Components PV85G0.53FCA-0-0-01) at 1 mW via a bias-tee (Mini Circuits ZFBT-6GW+). The intensity modulated light signal is then collimated using a ThorLabs F240FC-850 lens prior to transmission over the free-space channel.

We utilise a fibre optic cable to guide the light from the laser to the entrance of the free-space atmospheric chamber. The light emitted is collimated and transmitted across the chamber. At the Rx, we capture the light via a lens into a separate fibre. This approach allows rapid and simple alignment of the free-space system which can also be a timely operation, and also enables maximum coupling efficiency. On the other hand, depending on the divergence angle of Tx beam, there is limit on longest link distance before the optical beam size at the Rx exceeds the frontend aperture, hence exposing the link to geometric loss. Reducing the divergence angle avoids this issue, however, this introduces a requirement for increasingly large optical components, increasing the price, size and maximum link distance. However, larger optics at the Tx will escalate the effect of pointing errors due to smaller beam size since the side effect of beam pointing error is more pronounced on more collimated beams. On the other hand, having a larger Rx aperture will improve the resilience of the link towards pointing errors as the jittering beam will remain within the Rx active area. Apart from geometric loss and pointing error, the alignment of the system is also highly affected by the size of the optics. A narrow beam (i.e., a small footprint at the Rx) will make the alignment process a tedious job. Therefore, the middle ground, where the optimum Tx divergence angle and the Rx aperture size are adopted, as has been discussed extensively in previous work [16].

We have utilised the world-leading indoor atmospheric chamber at Northumbria University to evaluate the FSO link performance under different conditions [10] (a representative photo in **Fig. 2.**6).

Fig. 2.6. Representative photograph of the atmospheric chamber under use in this test.

The chamber is configured to emulate a fog environment and we have used neutral density filters to control the received power P_r to maintain consistency throughout the test and measurement. Since the FSO channel has been extensively studied and reported in the literature extensively [18], we do not discuss it in detail here. However, it should be noted that we only investigate the impact of fog on the performance of the FSO link and have not considered others channel conditions such as turbulence. Fog results in a reduction of visibility V due to aerosol scattering, which can be modelled with a coefficient β_α as follows:

$$\beta_\alpha(\lambda) = \frac{3.91}{V}\left(\frac{\lambda}{550\,\text{nm}}\right)^{-q}, \tag{2.7}$$

where λ is the wavelength and q is the size distribution of the scattering particles given by Kim model in [27], which has been used as a valid approach to of modelling in FSO for many years. The Rx consists of a focusing lens (ThorLabs F240FC-850) followed by a photodiode (ThorLabs DET025AFC), a transimpedance amplifier (Texas Instruments OPA855DSGEVM), and a limiting amplifier (AD MAX3747), which feeds the ADC (AD9680, 14-bits with a maximum sample rate $f_{s\text{-max}}$ of 1.25 GS/s). The most critical aspect of real-time system performance is the clock recovery, which must be carried out properly in order to ensure that the data can be fully recovered. Here, we have employed the Schmidl & Cox method traditionally used with OFDM modulation, in which the first symbol in a frame is transmitted with known information. Considering that the free-space channel is static, flat in terms of its frequency response and its profile is only sensitive to the received power, we hypothesize that there should be little difference in system performance between a frame structure where one synchronisation frame is transmitted before continuous data, rather than re-syncing periodically as there is no new channel information to obtain, provided the link remains undisturbed. After the data is de-framed, synchronisation is performed before the data is demodulated. In general, m-CAP signals are demodulated using time-reversed matched filters, a one-tap equaliser and hard threshold detection. The time-reversed matched filters are given as $f(n) = g(-n)$.

We evaluate the performance of the proposed m-CAP FSO system by analysis of the error vector magnitude (EVM) in this section. In Fig. 2.7, we illustrate the EVM performance of the link operating at 0.5 Gb/s, using both pulse shapes for all m and $\beta = 0.35$. Based on previous studies in band-limited optical wireless links [25], we anticipated that a higher order of m would improve the system performance, particularly in low power environments due to the lower sub-band baud rates. However, the results show the opposite trend is true; the systems that used the higher value of m demonstrate worse EVM performance in low visibilities (i.e., $P_r < -13$ dBm) and the single sub-band system has greater sensitivity. This is also true for all values of β tested. This is attributed to a relatively large null observed in the frequency response of the Rx electronics. The null is observed at approximately 210 MHz and the bandwidth of the m-CAP signal is 300 MHz. We believe that this null is the result of destructive interference caused by an impedance mismatch in our Rx. Therefore, for systems not AWGN limited, transmitting a

1-CAP signal would entail utilising the entire spectrum, which could then be easily corrupted due to the large null in the frequency response. This explains why the signal recovers to lower EVM levels when *m* is increased in higher received power environments. Similar results were obtained for the *k* = 2 and 6 systems, which are not shown here in the interest of conserving space. Note, in our previous work, we demonstrated that by dividing the *m*-CAP signal into increasingly small sub-bands, the channel begins to appear flat to each individual sub-band, regardless of the overall shape and we believe this is why the spectral null impacts the higher order subcarriers less [26].
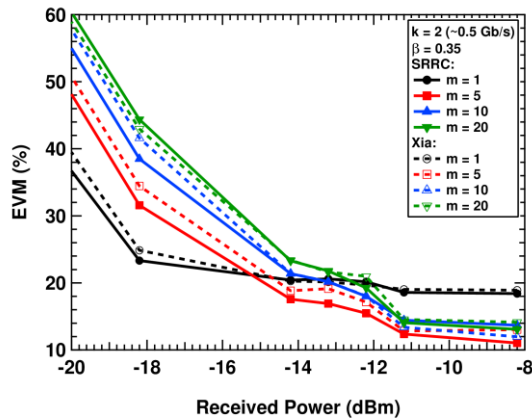
Fig. 2.7. EVM performance of the ~0.5 Gb/s illustrating the sub-band specific performance of the link for both filters under test.
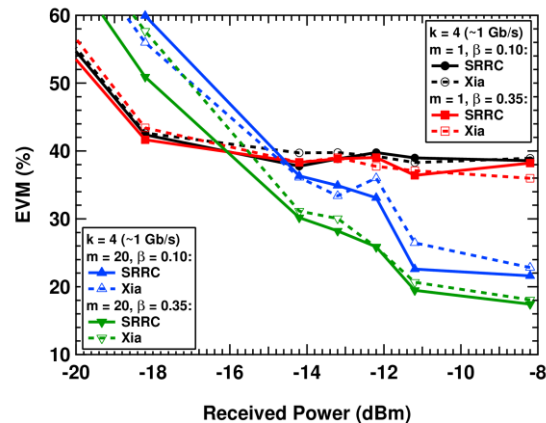
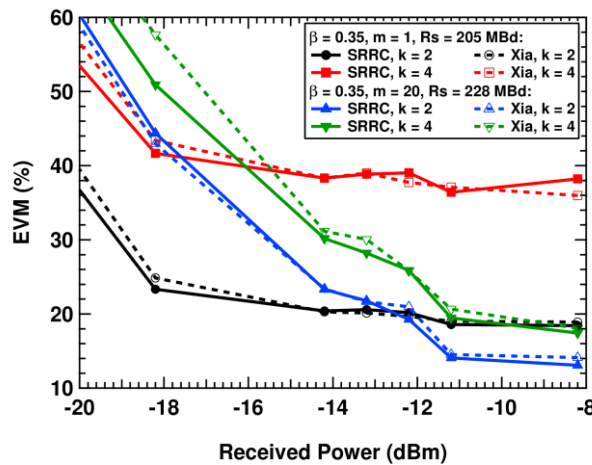**Fig. 2.8.** EVM performance of the ~1 Gb/s link for varying numbers of sub-bands and roll-off factors.

Fig. 2.9. EVM performance of the ~0.5 and ~1 Gb/s FSO links with a roll-off factor of 0.35. The performance gain for the ~1 Gb/s system at high received power outperforms that of the ~0.5 Gb/s equivalent.

We also observed that the SRRC consistently outperformed the Xia pulse, counter to previous reports [20]. While the performances are similar, the Xia pulse consistently has a small sensitivity penalty. Since our electro-optic system is not band-limited and we are comfortably within the linear region of operation, we attribute this to the fact that the Xia pulse has a centre-offset peak. This offset is the source of the penalty since the optimal sampling point has a lower SNR than the SRRC due to the nature of the offset. Previous reports tested the Xia pulse in a highly bandlimited system that introduced significant non-linearity, hence the different outcome. Furthermore, there have been no real-time reports on the performance of the Xia pulse so far. Previous efforts have performed data capture via a real-time oscilloscope, meaning that the optimal sampling point can always be found, benefitting performance in a way that cannot be matched in this work. In Fig. 2., we illustrate the comparative performance of the two pulse

shaping filter candidates using m of 1 and 20 operating at ~1 Gb/s. The same observation as above occurs where the system with the higher number of sub-bands performs better at higher received power values and the single-band system operates better in lower received powers. We include two values of β to illustrate that the effect is independent from it. We also note that for $k = 6$, a similar trend is observed. We also note that there is little difference in performance between the Xia and SRRC in the most part.

Next, in Fig. 2.9 we compare the performance of the ~0.5 and ~1 Gb/s systems for a fixed value of $\beta = 0.35$. Clearly, both systems follow similar trends judging by their EVM profile trends. In both cases, when the system is noise limited the performance of the 1-CAP system is superior and vice-versa in high performance environment. Interestingly, the increase in performance for the ~1 Gb/s system in higher received powers (i.e., -8 dBm) is substantially larger than it is for the ~0.5 Gb/s system. For the former, the EVM improves from ~40 to ~18%, while for the latter, the improvement is from ~18 to ~14%. We attribute this to a combination of the performance gain introduced with higher sub-bands mentioned previously in the discussion of Fig. 2.7 and the fact that increasing the received power alleviates the far greater SNR penalty imposed on the system for 16-QAM in comparison to 4-QAM. Similar trends are also observed when $k = 6$ which are not shown here. The performance of this system (~1.5 Gb/s) is an approximate EVM value of ~20% for $m = 10$ and 20 at a received power of - 8.2 dBm.

2.3. Transceivers for MIMO FSO

Our work adopted GNU Radio which is an open source software development ecosystem that provides digital signal processing blocks to implement the OWC and RF systems to demonstrate the MIMO FSO link availability under varying atmospheric conditions. We outlined the design and implementation of out of tree (OOT) modules/signal processing blocks integrated into GNU Radio. Then we analyze the performance of a MIMO intensity modulation-direct detection FSO system with the adaptive switching using GNU Radio under various atmospheric conditions for real-time data transmission. The proposed system with OOT modules facilitates the implementation of N number of Txs and Rxs. In this work, 4x2 MIMO FSO system is considered as a proof of concept, see Fig. 2.10. The design employs two sets of Txs and Rxs for parallel transmission of two different signals to improve link reliability.

A dedicated switching algorithm is proposed to turn on the Tx(s) based on the channel conditions. Each Tx and Rx can operate independently or in a unified cluster. Fog and turbulenceinduced attenuation and geometric losses are taken into account when determining the link's reliability. Under normal weather conditions, Tx-A1 and Tx-B transmit two independent data streams. In fog or turbulence, however, additional Txs (Tx-A2 and Tx-B2) can be used if the following conditions, i.e., $L_{\text{Atm (input)}} \geq L_{\text{Atm (Thres)}}$ or $\sigma^2_{I(\text{input})} \geq \sigma^2_{I(\text{Thres})}$ are met. This is to ensure that the link's availability is maintained to the maximum extent possible at the expense of increased transmit power P_{Tx}. On the Rx side, the received optical beams are focused by optical collimators onto two optical Rxs (Rx-A and Rx-B), which are composed of PD and trans-impedance amplifiers. The electrical signal that has been regenerated is then applied to moving average filters, samplers, and threshold detectors (slicers) to recover the estimated sequence of the transmitted data stream. The BERT is then employed to determine the real-time BER by comparing the received and transmitted data streams. Note that (i) the used parameters and link characteristics in terms of the channel loss (V, σ^2_I, and C^2_n) are monitored using SDR/GNU Radio, and (ii) the extracted link characteristics and the received

OOK signal are generated in the GNU Radio software domain. In this research, it is assumed that the signals transmitted and received are uncorrelated. Based on the numerical evaluation of L_{Atm} for a given V and L, the link status is studied and a set of Txs to be used is carried out. Note, σ_I^2 and C_n^2 are predicted to reach a forward error correction (FEC) BER of 3.8×10^{-3}, the upper limit.
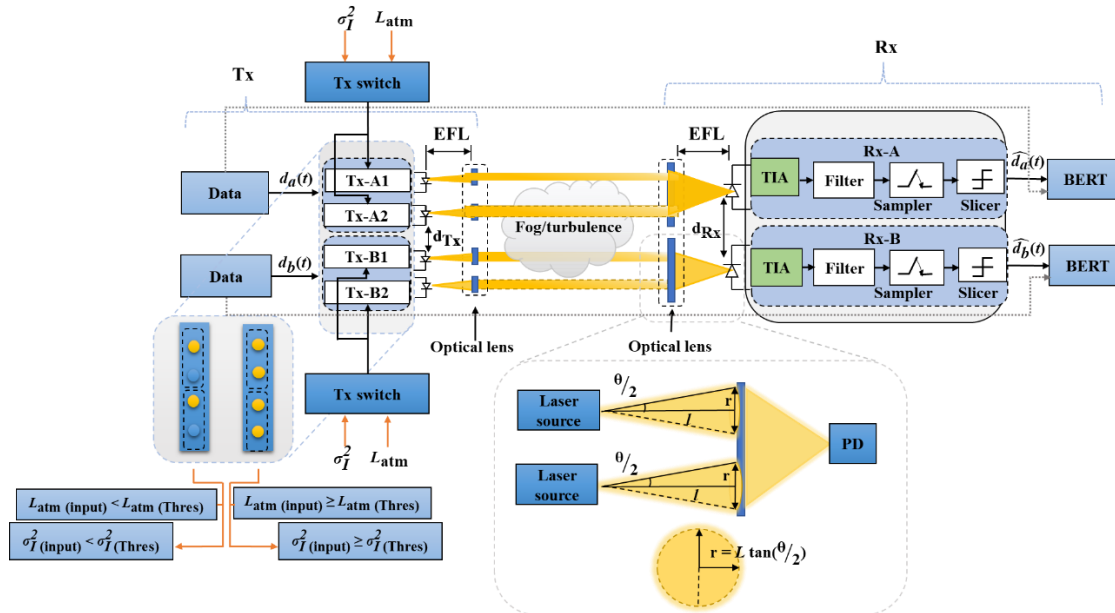

Fig. 2.10. Schematic system block diagram of MIMO FSO system with adaptive switching algorithm in software defined GNURadio ecosystem.

To investigate the performance of the software defined adaptive switching MIMO FSO system, the SDR-based Tx, Rx, and channel have been implemented in GNURadio, along with a general-purpose processor-based real-time signal processing framework. The GNURadio is also capable of functioning as a simulation environment without the need for actual hardware. Note that GNURadio applications are typically written in Python as a package and combined with DSP blocks integrated within GNU Radio and implemented in C++ to perform crucial signal processing tasks. Fig. 2.11 depicts the implementation of the MIMO FSO system in the GNU Radio domain, which consists of a Tx, a channel, and an Rx. At the Tx, a sequence of pseudo-random binary data in the OOK format is applied to the throttle module, which is used to prevent CPU congestion following real-time simulation. Throttles outputs are applied to (*i*) virtual sink modules and (*ii*) MIMO-Tx modules which output is applied to virtual sink modules. In addition, the MIMO- Tx is provided with the outputs of the virtual sources, which represent feedback data on atmospheric loss $L_{\text{Atm (input)}}$ in dB and $\sigma_{I(\text{input})}^2$ of the channel. Since GNU Radio provides a graphical user interface (GUI) to generate and configure signal processing flow graphs, sample time waveforms were generated at the outputs of the MIMO-Tx (links A and B) and the optical Rx as shown in Fig 2.12(a-f). Figure 2.12(a-c) depict the received signal under a clear channel, where only a single Tx (TxA1 and TxB1) is active at any time given. Additional Txs are activated to ensure link availability based on the channel condition, provided $L_{\text{Atm}} \geq L_{\text{Atm (Thres)}}$ of 0.3 and $\sigma_I^2 \geq \sigma_{I(\text{Thres})}^2$ of 0.02, thus meeting the FEC BER limits of 3.8×10^{-3}. Fig. 3.12 (d-e) depict the simulated time waveforms in this instance.
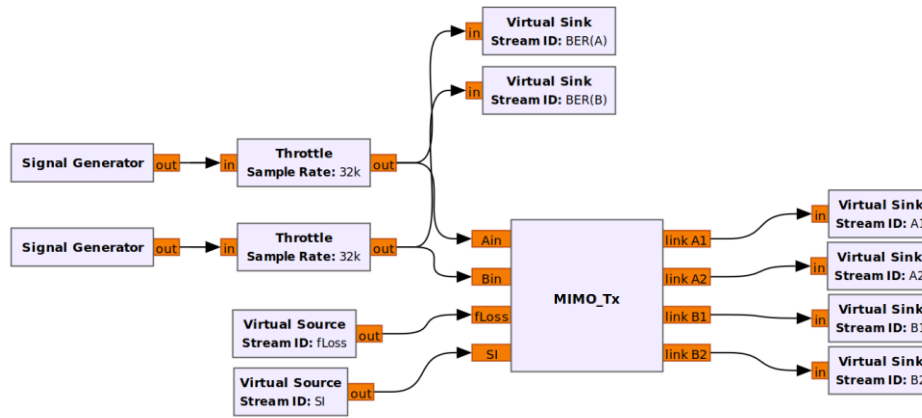
(a)
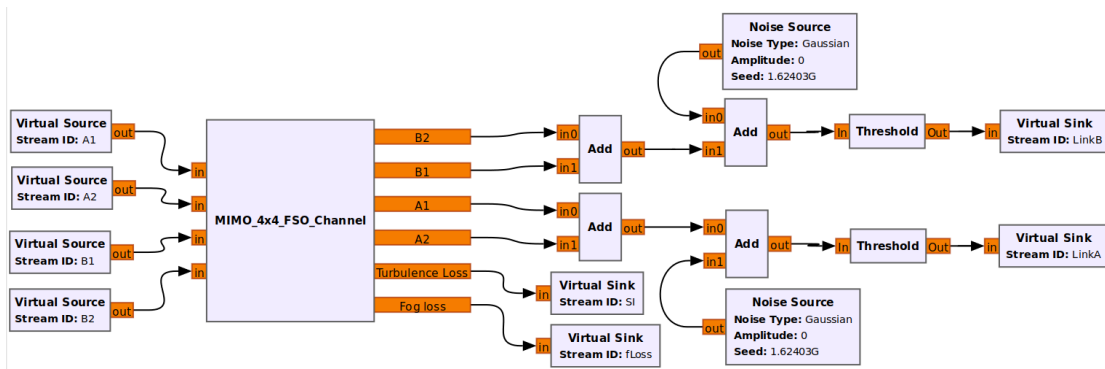
(b)
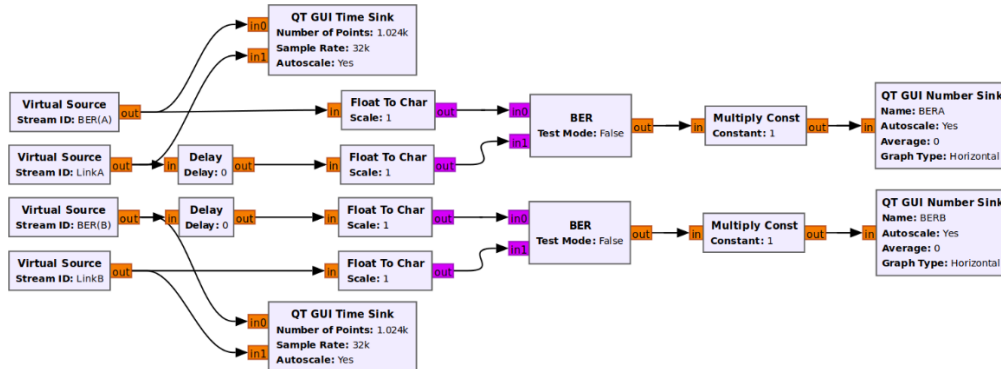
(c)

Fig. 2.11. System implementation for (a) Tx with fog and turbulence, (b) channel with the additive white gaussian noise, and (c) the Rx with real-time BER estimation in GNURadio.
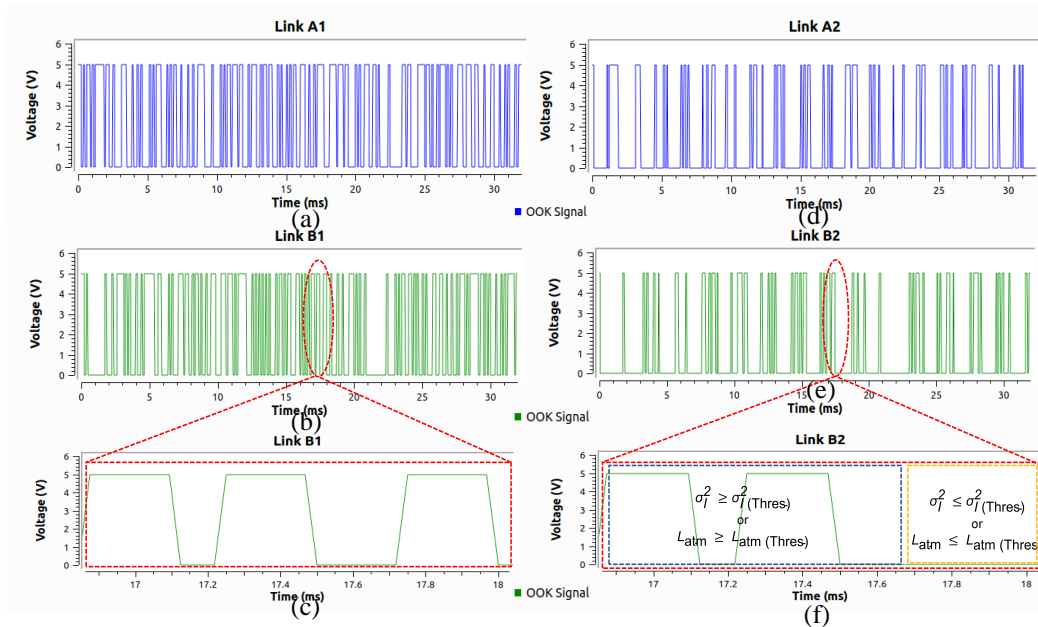
Fig. 2.12. OOK waveforms at the: (a) Tx-Link A, (b) Tx-Link B, (c) optical Rx for a clear channel, and (d) Tx-Link A, (e) Tx-Link B, and (f) optical Rx for an un-clear channel.
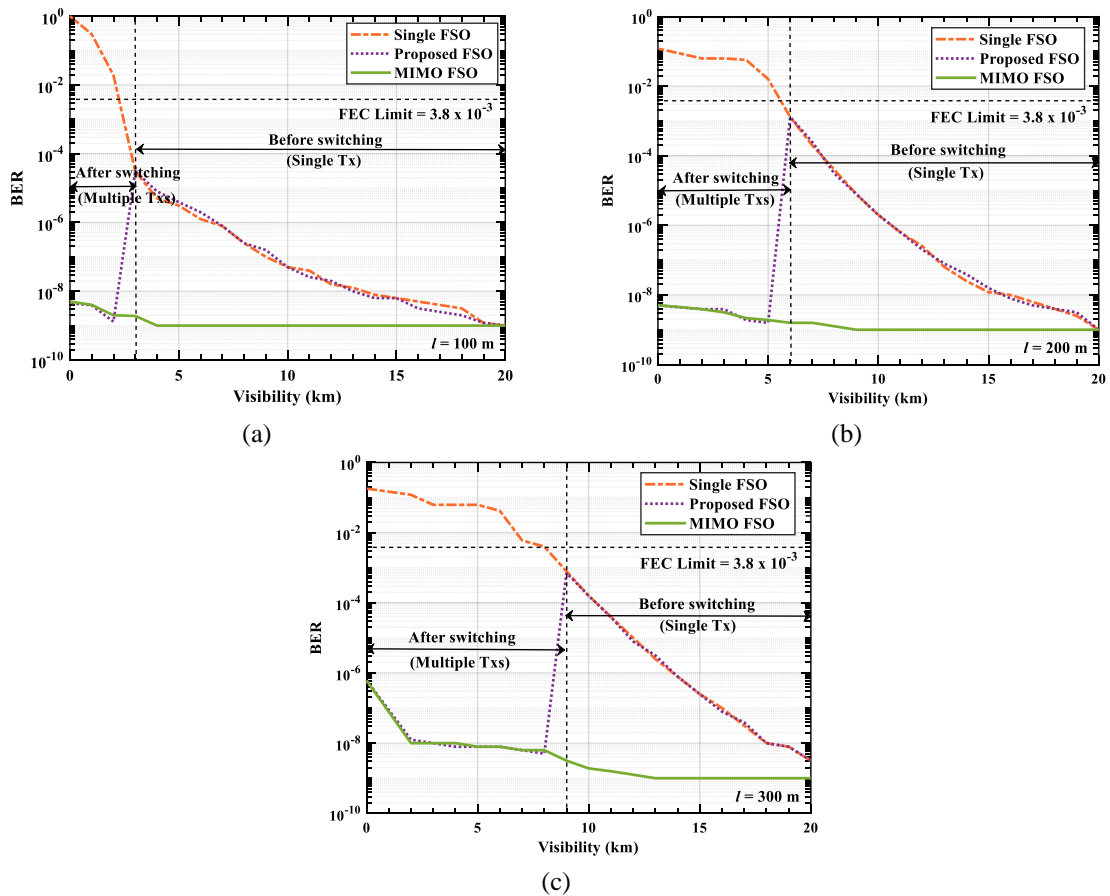

Fig. 2.13. BER vs. the visibility for single, MIMO and proposed FSO with adaptive switching links for: (a) 100, (b) 200, and (c) 300 m with fog.

The designed and built OOT not only satisfies the objective to monitor the system performance in real-time, also satisfies the purpose of reconfiguring without the need to change the hardware platform. Moreover, it also offers an easy experimental implementation on the fly due to direct communication with the SDR platform. For a clear channel with V of 20 km, the required P_{Tx} is considered to be 10 dBm with 0 dB channel loss and the additional losses including L_{Geo} are assumed to be low. The system performance in terms of BER for the link range of 100, 200, and 300 m links under the fog conditions are depicted in Fig. 2.13. For a 100 m link, MIMO outperforms the single FSO link for $V<18$ km and especially at lower values of V as expected. For the FSO link with the proposed adaptive switching algorithm, the BER pattern follows the single FSO link, up to a distance of 3 km, after which the BER drops to the MIMO FSO link level with a BER of 10^{-9} which is due to turning on the additional Txs as explained before. The same pattern is observed for 200 and 300 m links as depicted in Fig. 2.13 (b) and (c) except when the switching takes place at V of 6 and 9 km where the BER values are at 1.3×10^{-3} and 7.4×10^{-4}, respectively. Also observed are (*i*) the BER plot for the MIMO FSO link, which is almost constant (i.e., 10^{-9}) at $V > 5$ and 10 km in Figs. 2.13(b) and (c). Additionally, compared to D_{Rx}, the beam spot sizes of 17.5 and 34.9 mm in 100 and 200 m, respectively, are smaller. Therefore, L_{Geo} is neglected. Due to the beam spot size of 52.4 mm, an extra 1.2 dB of L_{Geo} is introduced in the 300 m link.

For all three systems, the estimated BER exceeds the FEC limit for $\sigma_I^2 < 0.02$, hence, $\sigma_{I(Thres)}^2$ was set at ≤ 0.02. The systems were then simulated under weak to moderate turbulence (i.e., $10^{-11} < C_n^2 < 10^{-17}$) to determine the BER performance for all three systems and link spans of 100, 200, and 300 m as depicted in Fig. 2.14. In these plots, the same pattern is observed as in Figure 2.13 where the BER of the 100 m link adaptive switching the FSO link followed the single FSO link plot for C_n^2 of $10^{-13} \text{m}^{-2/3}$, beyond which the BER significantly improves, reaching the level of MIMO FSO link at C_n^2 of 10^{-12} from 10^{-4} to 2.5×10^{-8}, see Fig. 2.14 (a). This improvement in BER performance is due to the addition of Tx-A2 and Tx-B2. In Fig. 2.14(b), the BER plot for the proposed link changes direction at $C_n^2 < 10^{-14}$ decreasing to 10^{-8} at $C_n^2 < 10^{-13}$ and then increasing with C_n^2. In Fig. 2.12 (c), the BER transitions from 10^{-3} to 2×10^{-9} at C_n^2 of 10^{-14} to 10^{-13} for the proposed system. Note that, (*i*) the BER floor level for both MIMO FSO and proposed FSO links is $\sim 10^{-9}$ for $C_n^2 > 10^{-13}$; and (*ii*) the 200 and 300 m long MIMO FSO link performance degrades more under turbulence effects (i.e., $C_n^2 > 10^{-13}$).
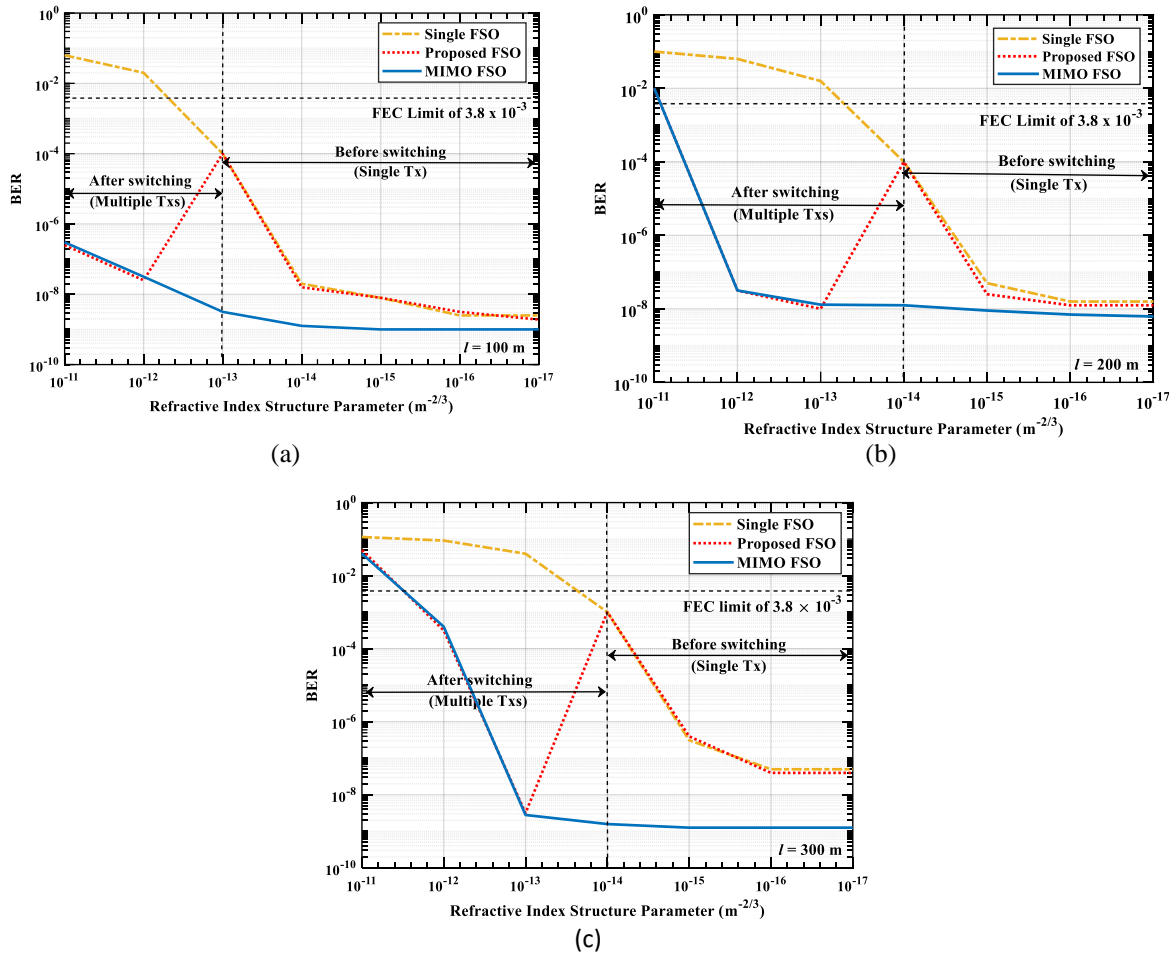
Fig. 2.14. BER vs. C_n^2 for single, MIMO and proposed FSO with adaptive switching links for: (a) 100, (b) 200, and (c) 300 m with turbulence.

2.3. Conclusions FSO

Several prototypes of FSO systems have been developed and experimentally tested within the NEWFOCUS project. We especially focused on MIMO links and adaptive switching mechanisms. A fully functional FSO link with a feedback path has been implemented using cost effective off-the-shelf components, i.e., media converters and small form-factor pluggable modules. We propose a switching mechanism at the transmitter to improve the link performance under different fog conditions and provide results for the proposed MIMO FSO system compared with a single FSO link. The real-time channel estimation is demonstrated and based on the channel state information, adaptive switching is carried out in GNU Radio. We show that the proposed system under the heavy fog condition offers almost the same packet error rate under the clear channel but with a reduced data rate by about 100 Mbps

3. Vehicular Communications

To extend the communications range in wireless systems, the use of relay nodes (RNs) has been proposed in [28,29]. In [28], relay-based systems were shown to be viable in mitigating channel fading over short transmission ranges, with an enhanced power margin by up to 18.5 dB using a single RN at a target outage probability of 10^{-6}. In [5], the viability of VLC using multiple taillights (TLs) Txs and photodiodes (PDs)-based Rxs with orthogonal frequency division multiplexing for direct transmission (DT) and multi-hop transmission (MHT) was reported. It was shown that, with spatial multiplexing MHT offered reduced average signal power of -59 dBm for a single hop (for link span L_s of 16 m) compared with -27 dBm for DT (for L_s of 12 m). Multi-user VLC serving as a RN for other users was introduced in [30]. A similar method with vehicles acting as RNs was proposed in [31] for inter-vehicle communication systems.

Recently, an experimental investigation of a relay-assisted vehicular VLC (VVLC) link was reported in [32] showing that, the decode and forward (DF) relay scheme is the preferred option. Consequently, we extend the work in [32] by further investigating relay-assisted VVLC for a range of transmit power P_t and longer L_s using a Monte Carlo system-level-based simulation model, which allows considering different communication geometries and parameters. Also, we investigate the orientation of the RN in terms of the azimuth (horizontal)/elevation (vertical) angles of the source vehicle. Note, in VVLC using a combination of an imaging lens and PDs to increase the received optical power density, the link will experience beam spot offset (BSO) (i.e., an offset in the projected beam spot from the centre of the focal plane away from the PD) when there is a misalignment between the Tx and Rx. This is due to non-stationary vehicles positions and varying positions of TLs (Txs) and Rxs depending on the vehicle models. The contributions of the work carried out are (*i*) investigation and providing insights on the effect of misalignment between vehicle's Txs and Rxs in real road conditions on the BER performance of the system resulting from the BSO on the focal plane, which is carried out for the first time to the authors best knowledge; (*ii*) investigating relay-assisted VVLC links with amplify and forward (AF) and DF relay schemes; (*iii*) mitigation of the misalignment issue considering typical vehicular geometry parameters; and (*iv*) providing insights to the impact of various parameters such as PD size, incidence angle and L_s, on the performance of VVLC.

The schematic system block diagrams of the proposed amplify-and-forward (AF) and DF relay-assisted VVLC systems are shown in Figs. 3.1(a) and (b), respectively. It is simulated using Monte Carlo model and considers different communication geometries and system parameters for evaluating the link performance in terms of the BER. At the Tx, a 3×10^5 random bit stream in the non-return-to-zero on-off keying (NRZ-OOK) data format is generated, which is upsampled (number of samples/bit $n_{sam} = 10$) prior to intensity modulation of the Tx. The modulated signal is transmitted over the 1st free space channel to the RN. Noise i.e., emulated sunlight induced noise obtained from empirical measurements, which is the dominant source in VVLC systems during daytime, and all other noise sources outlined in Section II are added to the received signal. At the RNs and Rxs, OFs (a wavelength band of 405-690 nm) and OCs with the f of 15 mm (transmittance of 0.92 for both OF and OC) are used to improve the signal to noise ratio. The L_{s1} has RNs at 25 and 50 m, L_{s2} has RNs at 25 and 65 m. For the AF relay link, at RNs the regenerated electrical signal is amplified to its original power level prior to transmission to the next RN and finally to the end user (Fig. 3.1(a)). For the DF relay link, the regenerated electrical signal is applied to the matched filter (MF) and decoder prior to packet generation. Note, the detection process is the same at the DF RN and end user, where MF is composed of integrator, sampler (with a sampling interval $t_s = n_{sam}$), and slicer (the threshold

level set to the mean value of sampled filtered signal). The decoder sets the signals from the output of the slicer that are below the threshold level to 0 and else to 1. The system parameters are T_K= 298 K, I_{amb}= 13.3 mA, B=5 MHz, I_{dk}= 5 nA, R_L= 50 Ω and R_b=10 Mb/s. I_{amb} is calculated from the solar irradiance measurement given in [33].
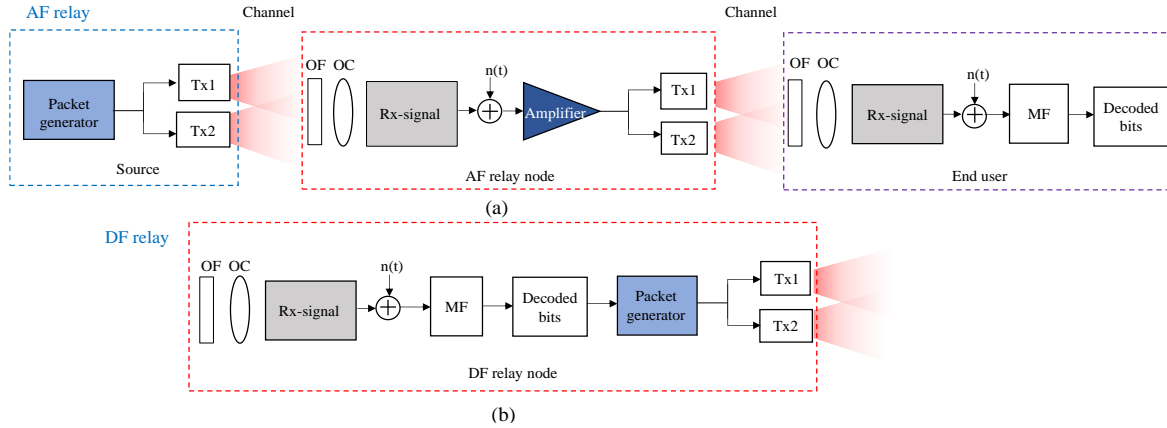

Fig. 3.1. System block diagram for the VVLC relay-assisted links with: (a) AF, and (b) DF relay schemes (just relay node (RN) shown).

The BER as a function of L_s for a range of P_t is presented in Fig. 3.2, where Txs and Rxs are in alignment and have diagonal widths d_{Tx} and d_{PD} of 5 cm and 1 mm, respectively (same PD type is used in all Rxs). As shown in Fig. 3.2, BER improves with a 0.25 W increase in P_t (i.e., 0.75 to 1 W and 1 to 1.25 W) by a drop of up to 68 and 89 %, for the AF and DF links, respectively at the end of the 2nd channel.
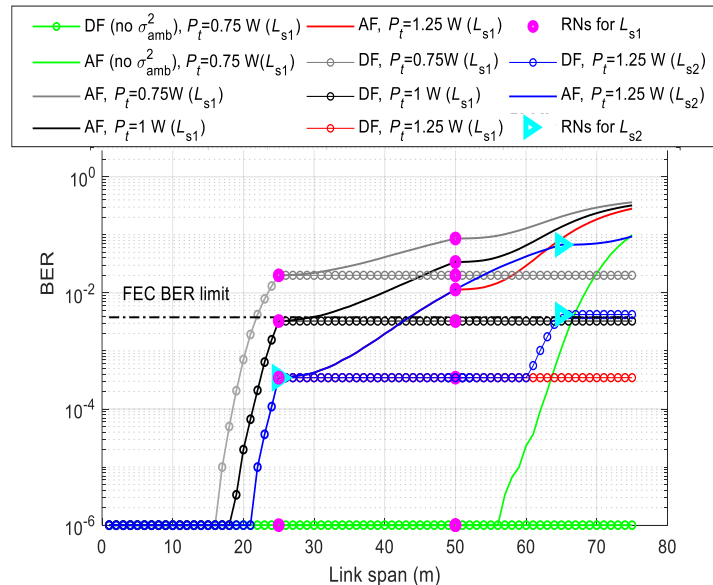

Fig. 3.2. BER performances as a function of L_s for a range of P_t.

Note, for error free transmission, the BER floor level is set to 10^{-6}. Notably, links with DF show a more stable BER compared with AF but starts to degrade after certain L_s depending on the inter hop distance. For comparison, at P_t of 0.75 W, links are shown with and without σ_{amb}^2 with only L_s of 21 and up to 66 m achieved, respectively at the FEC BER limit of 3.8×10^{-3}. Moreover, at the FEC BER limit at the end of the 2nd hop and for $P_t = 1$ W, L_s is 150 % higher for DF compared with AF under emulated sunlight noise. This is because, in an AF relay-based link the system performance is affected more by the noise accumulation over the transmission

span since the received signal at the RN is simply amplified with no regeneration or reshaping in contrast to the DF. Note, in VVLC systems (*i*) for practical implementation compact devices such as field programmable gate arrays can be used for encoding/decoding, modulation/demodulation driver for the Tx, Rx, etc., at various stages; and (*ii*) the exact alignment between the Tx and the Rx is not possible with and without RNs maintaining due to vehicles movement, which result in variations in φ, see Fig. 3.3.
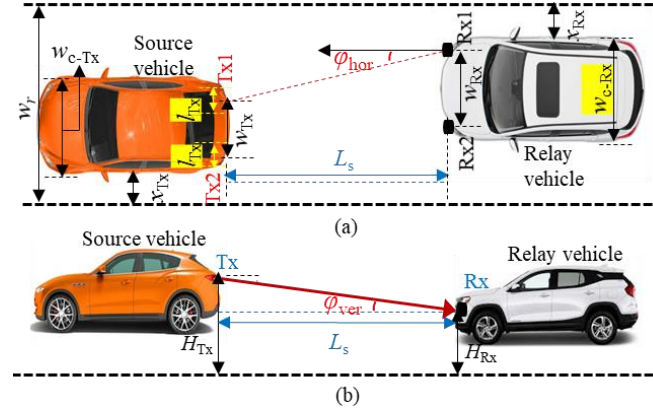

Fig. 3.3. VVLC configuration: (a) top view showing Tx-Rx horizontal incidence angle, and (b) side view showing Tx-Rx vertical incidence angle.

Hence, links using an imaging lens at the Rx will experience BSOs in the horizontal, vertical or both directions on the focal plane at the PD, see Fig. 3.4. The horizontal incidence angle for at least a Tx to be captured for a road lane width w_r is given by:

$$\varphi_{\text{hor}} = \arctan\left(\left(w_r - \left(\frac{w_{\text{c}-\text{Tx}} - w_{\text{Tx}}}{2}\right) - \left(\frac{w_{\text{c}-\text{Rx}} - w_{\text{Rx}}}{2}\right) - \left(w_{\text{Tx}} - \frac{l_{\text{Tx}}}{2}\right) - x_{\text{Rx}} - x_{\text{Tx}}\right) \Big/ L_s\right),$$
(3.1)

where $w_{\text{c}-\text{Tx}}$, $w_{\text{c}-\text{Rx}}$, w_{Tx}, w_{Rx}, x_{Tx}, x_{Rx} and l_{Tx} are the widths of the Tx and Rx vehicles, distance between the centres of Txs 1 and 2 and Rxs 1 and 2, distance of Tx and Rx vehicles from the edge of road lane and the length of the Tx, respectively. On the focal plane at the PD and using a converging rectilinear lens, the maximum BSOs is given as:

$$b_{\text{of}} = f\tan(\varphi),$$
(3.2)

$$b_{\text{of}} = \begin{cases} b_{\text{hor}-\text{of}} & \varphi = \varphi_{\text{hor}} \\ b_{\text{ver}-\text{of}} & \varphi = \varphi_{\text{ver}} = \arctan((\Delta H)/L_s), \end{cases}$$
(3.3)

where the offset between the Tx's and Rx's vertical heights is $\Delta H = |H_{\text{Tx}} - H_{\text{Rx}}|$, φ_{ver} is the vertical incidence angle, $b_{\text{hor}-\text{of}}$ and $b_{\text{ver}-\text{of}}$ are the horizontal and vertical BSOs on the focal plane. Using (3.1)-(3.3), $w_{\text{c}-\text{Tx}}$ and $w_{\text{c}-\text{Rx}} = 1.7$ m, w_{Tx} and $w_{\text{Rx}}=1.2$ m, and $L_s \geq 2$ m the maximum φ_{hor} (i.e., the worst case scenario for inter-vehicle communications at the opposite edge of the road lane) for $w_r= 2.5$ and 3.75 m (which are the minimum and maximum w_r for a lane) are 21.8 and 45.7°, respectively and the maximum φ_{ver} for $\Delta H = 0.5$ m for $L_s \geq 2$ m is 14°. Consequently, Fig. 3.5(a) depicts the plots of BSOs as than the diagonal width d_{PD} of a high-speed PD (e.g., 0.1 mm). Notably, AFOV of VLC depends on *f* of the lens and the size of the PD as described in [11] and depicted in Fig. 3.5(b).
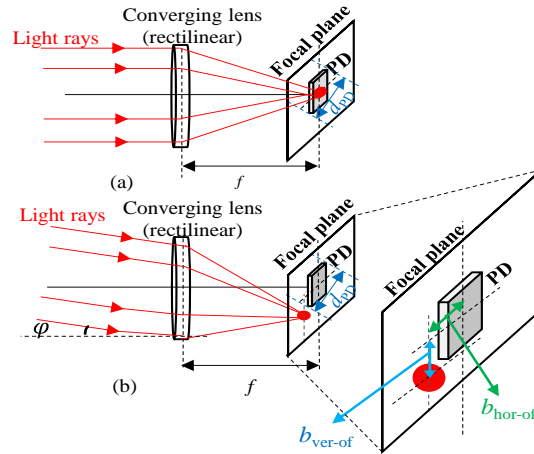
Fig. 3.4. (a) Parallel, and (b) non-parallel light beams through a converging lens.
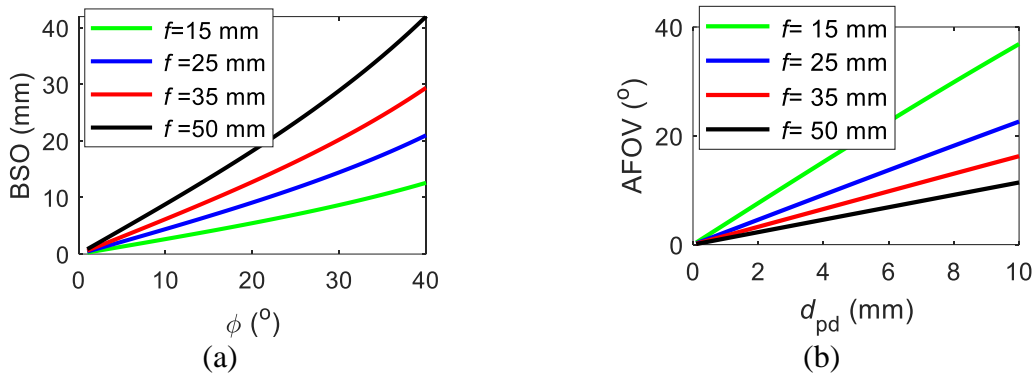

Fig. 3.5. (a) BSO vs. φ and (b) AFOV as a function of d_{PD} for a range of f.

Note, the width of the projected focused Tx's image (i.e., the beam spot size (BSZ)) in terms of the Tx's diagonal widths d_{Tx} is $d_{BSZ} = d_{Tx}f/L_s$ [28]. Thus, the size of Tx's beam spot is a critical factor in considering BSZ- and BSO-induced power losses at the PD, see Fig. 3.6. As shown BSZ plots exponentially drop with L_s for all values of d_{Tx} and increases with f, reaching below 2 mm at $L_s > 10$ m and converging to < 1 mm for L_s of 25 m. Note, at shorter L_s BSZ is in orders of magnitudes larger than at longer L_s. E.g., at f of 50 mm, $d_{Tx} = 15$ cm, and at L_s of 5 and 20 m the BSZs are 1.5 and 0.375 mm, respectively. Also, the link performance is not degraded due to BSO provided the PD size is greater than the BSO and BSZ to ensure capturing of the projected light beam spot. Note, larger size PDs can be used, since the data transmission rate is low in VVLC [34].
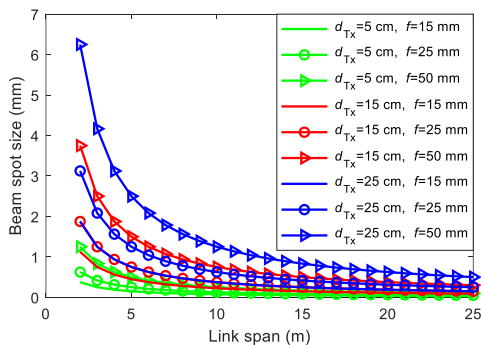

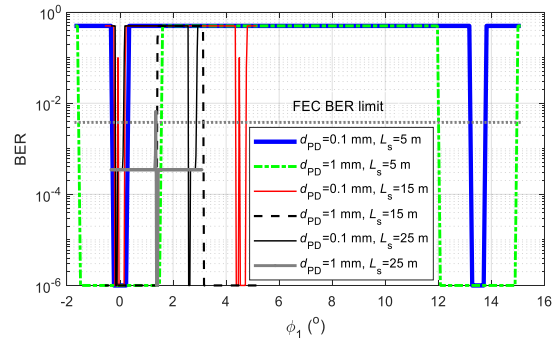**Fig. 3.6.** Beam spot size at the focal plane versus L_s for a range of f and d_{Tx}.

Fig. 3.7. BER degradation as a function of φ_1 for a range of d_{PD} and L_s.

Furthermore, for the first time to the authors' best knowledge, we investigate the effect of the orientation of the relay vehicle with respect to the source vehicle considering BSO due to the φ on the BER performance at the first RN. System parameters used are $P_t = 1.25$ W, $f = 15$ mm and $d_{\text{Tx}} = 5$ cm. Note that, for same horizontal/vertical misalignment offset distance on the road between the Tx and Rx, φ will be higher at shorter L_s. Fig. 3.7 shows the BER as a function of φ_1 (angle of incidence with respect to Tx1 and Rx1, which will be same for Tx2 with respect to Rx2) for a range of d_{PD} and L_s. As can be observed, BER plot shows step responses i.e., rapid degradation due to φ_1 resulting from BSO. Note, the centre of the road lane is considered as the origin of the cartesian and spherical coordinate systems for calculating the positions of the Tx and Rx, and incidence angles, where φ_1 values to the left and right of the road lane are positive and negative, respectively. Moreover, the system performance is highly dependent on the geometry of the Tx and the Rx. As can be seen, the Rx with a larger d_{PD} allow higher degrees of misalignment between the Tx and the Rx i.e., larger φ. Note, at certain values of φ the BER tends to 0.5 as the optical signal or the beam spot from the lens is not captured by the PD (only the ambient light is). At certain φ_1 and L_s the following capturing scenarios are possible: (*i*) both Txs; (*ii*) a single Tx only; (*iii*) part of the Tx(s); and (*iv*) no Txs being detected by the PD. To minimize/overcome this effect, we propose the use of a spherical PD array Rx to provide a range of varying angular PD orientations with respect to the Tx with an azimuth and elevation curvature deflection angles of 91.4° (i.e. to cover φ_{hor} value of 45.7° to the right or left) and 28° (for coverage of φ_{ver} value of 14° to the top or bottom) considering a minimum L_s of 2 m, $\Delta H = 0.5$ m and $w_r = 3.75$ m, which is the largest width for the single road lanes. Note, with this method, lower values of φ can be achieved using a spherical PD array, as lower φ results in lower BSO see Fig. 3.5(a) and consequently a minimum BER degradation due to BSO.

3.2. Vehicular Visible Light Communications under the Effects of Atmospheric Turbulence with Aperture Averaging

In new part we experimentally investigated the effects of artmospheric turbulence (AT) with utilization of aperture averaging (AA) at the receiver on the performance of a VVLC link with a PD-based Rx under weak to moderate AT regimes.

Experimental investigation on AT with AA is carried out. The schematic block diagram of the proposed VVLC system with the PD- and camera-based Rxs with AA and under AT is depicted in Figure 3.7. The Rx1 is composed of a camera (Thorlabs DCC1645C-HQ) with a lens (Computar MLH-10X), and the Rx2 is composed of a PD (PDA100A2) and a convex lens. An indoor laboratory atmospheric chamber is used to simulate the outdoor AT. At the Tx, data packets of length 90 bits in the non-return to zero OOK format are generated using an arbitrary waveform generator, the output of which is used for intensity modulation of the TL (Truck-trailer DACA08712AM) via the driver module. The intensity-modulated light beam transmitted over a dedicated atmospheric chamber is captured at the Rxs. AT is generated within the chamber by varying the temperature along the transmission path using hot/cold fans. Seventeen temperature sensors are used within the chamber to measure the temperature distribution. The key experimental parameters adopted in the proposed system are listed in [95].
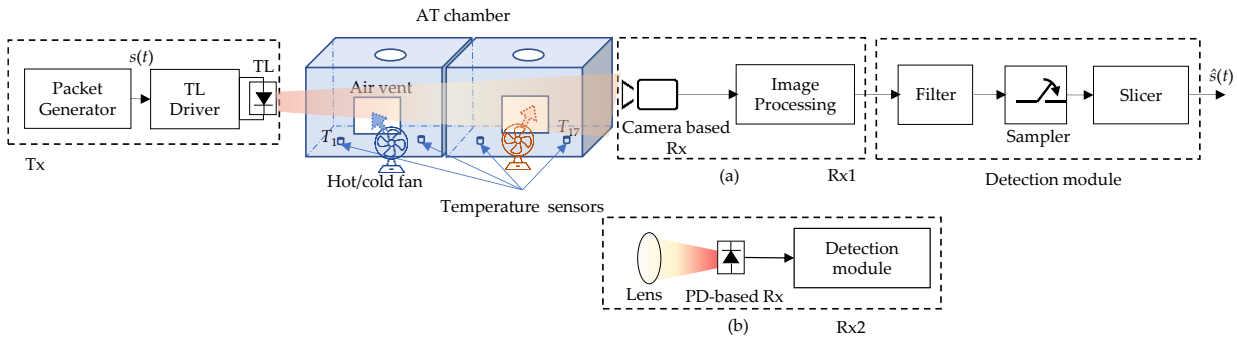
Figure 3.7. Setup of experimental investigation on AT effects on the VVLC link with: (a) camera, and (b) PD Rx

The histogram plots prior to the detection **camera module** are depicted in Figure 3.8(a)-(d), which illustrate the distributions of discrete intensity levels of the captured images within the range of 0 to 1 for the captured image frames per link.
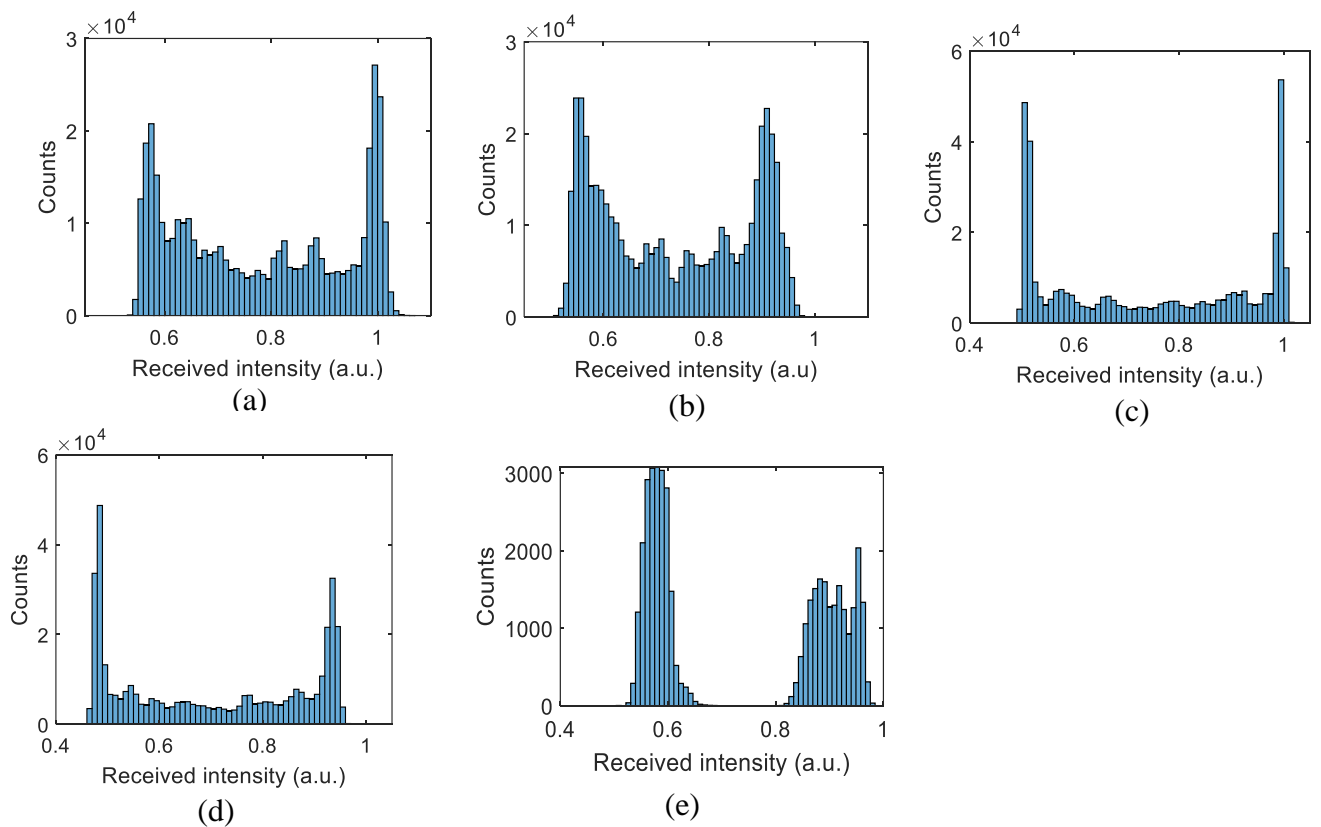

Figure 3.8. Camera Rx histogram plot: prior detection module for (a) gain 1.07× with no AT, (b) gain 1.07× with the highest AT scenario, $C_n^2 = 1.0 \times 10^{-10}$ m$^{-2/3}$, (c) gain 3.96× with no AT, and (d) gain 3.96×, with the highest AT scenario C_n^2 1.1×10^{-10} m$^{-2/3}$; and (e) output of sampler for (a)

Whereas Fig. 3.8(e) show the histogram for the sampled received intensity levels of Fig. 3.8(a) at the output of the sampler (i.e., within the detection module). Note the slight merge between the received intensities for the bits 0 and 1 in Figs. 3.8(a)-(d), which is due to the slow rise-time of the captured on and off states of the Tx. This is because of the transition between different illumination levels brought about by the sampling process in the RS-based camera [20]. Consequently, this happens at the transition edges, however for the proposed detection module, the sampling takes place at the centre of the received samples per bit; hence the system's performance is not degraded and bits 0 are 1 are clearly distinguishable as in Fig. 3.8(e). Moreover, it can be observed that, the link with a higher gain factor (i.e., Figure 3.8 (c) and (d)) have higher peak counts than Figure 3.8 (a) and (b) with the low gain factor.
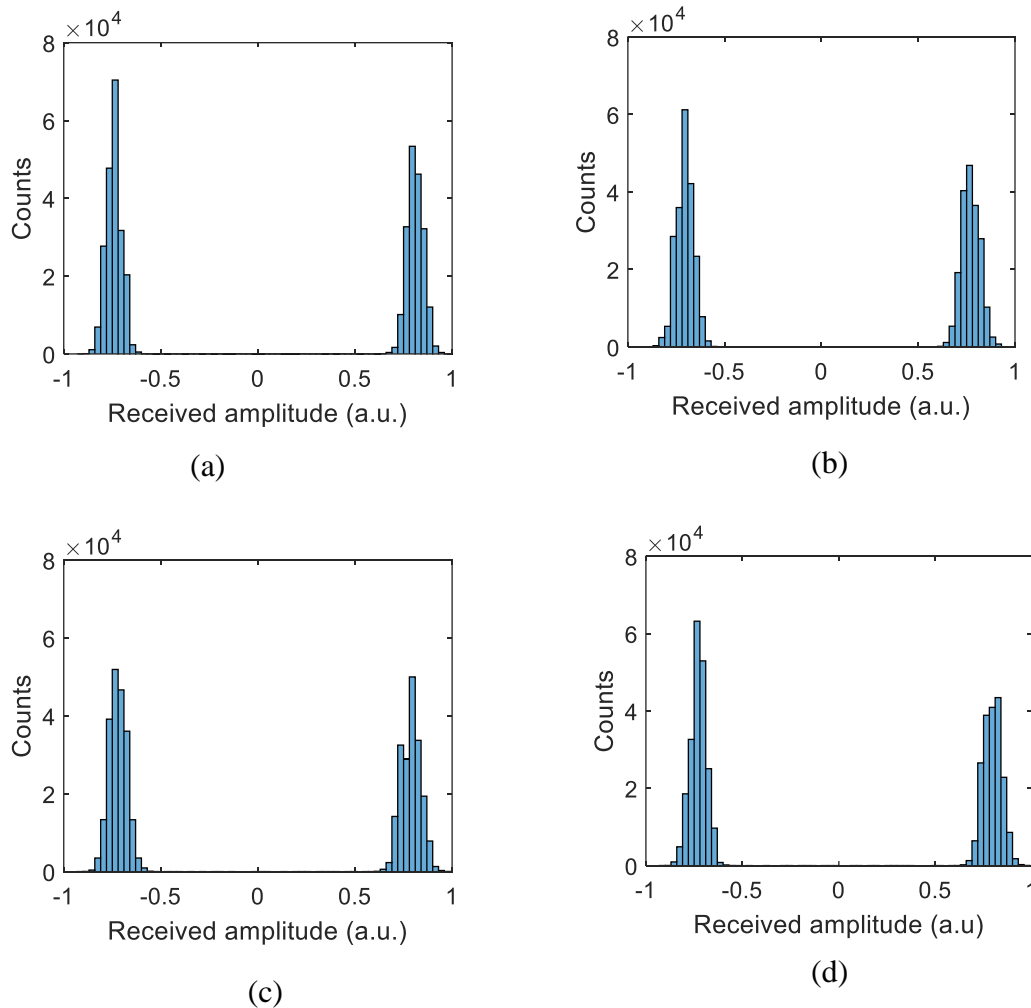

(a)

(b)

(c)

(d)

Figure 3.9. PD Rx histogram plot for (a) clear channel and with AT conditions of (b) $C_n^2 = 3.9 \times 10^{-11}$ m$^{-2/3}$ (c) $C_n^2 = 7.9 \times 10^{-11}$ m$^{-2/3}$ and (d) $C_n^2 = 1.0 \times 10^{-10}$ m$^{-2/3}$,

For the link with AA and the **PD-based Rx**, we have measured the SNR of the captured signals and produced histogram plots for bits 0 and 1, i.e., the signal distribution profile for the channel with and without AT as shown in Figure 3.9 prior the detection module. From the results obtained, (i) the histogram plot shows a clear distinction between the received signal for bits 0 and 1; and the average SNR is independent of the weak to moderate AT (with only ~0.1 dB of SNR penalty compared with the clear channel with OC). Thus, this demonstrates that AA can effectively combat the induced signal fading due to AT for the VVLC systems under weak to moderate turbulence regimes.

3.3. Conclusions Vehicular OWC

Relaying can be a viable option for vehicular OWC links to improve communication performance. We as well experimentally investigated the effects of aperture averaging for the VVLC link under turbulence using an LED-based vehicle's taillight. Results obtained showed that, with the aperture averaging there the system performance was not degraded under atmospheric turbulence, whereas both PSNR and SNR dropped by 0.7 and 0.1 dB for the camera- and PD- Rxs, respectively compared with the clear channel.

4. Radio signal over FSO

The exponential growth of global mobile traffic that needs to support interactive services, rich-video applications, mobile cloud, Internet of Things (IoT), and machine-to-machine (M2M) services, is expected to reach 5016 EB per month in 2030 [35]. In this sense, the estimated number of mobile and M2M subscriptions worldwide is expected to be of around 17.1 billion and 97 billion by 2030, respectively. Moreover, future mobile communications, i.e., sixth generation (6G) need to support extended reality and innovative scenarios, such as holographic-type communications, multisensory and tactile internet experiences. Therefore, to satisfy the performance criteria of 6G, more stringent technical requirements need to be met, including a user experience of 1 Gbps with minimal latency of 0.1 ms, and peak rates of 1 Tbps [36]. To fulfill these requirements, new key enabling technologies, architectures, air interfaces and virtual infrastructures will be required for the evolution of 5G-NR, capturing the interworking capabilities of enhanced mobile broadband (eMBB), massive machine-type communication (mMTC), and ultra-reliable low-latency communication (URLLC) [37]. Due to the congestion of lower microwave bands employed in conventional cellular services, a number of emerging technologies will be required to provide technical solutions for wireless communications, namely millimeter wave (mmW) and FSO. This deliverable aims to present the recent advances in mmW radio signal over FSO field trials proposed for such systems by several collaborations between research groups from different partners in COST action CA19111 NEWFOCUS.

In this context, next-generation wireless networks will experience a paradigm shift towards a network densification with smaller cells and higher volume of traffic by adopting centralized-radio access networks (C-RANs). However, some challenges need to be addressed to overcome the blockage in line-of-sight (LOS) in scenarios where multiple interferences between access points in high link densification and moving objects are present. Historically, radio over fiver (RoF) technologies have proven to provide high-capacity, high-speed and secure data

transmissions over long distances [38]. Given the technical performance of RoF technology over traditional data transmission systems, RoF has been considered a key enabling technology to overcome the problems with non-linear distortions associated with traditional radio frequency (RF) systems.

In RoF systems transmission of an optical mmW signal between the central station and base station is less feasible, particularly in rural and remote areas (i.e., geographical constraints) due to the high deployment cost and damaged cables (road works or earthquakes, e.g., Great East Japan Earthquake in 2011). The FSO communications technology [39] can be therefore adopted to solve the aforementioned issues in order to maintain seamless connectivity. FSO systems, which use air as a transmission medium, are very attractive compared to traditional wireless RF systems. FSO uses extremely narrow laser beams allowing for a high reuse factor, inherent security, and robustness to electromagnetic interference. The transmission of radio signals over FSO, so-called RoFSO [40], offers typical flexibility of wireless communications and speed of light transmission [41]. It also provides a higher level of coverage and mobility while employing THz carrier frequencies, which do not require license fees [39] and are an excellent alternative in areas where the optical fiber cannot be installed. Furthermore, the FSO link can be employed to transmit multiple wavelength division multiplexed (WDM) channels simultaneously. FSO is also a potential solution for the last-mile access networks and an attractive substitute for both optical fiber and RF communication systems.

The RoFSO technology was first introduced and demonstrated in 2006 as a possible option for optical fiber links to transport RF signals over short distances in [42], where modulated analog RF signals in the frequency range of 46 to 870 MHz was transmitted over a 3 m indoor FSO link and characterized the key performance parameters (i.e., carrier-to-noise ratio and spurious free dynamic range). However, the effect of atmospheric turbulence (AT) was not considered. Misalignments, so-called pointing errors, either due to building thermal expansion, wind, or weak seismic activity, among others, must also be considered and further compensated [43, 44]. FSO is highly affected by atmospheric phenomena, especially by thermal turbulence. The thermal distribution can vary significantly based on the daytime and as well within the urban environment due to several sources of heating [45, 46]. High thermal differences can be experienced, e.g., up 30 ºC [45], resulting in different turbulence levels in the vicinity of buildings, air conditions, highways, masts and in and over the street canyons. It is well-known that, the FSO link performance is highly affected by the AT strength, which is usually characterized by the refractive index structure parameter $C_n^2 (\mathrm{m}^{-2/3})$. In 2009, P. T. Dat et al. carried out complete and long-term RoFSO measurements with RF in the frequency range of 450 kHz to 420 MHz over a link span of 1 km in an outdoor environment with AT and compared with the analytical model [47]. Both experimental and numerical results showed a good agreement even under a strong AT regime.

For example, the atmospheric attenuation for signal wavelengths in the transmission window 1520–1600 nm is less than 0.2 dB/km with clear visibility [48], whereas the RF losses, strongly dependent on electrical frequency, lead to up to, e.g., 60 dB over 1 m at a 25 GHz frequency [49] with a particular antenna. In particular, FSO is affected by atmospheric turbulence created by temperature gradients [44-46, 50] occurring naturally in an outdoor environment. However, the thermal distribution can vary significantly along the FSO link especially in the cities as a result of the presence of sources of hot and cold air, e.g., rivers or highways, beneath the optical path. More specifically, the performance of FSO links, which are due to the flexibility widely deployed in dense urban areas, is affected by the buildings' heating and air conditioning and

the presence of watercourse or wind circulation in street corridors, etc. So far, only uniform turbulence regimes have been thoroughly studied in the literature [51].

Moreover, in the literature, optical frequency multiplying schemes for mmW signal generation based on different modulation schemes such as double-sideband (DSB) and carrier-suppressed double sideband (CS-DSB) have been employed to transmit such signals over RoF, RoFSO and a combination of both links. In [52], a 25 GHz 16-QAM DSB signal based on either direct or external modulation was transmitted over 100 m single mode fiber (SMF) and 50 m long outdoor mmW links with the signal bandwidth limited to 20 MHz. In [53], a CS-DSB scheme for doubling the frequency to obtain the 40 GHz mmW signal with a 2 GHz bandwidth over a 20 km SMF was experimentally demonstrated. However, the 32-QAM signal was only evaluated at the intermediate frequency (IF) of 2 GHz. In [54], a simple RoF link (20 km) with 3.5 Gbps on-off keying, which is not used in 5G networks, a downstream link using the 72 GHz mmW based on all-optical CS-DSB frequency eightfold technique and a single external Mach-Zehnder modulator (MZM) was reported. A 60 GHz 4- and 16-QAM DSB signals with a bandwidth up to 400 MHz over a SMF were investigated in [55]; however, fiber distance was limited to a 1 km of SMF, which is relatively short for optical fronthauling in 5G. In [56], the transmission of the 5G new radio (NR) standard signal of 26 GHz 16-QAM DSB with a bandwidth of 400 MHz over a 12.5 km of SMF, as well as 1 and 8 m long FSO and RF wireless channels, respectively was reported.

In [53] and [54], the transmission of 25 GHz quadrature phase shift keying (QPSK) and 16/64-QAM signals using CS-DSB-based frequency doubling technique was also demonstrated over SMF, FSO and RF wireless links focusing on the impact of AT on the FSO link. The signal performance was directly evaluated at 25 GHz; although an LTE signal was used with a 20 MHz bandwidth so, thus, the potential toward incoming telecommunication standards is limited. Moreover, a full-duplex hybrid microwave photonic link (HMPL) system using an optical heterodyne method for 60 GHz 16- and 64-QAM signal transmission over a hybrid 25 km SMF, 1m FSO, and 1m RF wireless link was presented in [57]; however, the data rate (Rb) was limited to 80 Mb/s and 120Mb/s, respectively. A transmission of 80 Gb/s and 41 Gb/s filter bank multi-carrier signals over the downlink (DL) and uplink (UL) direction was carried out in [50] using a 20 km SMF, 1.5 m FSO, and 1 m RF wireless link [58]. However, the DL and UL signals were transmitted separately, and complex optical in-phase-quadrature modulators were used for data modulation, which makes the HMPL bulky and costly. The transmission of 26 GHz 5G NR signal over a hybrid system was demonstrated in [56] using 12.5 km SMF, 1 m FSO, and 8 m RF wireless link. Nevertheless, only DL transmission was implemented and Rb was limited to 1.2 Gb/s. Notably, there are no reported HMPL systems that employed (i) low-cost directly modulated laser (DML) for data modulation, (ii) optical frequency multiplication (OFM) technique to avoid the use of high-frequency RF components, and (iii) composite subcarrier multiplexed (SCM) signals for multiple-user services. In our previous work [53], we employed a DML and OFM technique for the demonstration of three-user transmission over 10 km SMF using the uniform 16-QAM allocation. However, only DL transmission was demonstrated, and Rb was limited to 0.8 Gb/s.

4.1. Impact of Thermal-induced Turbulences in FSO on Photonically Generated mmW Signals

In [59], different thermal distributions along the FSO link have been implemented and Gamma-Gamma model [60] has been employed to estimate the thermally induced turbulence [61]. As expected, the results show high electrical power decrease and fluctuation of the generated mmW signal according to the particular level of the turbulence in terms of refractive index structure parameter and thermal distribution along the FSO link.
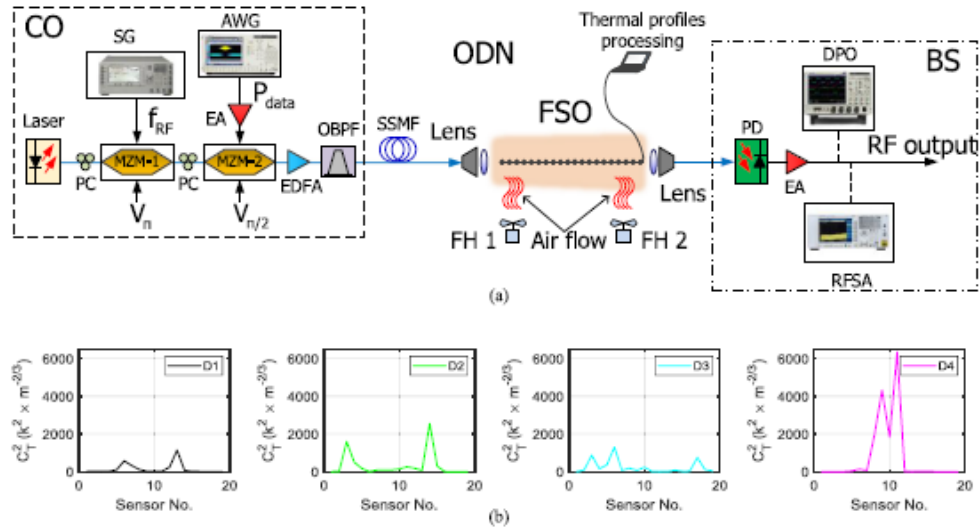

Fig. 4.1. (a) Experimental setup (CO: central office, ODN: optical distribution network, PC: polarization controller, MZM: Mach–Zehnder modulator, AWG: arbitrary waveform generator, EA: electrical amplifier, EDFA: erbium-doped fiber amplifier, OBPF: optical bandpass filter, SSMF: standard single mode fiber, FSO: free-space optics, FH: fan heater, PD: photodetector, RFSA: RF spectrum analyzer, DPO: digital phosphor oscilloscope), and (b) C_T^2 distributions.

The experimental setup of mmW signal transmission over a hybrid optical link of standard single mode fiber (SSMF) and FSO is shown in Fig. 4.1(a). A distributed feedback (DFB) laser (EXFO IQS) at a wavelength of 1550.12 nm with an output optical power of 10 dBm provides the optical carrier. A polarization controller (PC) adjusts the state of polarization to minimize MZM-1 (Photline MX-LN-40) losses. MZM-1 is biased at null transmission point (half-wave voltage, $V\pi$), i.e., at 6.4 V, to obtain the CS-DSB modulated signal. The optical carrier is then modulated by an RF, f_{RF}, which is generated by a signal generator (Agilent PSG E8267C) with an output RF power of 22 dBm. The experimental setup employs another PC before a second modulator, MZM-2 (Avanex PowerBit F-10), which is biased at the linear point (quadrature voltage $V\pi/2$), i.e., 5.8 V. The optical signal is then modulated by the data generated by an arbitrary waveform generator (AWG, Tektronix AWG7122C). Note that the data signal with 28 dBm output power is amplified by a 12 dB gain RF electrical amplifier (Minicircuits ZX60-14012L-S+). The modulated optical signal is amplified by an erbium-doped fiber amplifier (EDFA, Amonics EDFA-23-B-FA) with 13 dBm output power and filtered out by an optical bandpass filter (OBPF, Finisar Waveshaper 4000S) having a bandwidth of $\Delta\lambda = 1.5$ nm to reduce amplified spontaneous emission. The signal is then launched into 1.4 km long SSMF what is followed by a 1.2 m long FSO channel using a pair of air-spaced doublet collimators (Thorlabs F810APC-1550). The FSO link loss is 4.5 dB, which is significantly lower compared to free space propagation of radio waves in the mmW band.

Artificial turbulence is produced on the FSO channel according to four different spatial temperature distributions (D1–D4), as shown in Fig. 4.1(b). The distribution is expressed in terms of the temperature structure parameter C_T^2 distribution along the link. Turbulence is generated by two fan heaters introducing temperature gradients into the FSO channel and measured by 20 temperature sensors equidistantly located along the FSO link with 0.06 m spacing. These distributions represent inhomogeneous temperature profile when the collimated laser beam propagates in FSO link through differently heated areas, according to Fig. 4.1. D1 introduces almost uniform turbulence along the link, whereas in the case of D2 and D3, the fans' thermal flow was set in order to reach increased thermal gradient close to the Rx and Tx, respectively, which can be induced e.g., by thermal flow close to the building/masts of transmitting/receiving FSO heads. Finally, D4 represents peak turbulence in the middle of the link, which can be caused e.g., by an increased airflow over the street canyons, roads or air-condition outlets as indicated in Fig. 4.1.

According to photonic mmW signal generation approach based on external CS-DSB modulated signals [62], the mmW signal $f_{mmW} = 2f_{RF}$, is generated after beating the modulated sidebands at photodetector (PD, Finisar BPDV2020R) and subsequently, it is amplified by an RF electrical amplifier (SHF-810). The mmW signal is analyzed by an RF spectrum analyzer (RFSA) showing the RF signal potentially launched to an antenna located in the C-RAN BS infrastructure.
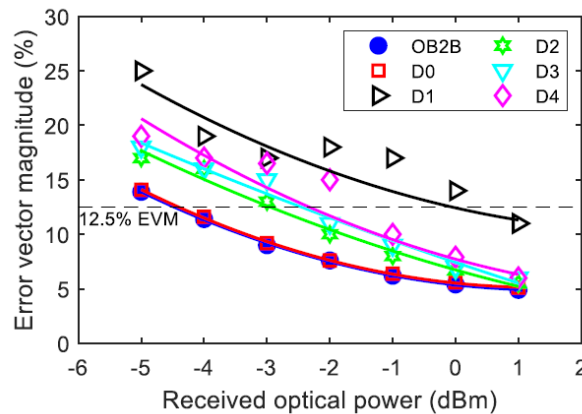

Fig. 4.2. Measured EVM for different links and temperature distributions for 8 Gb/s 16-QAM signal over 40 GHz mmW signal.

Fig. 4.2 plots the obtained EVM versus the received optical power at PD input for all tested scenarios. Since only 1.4 km SSMF and 1.2 m long FSO channel are employed, there is no significant power penalty between optical back-to-back (OB2B) and D0. The EVM values of OB2B and D0 (without induced turbulence) are kept below the limit of 12.5% for optical power up to −4.3 dBm at the optical Rx whereas minimum EVM of 5% is measured for a received power of 1 dBm. The largest EVM impact of turbulence has been obtained under D1 temperature distribution which represents evenly distributed turbulence along the channel. The power penalty is in this case almost 5 dB at 12.5% of EVM, compared to D0. The EVM can be kept below 12.5% for received optical power up to -2.1 dBm for D2, D3 and D4 when turbulence highly influences the areas closer to the Rx and Tx or exhibit a peak in the center of the link, respectively. However, at least 0.3 dBm of received optical power is required for D1. Note that, despite the high phase noise level and low electrical power measurements in this scenario, the conducted measurements showed that evenly distributed turbulence in the FSO link has the highest impact on EVM performance in such system and the distribution of scintillations along the link also plays a key role in the signal transmission penalty.

In the following, a further experimental study of the impact of non-uniform turbulent distribution along the FSO link on the transmission of M-QAM signals with M=4, 16, and 64 in K-band (25 GHz) [62], which are photonically generated by using an optical external intensity modulator biased at the null transmission point was performed.
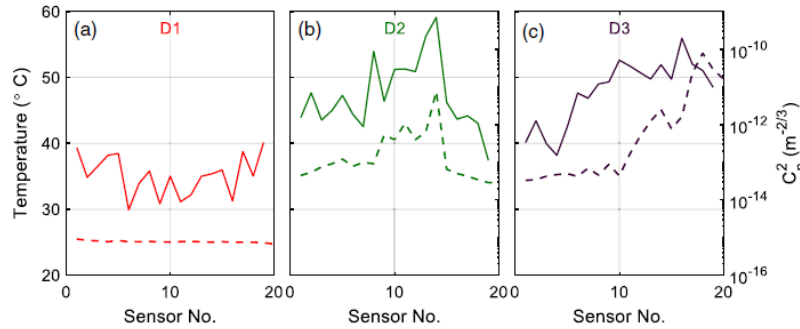

Fig. 4.3. Experimental temperature (dashed line) and C_n^2 (solid line) distributions for different scenarios: (a) D1, (b) D2, and (c) D3.

Three experimental turbulence scenarios of the FSO link D1, D2, and D3 were created in this case within a laboratory chamber where thermal distribution was captured by thermal sensors equidistantly spaced in 10 cm steps and the corresponding refractive index structure parameter, C_n^2, was calculated along the link (see distributions in Fig. 4.3). While almost flat distribution was set in the case of D1 with $C_n^2 = 5.9 \cdot 10^{-14} \ m^{-2/3}$ ($\sigma_R^2 = 1.3254 \cdot 10^{-5}$, low turbulence), D2 and D3 correspond to turbulence distributions with a turbulence peak in the middle of the link and increased turbulence in the last part of the link. The averaged C_n^2 values were $4.2 \ 10^{-11} \ m^{-2/3}$ and $1.8 \cdot 10^{-11} \ m^{-2/3}$ and, therefore, corresponding $\sigma_R^2 = 0.0094754$ and $\sigma_R^2 = 0.0041495$ for experimental D2 and D3 scenarios, respectively. Note that lower σ_R^2 values and higher C_n^2 values compared to the simulation results were obtained due to a considerably shorter FSO path, i.e., 2m long, in the experiment.
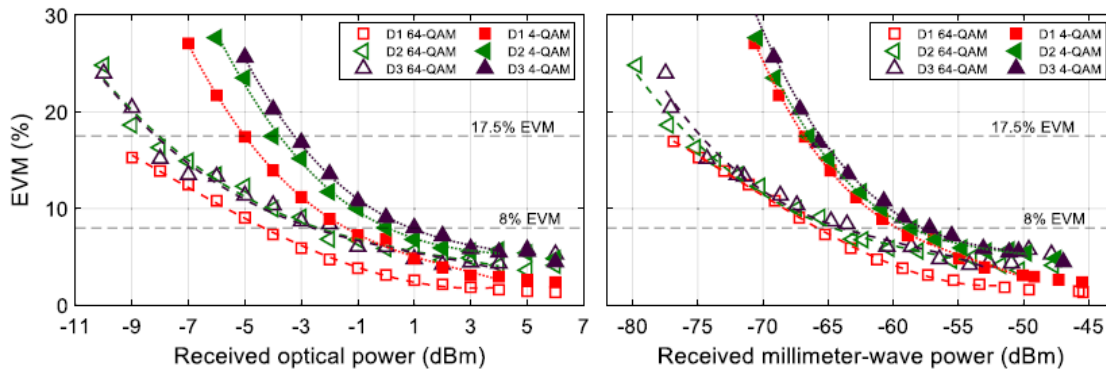

Fig. 4.4. Experimental EVM vs. received (a) optical and (b) electrical power for 4-QAM and 64-QAM modulation formats.

Fig. 4.4 shows the measured EVM versus the received optical power for 4- and 64-QAM. We can observe that EVM values are higher for 4-QAM, as obtained in the simulation results. Nevertheless, 4-QAM has a significantly higher EVM limit to obtain reliable transmission. Both modulation formats lead to less degradation under low turbulence (D1 scenario) and similar degradations for D2 and D3, as expected due to the similar turbulence level magnitude. Standard EVM limits, displayed as the dashed horizontal lines, for 4- and 64-QAM are satisfied under the D1 scenario with a received optical power of -5 dBm and -4.33 dBm, respectively. However, the power penalties with respect to D2 and D3 scenarios at the 17.5% EVM level for 4-QAM are 1.3 dB and 1.8 dB respectively, whereas the power penalties at the 8% EVM level

for 64-QAM are 1.9 dB and 1.7 dB. Note that D2 and D3 scenarios with 0 dBm received optical power leads to a 3.7% and 4% EVM difference between 4- and 64-QAM formats, respectively. Figure 4.4(b) shows the EVM results in terms of received electrical power measured at 25 GHz where 4- and 64-QAM required a minimum electrical power of -65.7 and -66.1 dBm, respectively, showing penalties lower than 0.94 and 1.7 dB for D2 and D3 in both cases.

Moreover, we proposed and investigated for the first time a seamless mmW RoF and radio-over-free-space optics-based downlink for use in a passive optical network architecture using 4-, 16- and 64-quadrature amplitude modulation for broadband wireless access (BWA) networks [63].
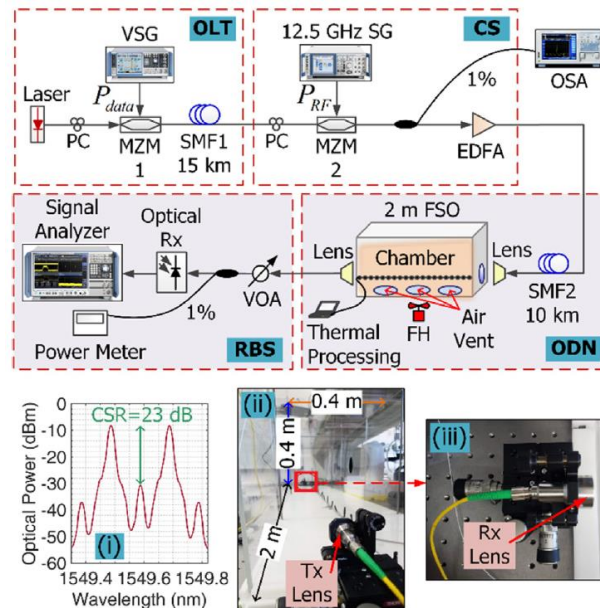

Fig. 4.5. Experimental setup of a hybrid 25 GHz RoF-FSO downlink. PC: polarization controller, OSA: optical spectrum analyzer, EDFA: erbium-doped fiber amplifier, FH: fan heater and VOA: variable optical attenuator. Insets show (i) optical spectrum, (ii) turbulent chamber/Tx lens and (iii) Rx lens.

Here, we only focus on the RoF-FSO downlink for use in BWA in rural areas. The proof-of-concept experimental setup is shown in Fig. 4.5, which consists of four sections of optical line terminal (OLT), central station (CS), optical distribution network (ODN) and remote base station (RBS). In OLT, the M-QAM signal at an IF of 200 MHz is first generated by using a vector signal generator (R&S SMW 200A). The signal is then used for external modulation of a continuous wave laser beam via a PC and a single-drive MZM (MZM 1 – Fujitsu FTM7938EZ/201) with a half-wave voltage of 3.5 V. Note that, 4-, 16- and 64-QAM have R_b of 34, 67 and 100 Mb/s, respectively with an output power P_{data} of 7 dBm.

The modulated signal transmitted over a SMF1 (15 km) is further externally modulated using another single-drive MZM (MZM 2 – Covega 10™ 081) with a half-wave voltage of 8 V by a 12.5 GHz RF clock signal from a signal generator (R&S SMF 100A) with an output power of 23 dBm. It is well-known that the physical properties of the MZM are easily affected by the change of external environment, which results in the drift of its bias point and therefore affects the performance. In this work, prior to measurements, we properly adjusted the bias voltage level applied to MZM 2 and monitored the electrical mmW spectrum over time on the signal and spectrum analyzer at the optical Rx. The most stable bias voltage value was adopted. Note, MZM 2 is biased at the minimum transmission point and its output optical spectrum is the two optical-tone signal with 25 GHz frequency spacing — see inset (i) in Fig. 4.5. The measured

CSR is 23 dB at a bias voltage of 2.9 V, which is adopted for all M-QAM for a fair comparison. Following amplification by an EDFA, the output of the MZM 2 is transmitted over a 10 km SMF2 to ODN. The optical signal at the SMF2 output is launched into a 2 m FSO channel via an optical lens — see insets (ii). A second lens is used at the end of the channel to capture the light for transmission over SMF — see inset (iii). Note that, both of them are air-spaced doublet lens (Thorlabs F810APC-1550) with an aperture diameter and focal length of 2.54 and 3.71 cm, respectively. The FSO link loss is about 4 dB. It is worth to mention that longer FSO distance would require advanced optical beam coupling techniques at the receiving side in order to reduce the beam size and obtain low loss coupling from a wider beam.

For the generation of non-uniform AT, an external fan heater positioned at the center of the chamber is used to blow hot air perpendicularly to the propagating light beam via a central air vent. Two air vents at each end of the chamber are used for heat dissipation (i.e., controlling the AT level). To accurately measure the thermal profiles within the chamber, 20 thermal sensors are equidistantly placed (i.e., $d = 10$ cm) along the chamber.
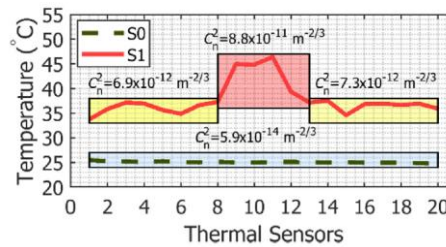

Fig. 4.6. Thermal profiles in case of uniform S0 and non-uniform S1 AT.

Fig. 4.6 shows the temperature profiles for two AT cases of low-level uniform S0 and non-uniform S1. The recorded temperature is processed offline to determine C_n^2 which is also illustrated in Fig. 4.6. Note, σ_R^2 can also be easily determined in order to scale the measurements for the outdoor environment. For S0, with a mean temperature of ~25 °C, the resultant C_n^2 is 5.9×10^{-14} m$^{-2/3}$. For S1, we set the highest temperatures at the center of the chamber with a peak temperature of ~47 °C and thus C_n^2 of 8.8×10^{-11} m$^{-2/3}$, which is more than three orders of magnitude higher compared to S0. Regarding the lower temperature profiles of 33–37 °C on either side of the chamber, the resultant C_n^2 are 6.9×10^{-12} m$^{-2/3}$ and 7.3×10^{-12} m$^{-2/3}$. At RBS, a variable optical attenuator (VOA) is used to adjust the received optical power P_r level prior to detection using a 38 GHz PIN PD (New Focus 1474-A). The regenerated mmW signal is captured using a signal and spectrum analyzer (R&S FSW) for signal assessment.
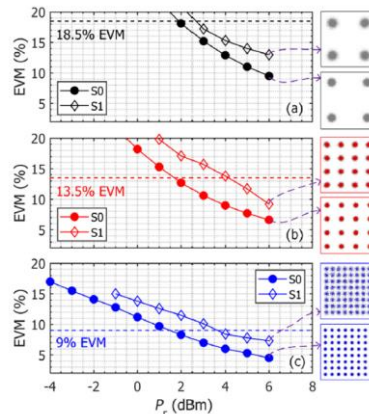

Fig. 4.7. EVM versus received optical power for: (a) 4-, (b) 16- and (c) 64-QAM transmissions. Insets show corresponding constellation diagrams at P_r of 6 dBm.

Figs. 4.7(a), (b) and (c) show the measured EVMs as a function of P_r for the M-QAM RoF-FSO downlink under S0 and S1. For S0, the EVM values are about 9.5, 6.6 and 4.5% at P_r of 6 dBm, which increased by 3.5, 2.5 and 2.8%, respectively for S1. Note that, all EVM values are well below the corresponding required EVM limits for $P_r > 4$ dBm, thus confirming the practicality of the proposed RoF-FSO downlink in the Passive Optical Network (PON) architecture for ubiquitous coverage. In addition, we measured the M-QAM constellations for P_r of 6 dBm as shown in insets of Fig. 4.7. Note, AT results in the spreading of the symbol size, which in turn induces a power fading on the received electrical M-QAM spectrum.

4.2. Experimental Trials with Different Modulation Formats in the Photonic mmW Signal Generation Module

We investigate the transmission of 5G NR signals at 39 GHz for DSB and CS-DSB schemes over the combined analog RoF and RoFSO link [64]. In addition, we experimentally demonstrate the implementation of 5G optical fronthaul with the hybrid SMF and FSO link at 3.5, 27, and 39 GHz bands.
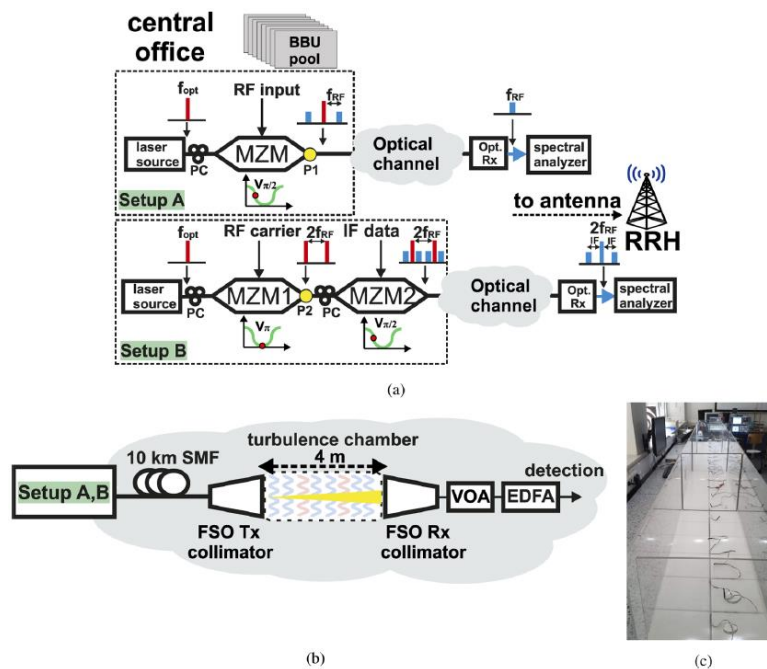

Fig. 4.8. (a) Setups A and B for an optical fronthaul network, (b) the full configuration of the optical channel, and (c) turbulent chamber.

We have tested two setups for performance comparison of the mobile mmW fronthaul network as illustrated in Fig. 4.8(a). Both setups employ a continuous wave (CW) laser signal source (CoBrite DX4) with 16 dBm of output optical power. In Setup A, representing a classic analog MPL with DSB modulation and direct detection (DD), a 5G NR mmW signal at a particular carrier frequency is produced by a vector signal generator (R&S SMW200A) and applied to the MZM (Optilab IML-1550-50-PM), which is biased at its quadrature point. The output optical power of the MZM is 7 dBm. In Setup B, a radio signal at the half of the target carrier frequency, i.e., 12.5 GHz for 27 GHz and 18.5 GHz for 39 GHz transmission, produced by a signal generator (R&S SMF100A) is applied to MZM1 (Fujitsu FTM7938EZ/201), which is biased at its null point. The CS-DSB signal is led to low-speed MZM2 (Covega 10TM 081), which is biased at its linear point and modulated by the 2 GHz IF data signal from a vector signal generator (R&S SMW200A). The externally modulated optical signal with a power of -2 dBm

is launched into the optical channel for transmission. In both Setups, the optical signal is directly detected at the optical Rx (Optilab PD 40) and the resulting converted signal is captured by a signal analyzer (R&S FSW) for performance assessment. In the case of setup B, the beating of the optical sidebands at the optical Rx generates the signal at the double frequency of the original signal, i.e., 25 and 37 GHz with an additional IF of 2 GHz. Note that, due to the lower output optical power level in Setup B, an EDFA is required while in Setup A, the EDFA is only used when the FSO link is included. The optical channel used in Setups A & B consists of a fixed 10 km long SMF reel, providing a satisfactory range for connection between a central office (CO) and remote radio head (RRH), and a 4 m long FSO link as depicted in Fig. 4.8(b), to demonstrate a proof of concept. The latter offers a flexible solution to establish connectivity in high-density urban areas where burying fibers is costly and time consuming. The FSO link is composed of the Tx and the Rx with optical doublet collimators (Thorlabs F810APC-1550) for launching and capturing the optical signal from and to the optical fiber, respectively. A laboratory AT chamber with controlled temperature distribution is employed for the FSO channel.
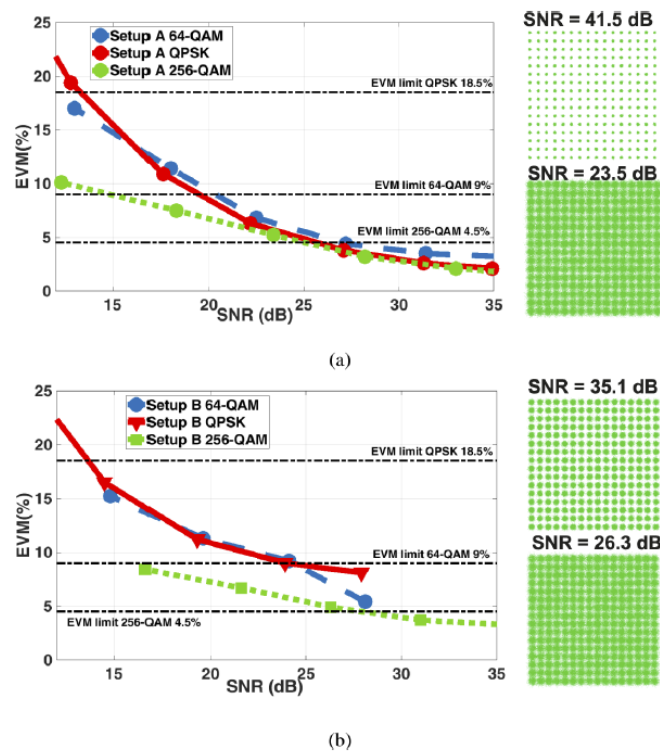

Fig. 4.9. EVM versus the SNR at 27 GHz for: (a) Setup A, and (b) Setup B. Inset are the constellations for 256-QAM at maximum SNR values and behind the edge of the EVM limit.

We have investigated the EVM as a function of signal-to-noise ratio (SNR) for both setups at 27 GHz, as illustrated in Fig. 4.9. To measure the SNR, a combination of an electrical attenuator at the input stage and a signal analyzer at the Rx was adopted. Following the 5G NR standard, we evaluated 90 MHz bandwidth using 256-QAM, and 400 MHz bandwidth using QPSK and 64-QAM. As expected, the EVM results for QPSK and 64-QAM show similar trends in both setups, since they have identical bandwidth of 400 MHz, however, each is subject to a different EVM limit. The highest required SNR is observed for 256-QAM. This is because the bandwidth is only 90 MHz comparing to 400 MHz for a fixed RF input power, i.e., 7 dBm, resulting in the highest power spectral density compared to the 400 MHz bandwidth. The 256-QAM transmission in Setup A offers improved performance in terms of the gain in the maximum SNR by 6 dB, and lower EVM by 2% compared with Setup B. In Setup A, the lowest EVM

values of 1.3 and 2.1 % at the SNR of 35 dB are observed for 256-QAM/QPSK, and 64-QAM, respectively. In Setup B, the lowest EVM values are achieved at SNR of 28 and 35 dB for 64-QAM/QPSK, and 256-QAM, respectively. Thus, in both setups, 256-QAM with 90 MHz bandwidth offers the best performance in terms of EVM, which is confirmed by the constellations shown for the selected SNR values.

4.3. Transmission Trials in Bidirectional Networks

In [65] we demonstrated an M-QAM orthogonal frequency-division multiplexing (OFDM) bidirectional 60/25 GHz transmission over 10 km Fiber, 100 m FSO and 2 m radio seamless heterogeneous fronthaul link.
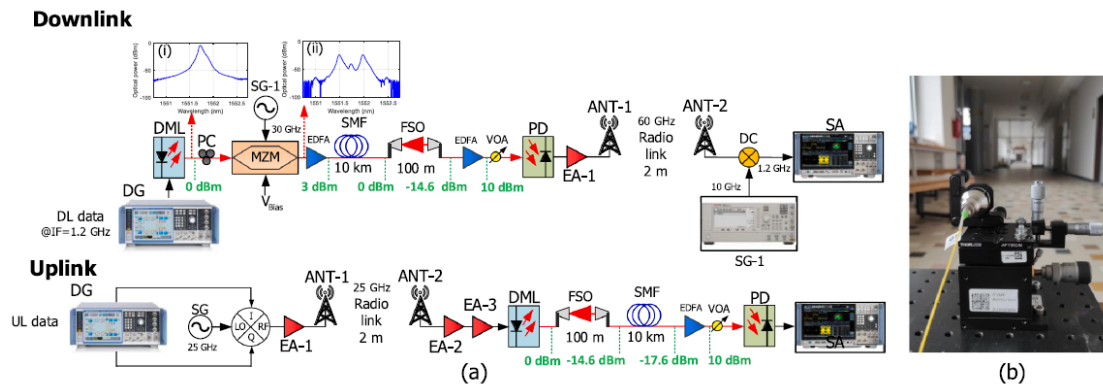

Fig. 4.10. (a) Experimental setup: Downlink at 60 GHz and uplink at 25 GHz bands and (b) Photograph of the coupling from fiber to FSO. Insets show the signal spectra: (i) DML output, (ii) MZM output. DG: digital generator, DML: directly modulated laser, PC: polarization controller, MZM: Mach-Zehnder modulator, SG: signal generator, SMF: single mode fiber, FSO: free space optics, EDFA: erbium doped amplifier, VOA: variable optical attenuator, PD: photodetector, EA: electrical amplifier, SA: signal analyzer.

A heterogeneous system for mmW signal transmission based on a 10 km SMF, 100 m FSO and 2 m radio seamless wireless links was set up to demonstrate bidirectional signal performance. The proposed setup is shown in Fig. 4.10. As depicted in Fig. 4.10(a), the DL employs a DML, which is a monolithically-integrated passive feedback laser described in [66], centered at 1551.7 nm (the optical spectrum is shown in inset (i) of Fig. 4.10) and driven through a bias tee (SigTek SB12D2) by an electrical M-QAM OFDM long term evolution (LTE) data signal carried by an IF of 1.2 GHz which is generated by a vector data signal generator (DG, R&S SMW200A). The MWPG approach based on carrier-suppressed external modulation is employed for the frequency up-conversion of the DML output signal where the frequency of the electrical driving signal at the Mach-Zehnder modulator (MZM, Optilab IML-1550–50-PM) is $f_{RF} = f_{mmW}/2 = 30$ GHz, where f_{mmW} is the target frequency band. The MZM output signal, whose spectrum is shown in inset (ii) of Fig. 4.10, is transmitted over the 10 km long SMF section and the FSO link, which was realized by two doublet collimators (Thorlabs F810APC-1550) with the total FSO insertion loss of 14.6 dB. Note that the FSO link was tested indoor so that any environmental effect could be neglected. After the FSO link, the signal is launched into an EDFA to compensate for the optical losses as a post-amplification stage, and then a VOA allows to adjust the received optical power (RoP) after the EDFA. Note the EDFA can also be placed at the transmitting side, which is a cost-effective deployment due to the possibility to share resources. The PD, Finisar XPDV3120) performs the opto-electrical conversion where both $\pm f_{RF}$ sidebands of the modulated optical signal beat each other to generate the desired $f_{mmW} = 2f_{RF} \pm f_{IF}$, where lower and upper data bands are located at 58.8 GHz and 61.2 GHz, respectively. Then, the signal is amplified by a low-noise electrical

amplifier (EA, SAGE SBL-5037033550-VFVF-S1) and radiated by a pyramidal horn antenna (RF spin, H-A90-W25) over a 2 m long wireless radio link. Finally, the same type of the receiving antenna allows the signal reception, and the further analysis is accomplished in the signal analyser (SA, R&S FSW). An electrical down-converter (DC, R&S FS-Z90) is used before the signal analysis due to the frequency limitation of the available instrumentation. The experimental parameters are fully detailed in Table 2 for every component employed in the setup. Fig. 4.10(a) shows the setup for the UL operating at 25 GHz, which employs the same DG as in the DL to generate a fixed I/Q signal output which is combined with the local oscillator signal at 25 GHz by using an RF mixer. Note that the DL and UL were not measured simultaneously. The resulting signal is amplified by EA-1 (Wisewave AGP- 33142325–01) and transmitted by a double ridged horn antenna (RF spin DRH40) through the 2 m long wireless radio link. The received signal is amplified in two identical cascaded amplifiers (MITEQ AMF-4F- 260400–40-10P) and launched into the DML, which is already described above, for electro-to-optical conversion prior to transmission over the wired and wireless optical links. The high bandwidth of the DML is here fully used to represent an effective solution for a low complexity UL system compared to the conventional usage of external modulation. In general, compared to the use of MZM, direct modulation offers satisfactory RF to optical conversion efficiency and linearity but has relatively low output power and the modulation chirp is generally higher. Finally, an EDFA and a VOA are also used to compensate the losses and adjust the optical power at the PD, which performs the opto-to-electronic conversion. The recovered data are then analyzed in the SA.
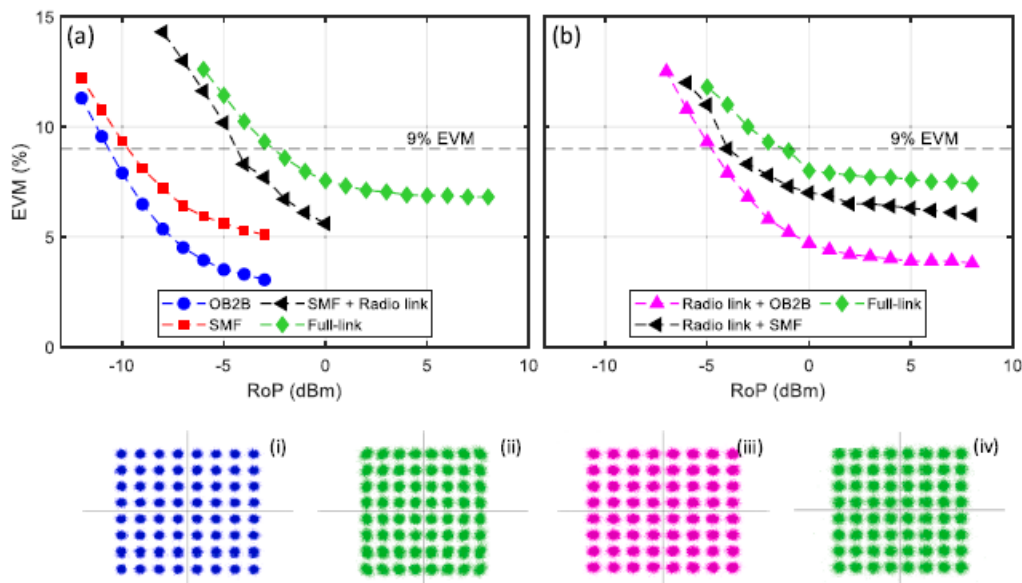

Fig. 4.11. EVM vs RoP for 64-QAM with different configuration in both links: (a) 61.2 GHz DL (b) 25 GHz UL. Corresponding insets show constellations for DL: (i) OB2B (RoP = -3 dBm), (ii) full-link (RoP = 8 dBm); and for UL: (iii) radio and OB2B (RoP = 3 dBm), (iv) full-link (RoP = 9 dBm).

Both the DL and UL performances were characterized by measuring the dependence of the EVM on the received optical power (RoP) for a 64-QAM signal transmission in the 60 GHz band (DL) and in the 25 GHz band (UL). Note that according to the previous section, the DL OB2B scenario employed different P_{data} compared to other DL scenarios, i.e., 5 dBm vs -12 dBm, so the comparison between them is not straightforward. The results, illustrating the EVM dependence on the RoP obtained by introducing the optical loss of the VOA, for the DL and UL with a 64-QAM are depicted in Fig. 4.11. As expected, Fig. 4.11(a) shows that the DL EVM decreases with the increasing optical power while the SMF + radio and full links imply a power penalty at the 9 % threshold of 5 and 7 dB, respectively, with regards to the SMF scenario

power level. This is because the SMF + radio and full link both contain the 2 m long radio link at 61 GHz, which deteriorates the overall EVM performance. The results imply that for the full-link scenario, the acceptable transmission quality requires a minimum RoP of -2.7 dBm. Note that the additional optical loss, introduced by the VOA, is 11 dB in this case. Fig. 4.11(b) then shows the EVM dependence on the RoP for UL where a penalty of 1.5 and 3 dB is observed when the SMF and full links are introduced, respectively, with regard to the OB2B scenario. The required RoP, in this case, is -1 dBm for the full link operation to keep the EVM below 9%. Note that the maximal additional optical insertion loss is 10 dB in this case and thus 1 dB lower compared to the DL. The difference among particular UL scenarios is less significant, compared to the DL, because the radio link is involved in all of them due to the UL definition. Insets (i) and (ii) then show the 64-QAM constellations for the DL under the OB2B and full-link scenarios, respectively, while (iii) and (iv) depict the constellations for radio link + OB2B and full-link scenarios in UL, respectively. It should be emphasized that the transmission over the full link in both the DL and UL setup fulfils the given EVM limit for a wide range of the RoP.

Moreover, in NEWFOCUS, we have also carried out full-duplex transmission of multi-Gb/s subcarrier multiplexing and 5G NR signals in 39 GHz band over fiber and free space [67].
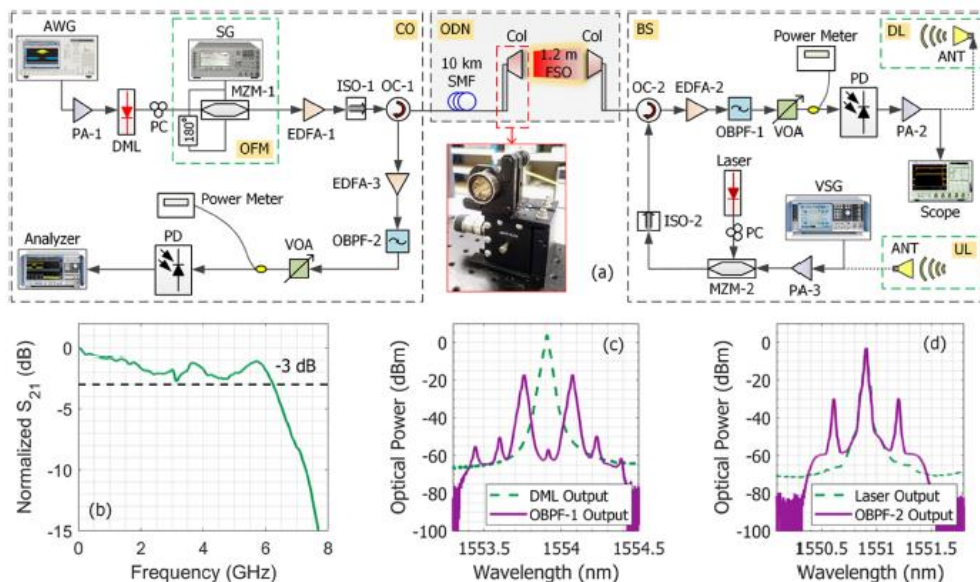

Fig. 4.12. (a) Experimental setup of the proposed full-duplex HMPL-based 5G mmW FWA networks, (b) DML frequency response, (c) optical spectra measured in DL, and (d) optical spectra measured in UL.

Fig. 4.12(a) illustrates the experimental setup. For the DL direction, in the CO, both single and multiple user signals were evaluated. The latter was generated at different IFs and added together to form a composite SCM signal by using an arbitrary waveform generator (AWG, Tektronix AWG7122C). The multiplexed signal was then electrically amplified by an RF power amplifier (PA-1, Wenteq ABL0300-01-2516) up to 9 dBm. Note that the transmitting power of all used amplifiers was set to not saturate them and thus avoid a significant nonlinear distortion. The signal was applied to a non-chirp DML (OpticalZonu OZ516) having a 3 dB bandwidth of 6 GHz and a fixed power of 5.6 dBm at λ of 1553.9 nm; see Fig. 4.12(b). The optical spectrum at the DML output is shown in Fig. 4.12(c). The optical signal was then launched to an OFM module, which can be reused for future high-frequency and high-capacity wavelength-division-multiplexing systems.

Here we adopted the optical frequency doubling based on a dual-electrode MZM (MZM-1, Sumitomo T.DEH1.5-40PD-ADC), biased at the null transmission point (i.e., 9 V) to generate a CS-DSB signal. The MZM-1 was driven by a 19.5 GHz input clock signal, generated by a signal generator (SG, Agilent 8267C) via an electrical 180_ hybrid coupler. The input clock power was set at 23 dBm. The PC was used to minimize the polarization-dependent loss. The data-modulated signal was amplified by an erbium-doped fiber amplifier (EDFA-1, AccelinkMWseries) with a constant gain of 20 dB to compensate for the modulation loss and boost the optical power prior to signal transmission over the ODN via the optical isolator (ISO-1) and the directional optical circulator (OC-1) to prevent any signal reflection.

The ODN consisted of a 10 km SMF, the output of which was launched into a 1.2 m FSO link by using a pair of air-spaced doublet collimators (col, Thorlabs F810APC-1550) with an aperture diameter and focal length of 2.54 and 3.71 cm, respectively; see the inset in Fig. 4.12(a). The FSO channel loss was 5.5 dB. The laboratory C_n^2 was about $2.4 \cdot 10^{-14}$ m$^{-2/3}$. The ODN output was then transmitted to the BS via an OC-2, amplified by the EDFA-2 (Amonic, AEDFA-23-B-FA) for ODN loss compensation, and filtered by an optical bandpass filter (OBPF-1, Finisar WaveShaper 4000S) to reduce amplified spontaneous emission noise. Figure 4.12(c) also displays the optical spectrum measured after OBPF-1. The frequency spacing between two sidebands is 39 GHz and the measured optical carrier suppression to sideband ratio is 40 dB. A VOA was then used to reduce the received optical power (P_{r_o}) with respect to the maximum value of 6 dBm into the PIN PD (u2t BPDV2020R), where the beating of the two sidebands was held to generate the desired 39 GHz signal. The electrical signal then can be amplified by an mmW PA and radiated wirelessly over the RF link via a grid array of ANTs in real applications. In this work, due to the unavailability of ANTs at 39 GHz band, the signal was then electrically amplified by an IF PA-2 (WNA-180) having 40 dB gain and finally evaluated by a commercially available software (Scope,Tektronix DPO72004C).

For the UL direction, a distributed feedback laser (EXFO IQS-610) emitted the optical power of 12 dBm at λ of 1550.9 nm, whose optical spectrum is shown in Fig. 4.12(d). It was then connected to a single-drive MZM (MZM-2, Photline MX-LN-40) via a PC for optical modulation. The MZM-2 was biased at the quadrature point (i.e., 5.1 V) to generate a DSB signal. Its modulation operation was driven by a 37 GHz 5G NR signal with 64-QAM at Rb of 2.4 Gb/s, which is the NR frequency range 2-test model 3.1, generated by a vector signal generator (VSG, R&S SMW200A). The output was amplified by a PA-3 (SHF-810) having 29 dB gain. Note that the data signal was practically supposed to be transmitted to the MZM-2 after the UL RF transmission. The optical signal was then launched to the mutual ODN via ISO-2 and OC-2. After ODN, it was passed over the OC-1 and VOA, then amplified by EDFA-3 (Amonic, AEDFA-23-B-FA) and filtered out by OBPF-2 (Alnair Labs BVF-100), whose spectrum output featuring the DSB is also shown in Fig. 4.12(d). The optical signal was detected by the PD and finally captured and assessed by a signal and spectrum analyzer (R&S FSW43). To analyze the proposed HMPL, both DL and UL transmission performances are evaluated in terms of EVM, BER, constellation diagrams, P_{r_o}, and P_{r_RF} for each QAM signal. Note that the indoor laboratory link was limited by the available space serving as a proof of concept while the link can be scaled up for a real network, as shown further. Also, the system phase noise represents an important issue. However, the systems optically generating mmW signal do not deteriorate significantly phase noise unless long fiber, i.e., over 50 km, or laser with wide linewidth are used [68]. Moreover, the characterization of the phase noise for similar systems can be found in [69].
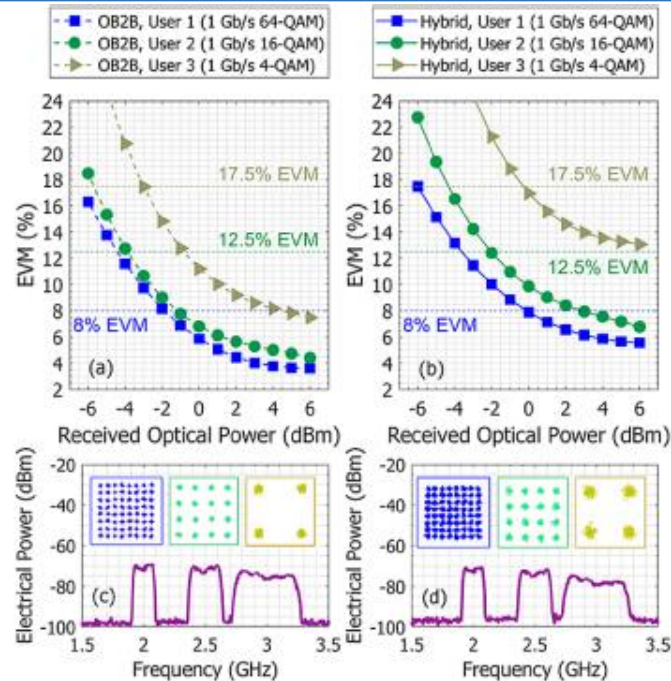
Fig. 4.13. Measured EVM versus received optical power for each band after (a) OB2B and (b) hybrid transmissions. (c) and (d) Corresponding received RF spectra and constellation diagrams (as insets) of OB2B and hybrid transmissions, respectively.

For three-band scenario (1 Gb/s each), the measured EVMs versus P_{r_o} of the SCM signals after OB2B and hybrid transmissions are shown in Fig. 4.13(a) and 7(b), respectively. As can be seen, all signals satisfy the EVM requirements for both configurations. For OB2B, the lowest EVMs for 4-, 16-, and 64-QAM are 7.5%, 4.5%, and 3.6%, respectively. The EVM performances are considerably less than the respective EVM requirements. The corresponding received RF spectrum and constellation diagrams are displayed in Fig. 4.13(c), which are clear and discernible.

Under the hybrid condition, at P_{r_o} of 6 dBm, the measured EVMs are 13.1%, 6.7%, and 5.5% for 4-, 16-, and 64-QAM, respectively, i.e., well satisfying the 3GPP specifications. The resultant EVM penalties between OB2B and hybrid transmissions are 5.6%, 2.2%, and 1.9% for 4-, 16-, and 64-QAM, respectively. This can be attributed to the CD [set to $17\ ps/(nm\ km)$] and FSO loss, which degrade the SNR as shown in the received RF spectrum in Fig. 4.13(d), where we noticed the spectrum profile is tilted, the noise floor is increased, and the received power is reduced gradually for bands at higher IFs. Still, the performance of the SCM signals is generally satisfactory, validating the effectiveness of using the variable QAM allocations scheme for delivering different multi-Gb/s signals over the hybrid link. Bearing in mind the availability of signal spectrum and selection of IF with narrower guard band—subject to the optimum QAM employed, more users can be accommodated based on the variable QAM allocations technique. In addition, we further observe two key points:

- By transmitting the SCM signals, the intermodulation effect is noticeable. For example, for OB2B, comparing the 1 Gb/s 16-QAM in SCM signals (4.5% EVM at P_{r_o} of 6 dBm) to that of single-band signal, whose EVM value is 5.0% but at R_b of 4 Gb/s; see Fig. 4.6(a). Nevertheless, the satisfactory performance of SCM signals over the hybrid link is also achieved.
- Although the EVM performances of 4-QAM in SCM signals for both OB2B and hybrid links are below the 17.5% EVM criterion, they are still high in comparison to that of

16- and 64-QAM. This is mainly because part of 4-QAM signal spectrum is out of the maximum frequency range of PA-1, the transfer response of which is non-flat and therefore significantly deteriorated signal beyond 3 GHz [see Figs. 4.13(c) and 4.13(d)]. Due to this issue, the outer symbols of 4-QAM constellations are randomly spread, which can be observed in the insets of Fig. 4.7(c) and 7(d), respectively, while 16- and 64-QAM constellations are visibly concentrated.

And finally, full duplex transmission schemes have been tested over fronthaul links incorporating remote mmW photonic local oscillator delivery for uplink down-conversion in DML-based optical hybrid C-RAN fronthaul [70].
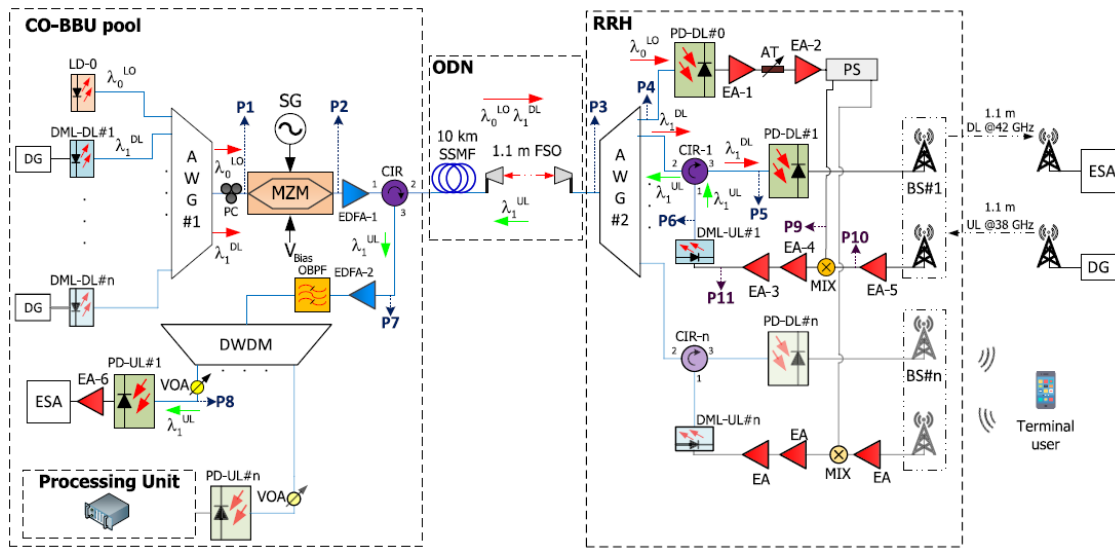

Fig. 4.14. Schematic of the experimental setup of full duplex RoF and RoFSO analog fronthaul transmission with LO delivery for UL downconversion by CS-MZM photonically generated mmW signal. The parts employed in the experimental testbed are rendered in solid color, whereas the parts indicating the system extension toward the real system are shown in faded color.

The proposed experimental setup of photonic up-conversion for mmW DL transmission and local oscillator (LO) delivery for UL down-conversion consists of a CO that hosts the baseband unit (BBU) pool, an ODN, and an RRH, as shown in Fig. 4.14. The proposed scheme allows us to share resources for a number of RRHs to provide an efficient system architecture. Therefore, at the considered CO, a continuous wave laser diode (LD-0, Yenista T100S-HP/CLU) is used with 11.4 dBm output power at 1546.4 nm wavelength (λ_0^{LO}) to deliver the LO signal at the RRH. Simultaneously, a DML (DMLDL# 1, Optical Zonu OZ516) with 7.4 dBm output power at 1553.7 nm (λ_1^{DL}) is modulated by a 100 MHz quadrature phase-shift keying (QPSK)/64-QAM 5G NR signal at 2 GHz IF, which is generated by the data generator (DG, Rohde & Schwarz SMW200A) using the predefined 5G NR test models, namely, TM 1.1 and TM 3.1 [71]. Low-order (QPSK, i.e., TM 1.1) and high-order (64-QAM, i.e., TM 3.1) modulation formats have been chosen for the sake of system validation within the experimental EVM range. Note that the bandwidth of the off-the-shelf DML-DL#1 is 7.7 GHz. The optical signals are then multiplexed by a 1_32 arrayed waveguide grating #1 (AWG#1, Alcatel 3CN00621JL) with a free spectrum range (FSR) of 100 GHz (0.8 nm). Therefore, a number of Txs, i.e., DMLs emitting at different wavelengths, can be deployed in the CO for multichannel downlink transmission, as indicated in Fig. 4.14, for up to DL#n. The polarization state of the input signal at the following MZM is aligned by a PC while electronic control of these components in the BBU pool is required to prevent any instability arising from polarization changes or thermal bias drift. Nevertheless, due to the limited resolution of the optical spectral analyzer (OSA),

only LD-0 and DML-DL#1 optical carriers can be distinguished, whereas the 2 GHz IF in DML-DL#1 is below the distinguishing ability of the OSA. The MZM (Sumitomo T.DEH1.5-40X-ADC-Y-Z), which is placed after the PC, is driven by an electrical single tone at 20 GHz generated by a signal generator (SG, Agilent 8267C) with 23 dBm of electrical output power. In order to achieve a CS optical signal, the MZM is biased at the null transmission point (V_π), i.e., by 7.36 V, which results in the CS ratio of 29 dB. The microwave photonics-based mmW signal generation approach, using the carrier-suppressed external modulator, is employed for the frequency up-conversion of the incoming optical signals, i.e., λ_0^{LO} and λ_1^{DL}, where the frequency of the electrical driving signal at the MZM is half the target frequency band f_{mmW}, thus $f_{RF} = f_{mmW}/2 = 20$ GHz. Only one DML Tx is used in the experimental setup, but the scheme can be used for multiple #n channels while the sharing of the MZM for signal up-conversion reduces costs and complexity.

Then, an erbium-doped fiber amplifier (EDFA, Amonics AEDFA-23-B-FA) with 14.15 dBm fixed output optical power is applied for compensating the MZM losses, and, after the amplification, the signal is launched into port 1 of a circulator (CIR, Acelink Technologies CIR-3-155-P-09-1-FC/PC) to be transmitted over the optical fronthaul link in the DL direction. The ODN consists of a 10 km long SSMF and a 1.1 m long FSO channel using a pair of air-spaced doublet collimators (Thorlabs F810APC-1550). The FSO fiber-to-fiber link loss is 8.2 dB, which is significantly lower compared to the mmW band free space transmission losses within the same distance. Note that an additional demultiplexing stage would be required at the output of the ODN for multiple RRH connectivity. The received optical signal at the RRH side is demultiplexed by a 1x40 AWG (AWG#2, Alcatel RB9020-00173) with the same FSR as the AWG#1, i.e., 100 GHz. Note that the spectrum at point P3 evinces a significantly increased noise floor due to the amplified spontaneous emission (ASE) noise introduced by the EDFA. Nevertheless, most of the noise is subsequently filtered by the AWG with the 0.8 nm grid. The beating of the first-order modulated sidebands at the PD (PD-DL#0, Finisar XPDV2320R-VF-VA) then generates the desired mmW LO single tone signal at 40 GHz, with 0 dBm of electrical power level, which is then adjusted by an amplification stage consisting of electrical amplifiers (EAs), i.e., EA-1 (SHF Communication Technologies AG SHF 810) and EA-2 (SHF Communication Technologies AG SHF 810) and an attenuator (AT). Although the phase noise of the generated mmW signal has not been measured in this experiment, a magnitude as low as -93 dBc/Hz in a similar setup with 100 kHz offset was reported in [53].

Furthermore, the optical data signal λ_1^{DL} is selected by the corresponding port of AWG#2 and transmitted via port 2 of CIR-1 to the Rx. It provides the up-conversion for DL data signal to 42 GHz after opto-electronic conversion at the PD-DL#1 (Finisar XPDV2320R-VF-VA). The DL signal must be subsequently amplified after the photodetection to be transferred to the seamless antenna transmission at the remote site. Note that the CS-MZM technique for mmW signal transmission shows high immunity to fiber-induced dispersion fading under ideal carrier suppression [72]. The UL at the RRH employs the same DG and DML for the signal generation and optical transmission as for the DL. The DG generates 100 MHz QPSK/64-QAM 5G NR data signals at 38 GHz with 2 dBm of electrical power, which is transmitted by a double ridged horn antenna (RFspin DRH40) through the 1.1 m wireless radio link with the wireless link loss of 26.8 dB. The received electrical signal is amplified by EA-5 (SHF-810) and combined with the photonically generated 40 GHz LO electrical signal using an RF mixer (MIX, MITEQ M2640W1). In the experimental setup, the input of the mixer is directly connected to the output of the EA-2, producing the LO; however, for scalability, a power splitter can be used to share the LO for other UL signals as indicated in Fig. 4.14.

The down-converted signal at the IF of 2 GHz is obtained by mixing the 38 GHz UL signal with the 40 GHz LO signal, which is further amplified by two cascaded electrical amplifiers, i.e., EA-3 (Minicircuits ZRL-2400 LN) and EA-4 (Minicircuits ZJL-4HG) to be launched into the DML-UL#1 for the electro-optical conversion. Note some additional nonlinearities and noise in the electrical spectrum of this signal arising from the afore-mentioned components. DML-UL#1, with similar characteristics to DML-DL#1, emits an optical carrier at 1553.5 nm. Then, the UL signal is transmitted through port 1 of the CIR-1 and then launched into the corresponding port of the AWG#2. Multiple UL signals can be included at the RRH due to the dense wavelength multiplexing (DWDM) grid in the AWG, as indicated in Fig. 4.14.

The optical signal (λ_1^{UL}) is launched into the full-duplex ODN via AWG#2, employing the same port as λ_1^{DL} in the reverse direction. EDFA-2 (Amonics AEDFA-23-B-FA) with fixed 13 dBm output power is used to compensate for the optical losses, whereas the part of the produced ASE noise is afterward filtered out by an optical bandpass filter (OBPF, Alnair Labs BVF-100-FS-SM) with bandwidth $\Delta\lambda$ equal to 0.8 nm, which exactly corresponds to the AWG grid used to filter out the ASE in the DL direction. Note that this EDFA and OBPF are only employed in the full link setup, OB2B and 10 km of SSMF do not require the optical amplifier. Note that another DWDM demultiplexer (e.g., another AWG), indicated in the CO in Fig. 4.14, would separate different UL optical channels in practical networks, and therefore any out-band signal would be removed (in that case, OBPF could be skipped). The optical power is adjusted by a VOA behind the OBPF, and finally the optical signal is launched into the low-frequency PD-UL#1 (JDS-Uniphase 64RA-2D12) and the recovered electrical UL signal is afterward analyzed by an ESA. The usage of low-frequency PD due to the UL down-converted IF transmission then considerably reduces requirements and costs for the network deployment also at the CO side. Note that Fig. 4.14 shows that multiple UL channels can possibly be demultiplexed by inserting a DWDM component.

Moreover, the schematic shows the EDFAs allocated in the CO with the associated cost and benefits in terms of sharing among several wavelengths, while the power requirements for the remote side are reduced in order to keep acceptable power consumption and low footprint.
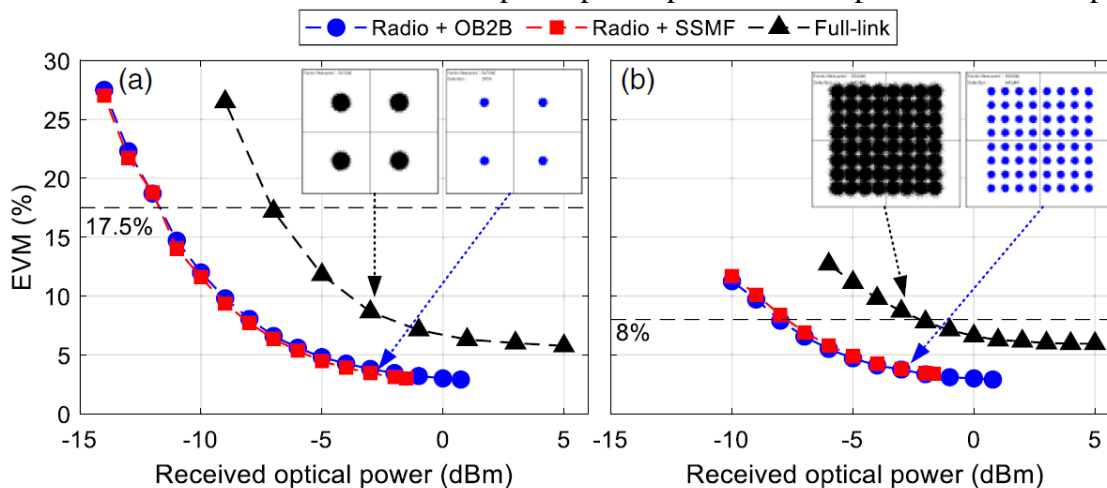

Fig. 4.15. Characterization of EVM performance versus RoP in the remote photonic LO delivery-assisted down-converted UL transmitting different 5G NR modulation formats: (a) QPSK, (b) 64-QAM. Insets show constellations obtained with RoP=-3 dBm for Radio + OB2B setup and full-link operation.

Based on these results, we have therefore adopted 2 dBm of the data UL power for both modulation formats for further testing (insets in Fig. 4.15 show the corresponding constellations

in the Radio+OB2B setup). In the next step, we have done the EVM characterization of the UL employing the photonic LO remote delivery by using both modulation formats: QPSK and 64-QAM with P_{data} D2 dBm at 2 GHz in terms of the received optical power (RoP). The results of the RoP, which was changed by the VOA, are shown in Fig. 4.15. Both measurements lead to very similar results for Radio+OB2B and Radio+SSMF setups except for the maximal achieved RoP, while the full-link operation, including the EDFA-2, leads to some signal penalty with the corresponding increased EVM.

The penalty is caused especially by use of the FSO channel with 8.2 dB loss, which is compensated by the EDFA resulting in higher maximal RoP for the full link, as can be seen in Fig. 4.15, but the received SNR is degraded (note that the noise figure of used EDFA-2 is up to 6 dB). On the other hand, the employment of the EDFA-2 enables the transmission of even the 64-QAM over the full-link UL configuration with very good performance, i.e., EVM considerably below the maximal limits. It can be observed that full-link operation with QPSK and 64-QAM requires the minimum RoP of -7.1 and -2.5 dBm, respectively. Insets show the obtained signal constellations for Radio+OB2Bs and full links with RoP= -3 dBm for both QPSK and 64-QAM signals, where the difference in EVM between them in both cases is 5%. Note that, for QPSK and 64-QAM mmW down-converted signals, the minimum EVM obtained under full link operation is 5.8% and 6%, respectively.

4.4. Analog Radio-over-LWIR FSO Distributed MIMO

The next generation of mobile networks is fast approaching. Global efforts have been made towards the future development of International Mobile Telecommunications for 2030 and beyond (IMT-2030), i.e., the upcoming sixth-generation mobile networks (6G) [73]. At present, fundamental and applied research have provided a comprehensive overview of the technological improvements expected in terrestrial IMT systems in the coming years, extending up to 2030 and beyond, including an analysis of key emerging services, trends in applications, and significant driving factors that will influence the evolution of IMT systems. This is reflected in the International Telecommunications Union Radiocommunication Sector (ITU-R) Report M.2516-0 [74]. Complementary to the scenarios described in IMT-2020 (5G), i.e., enhanced mobile broadband (eMBB), ultra-reliable low latency communications (URLLC), and massive machine type communications (mMTC) [75], some of the prospective services and possibilities for growth are holographic communication (delivery of 3D images), extremely high-rate access, connectivity for everything, extended reality (XR), multidimensional sensing, digital twin, global seamless coverage, among others. To fulfil the new requirements imposed by the preceding services and trends, some of the key factors that will drive the development and adoption of IMT systems beyond 2030 are energy efficiency, increased data rate, sensing resolution and accuracy, and spectral efficiency.

Among the key facilitators of 6G mobile networks, multiple-input multiple-output (MIMO) technology remains a significant factor. Presently, MIMO systems are not reaching their full potential when compared to theoretical channel capacity limits. Therefore, there is a pressing need for innovative approaches to address this disparity. Enhancing current MIMO technology involves various strategies such as deploying larger antenna arrays, improving hybrid beamforming, distributed deployments, integrating artificial intelligence (AI), and other solutions [74].

Distributed multiple-input multiple-output technology (D-MIMO) is a promising approach to meet these needs, providing increased capacity by distributing antennas over a cell [76]. Compared with traditional centralized MIMO, D-MIMO systems have better performance on spatial multiplexing gain, reducing interference and improving spectrum utilization. Additionally, since the antennas are more evenly distributed in the cell, the wireless distances for users are decreased, while the data rates and coverage are increased. D-MIMO supports a more reliable, fast and energy saving communication, especially for those in the cell-edge. While D-MIMO offers several advantages, it presents higher complexities requiring coherent joint transmissions (CJTs) and precise synchronization to maximize its gains. Analog radio-over-fiber (ARoF) and radio-over-mid-infrared (IR) free-space optics (FSO), specifically in the long-wave IR (LWIR) band [77-80], emerge as viable solutions to address large bandwidth signals and low complexity antenna units. ARoF and ARoFSO links offer a promising alternative where current digital fronthaul interfaces fall short. This is because the optical carriers that propagate through the transmission medium are modulated with analog RF signals, allowing for the estimation of amplitude and phase changes in the wireless channel and fronthaul links, and thus facilitating synchronization processes.

A. Demonstrator setup and results: NR conformance testing of analog radio-over-LWIR FSO fronthaul link
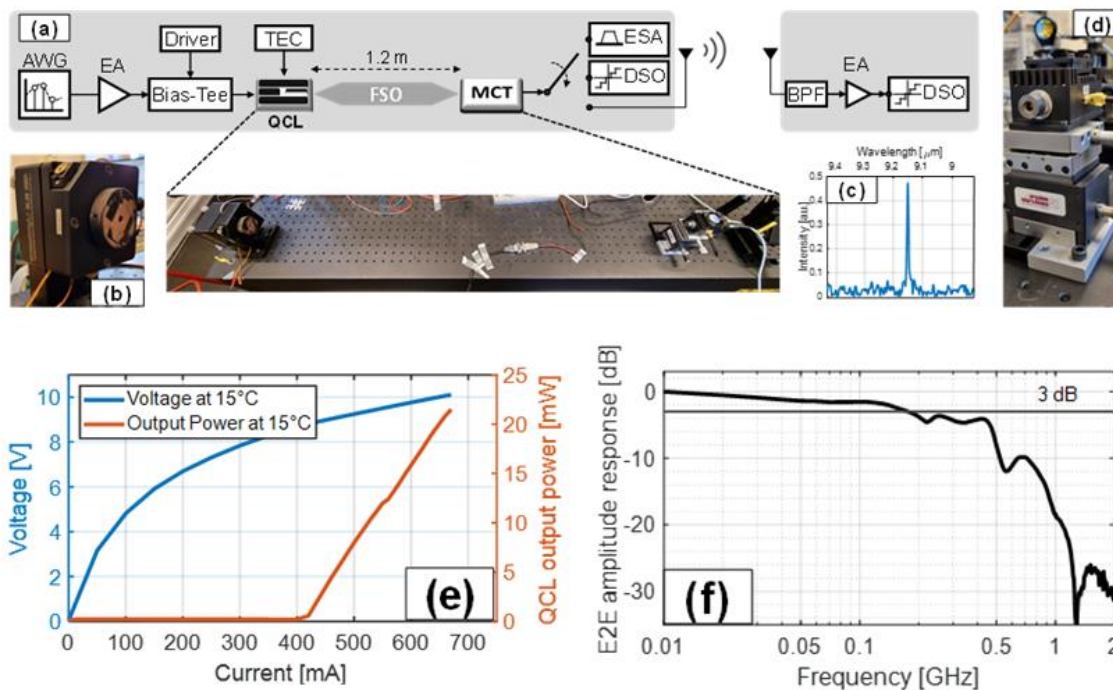

Fig. 4.16. (a) Experimental setup. (b) DM-QCL transmitter. (c) QCL output spectrum at room temperature. (d) MCT detector. (e) P-I-V curve of the 9.15-µm DM-QCL. (f) Characterized end-to-end amplitude response including the QCL, MTC detector, all the electrical and RF components.

Figure 4.16(a) shows the experimental configuration for NR conformance testing of analog radio-over-LWIR FSO fronthaul link. The experimental setup employs an NR signal with a bandwidth of 20 MHz with a SCS of 30 kHz, and carrier frequency of 627 MHz. This band was chosen due to the limited bandwidth of the MCT detector. The setup includes a 4 mm single mode DM-QCL laser mounted on an Aluminum-Nitride submount, operable at room temperature with a Peltier cooling module. The setup, including the photos of the LWIR Tx and Rx are shown in Figure 4.16. For the FSO transmission, a beam-collimating lens is used with a commercial MCT IR Photovoltaic detector, creating a wireless distance of 1.2 m between the
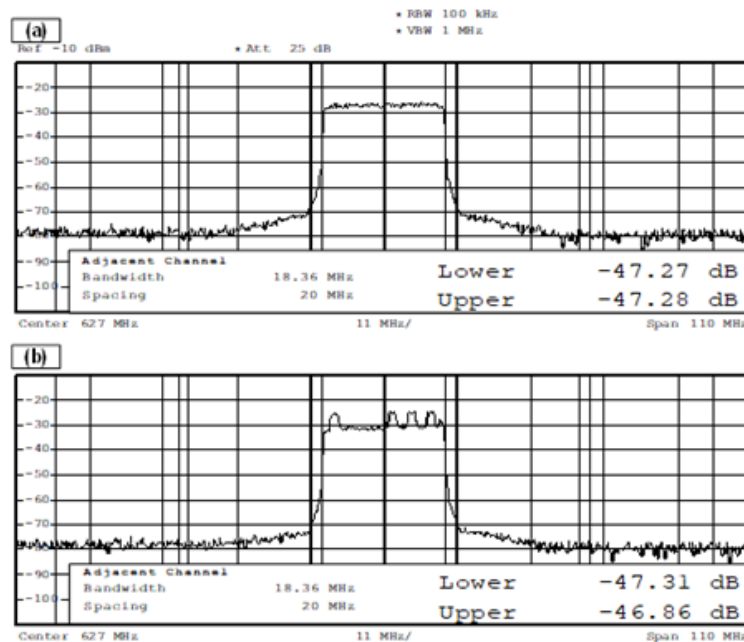

Fig. 4.17. Electrical spectrum and ACLR measurements of (a) TM NR-FR1-TM1.1 and (b) TM NR-FR1-TM1.2.
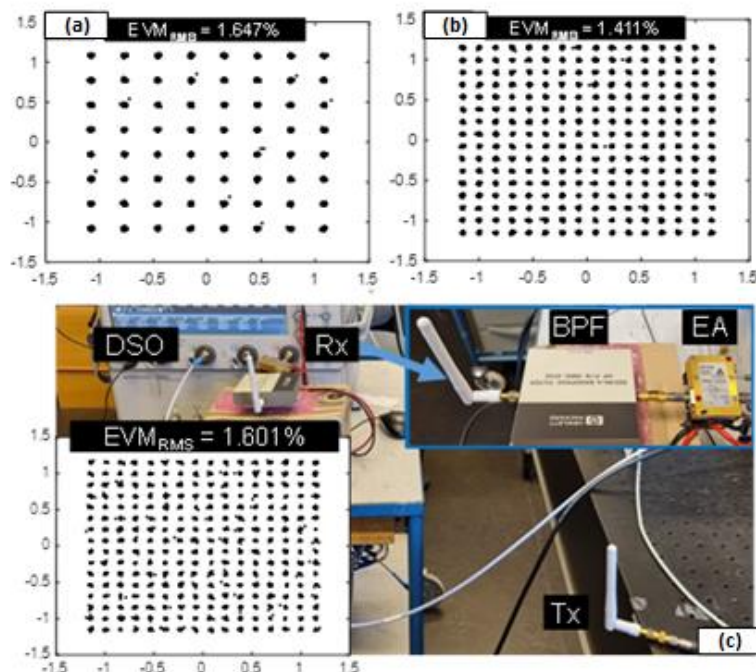

Fig. 4.18. Electrical spectrum and ACLR measurements of (a) TM NR-FR1-TM1.1 and (b) TM NR-FR1-TM1.2.
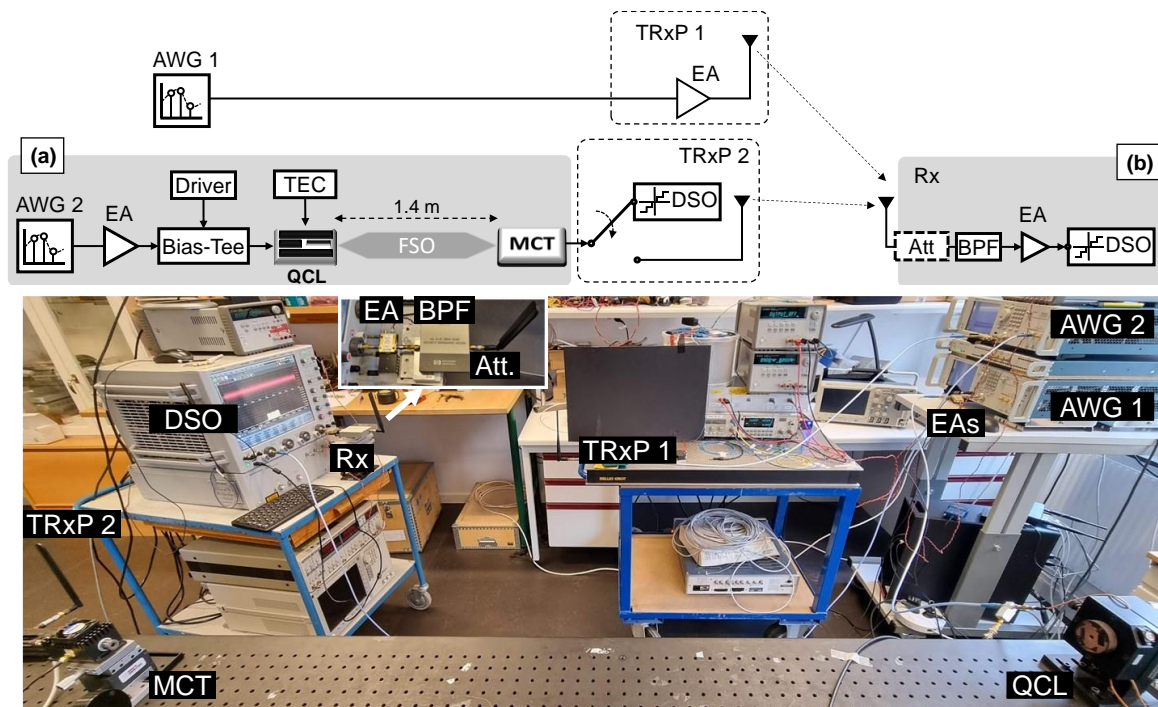
Fig. 4.19. (a) Experimental setup of 2 TRxPs D-MIMO CJT with analog radio-over-LWIR FSO fronthaul link. (b) the wireless Rx setup. (c) Photo of the experimental setup of 2 TRxPs D-MIMO CJT with analog radio-over-LWIR FSO fronthaul link.

DM-QCL and the detector. The MCT detector's 3-dB bandwidth is around 720 MHz. The FSO channel's frequency response is calibrated to optimize the received signal power. The ACLR of the RF signals are measured with an ESA, and subsequently captured for offline processing to calculate the EVM.

Figures 4.17(a) and 4.17(b) display the electrical spectrum and ACLR values of RF signals after photodetection and amplification, with ACLR values exceeding 44.2 dB, satisfying 3GPP requirements [81]. The bandwidth for calculating ACLR is 18.36 MHz, corresponding to the settings defined in [82]. To assess RF signal quality, test signals carrying 64-QAM and 256-QAM symbols were used. Figures 4.18(a) and 4.18(b) show EVM values which are within the required limits. To test the E2E performance, a multiband antenna is used to transmit the RF signals wirelessly. A narrow BPF and amplifier compensate for wireless losses. Figure 4.18(c) shows the Rx setup for the wireless transmission test and the received symbols constellation, demonstrating negligible EVM degradation compared to the conducted results in Figure 4.18(b).

B. Demonstrator setup and results: 2 TRxPs D-MIMO CJT with analog radio-over-LWIR FSO fronthaul link

We also implemented analog radio-over-LWIR FSO fronthaul links in the CJT by replacing the ARoF fronthaul link with the FSO link. As shown in the Fig. 4.19 (a), The D-MIMO network setup includes two TRxPs, a 1.2m coaxial cable for TRxP 1. The analog radio-over-LWIR FSO fronthaul link connects TRxP 2, where equipment setup is the same as the previous NR conformance testing of FSO fronthaul link, but the distance of free space increases to 1.4 m. Two AWGs of 50 GSa/s are used to generate analog signals. For wireless transmission, we apply multiband antennas with 3 dBi gain for both TRxPs. Figure 4.19 (b) shows the Rx setup, a BPF centered at 622 MHz filters the RF signals before it captured by a 10 GSa/s DSO. To adjust the
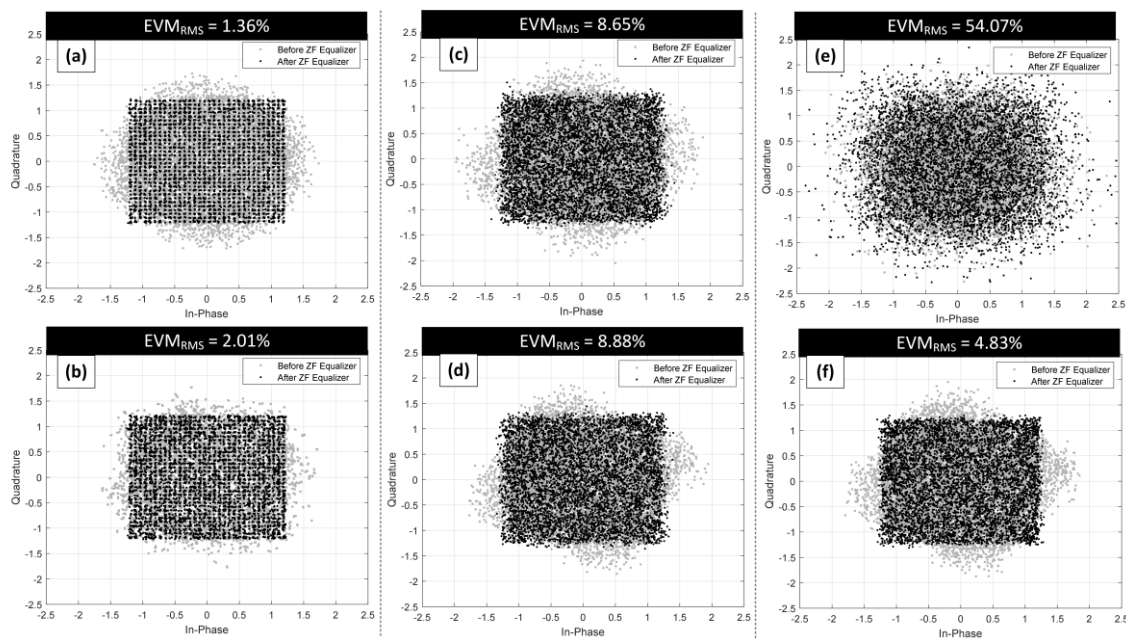
Fig. 4.20. Received symbols constellation and EVM measurement before and after ZF equalization for (a) optimally configured TRxP 2 before wireless transmission. (b) optimally configured TRxP 2 after wireless transmission. (c) attenuated TRxP 1 and (d) attenuated TRxP 2 after wireless transmission. (e) NCJT and (f) CJT when both TRxPs transmitting simultaneously.

received signal power, we applied an optional electrical attenuator before the BPF, therefore we can validate the CJT power and diversity gains. To generate AWGN channel, we also regulated the spacing of our setup to achieve nearly flat fading conditions for both received signals. In this experiment, an OFDM signals of 10 MHz with 30 kHz SCS, 24 RBs, and a 622 MHz carrier frequency was employed with non-TDD band. The OFDM signals from each TRxP are transmitted separately to approach channel estimation for both TRxPs. Therefore, both signals are time and phase aligned with each other.

We tested the end-to-end EVM performance of TRxP 2 with and without wireless transmission firstly, where all subcarriers carrying high-order 1024-QAM symbols during the test. By optimizing the operating parameters of experimental devices, which includes the AWG output signal voltage, DM-QCL bias current, and MCT detector received power, and through ZF equalization, we achieved the EVM RMS values of 1.36% before wireless transmission and 2.01% after wireless transmission, as shown in the Fig. 4.20 (a) and Fig. 4.20 (b) respectively. To evaluate the D-MIMO CJT performance, we intentionally degrade the performance of the TRxPs transmission through the electrical attenuator installed before the Rx's BPF. The received symbol constellations from TRxP 1 are demonstrated in Fig. 4.20 (c), where the EVM RMS is 8.65%. For the constellations received from TRxP 2 are demonstrated in Fig. 4.20 (d), where the EVM RMS is 8.88%. Both values are very close to each other. The channel estimation for TRxP 1 and TRxP 2 are conducted subsequently, their results are used to determine the precoding of signals from TRxP 2. Eventually, the precoded signal is time-aligned depending on the latency between TRxPs. Figure 4.20 (e) and (f) depict the received symbol constellation without and with precoding and time alignment respectively when simultaneous transmission implemented for both TRxPs. In non CJT (NCJT), although we have OFDM CP insertion, the EVM RMS degrades into 54.07% even with due to the insufficiency of coherency and inter-symbol interference (ISI). On the contrary, we achieved an EVM of 4.83% with CJT, since the signals are time and phase aligned, the power gain and network's diversity are greatly increased. Because of the similarity between TRxPs transmission channel conditions and flat fading, the

D-MIMO combined diversity and power gains is confirmed through the relationship between EVM and SNR [83], which is $EVM\_RMS^2 \approx 1/SNR$.

Comparing with transmission separately for each TRxPs, the CJT gain is approximately 5.29 dB for TRxP 2 and about 5.06 dB for TRxP 1. The theoretical value of CJT gain is 6 dB for a D-MIMO network with two TRxPs. The difference for the experimental result can be caused by several reasons, the EVM performance for both TRxPs is equalized intentionally although the wireless distances are mismatched, thus, the transmit power is unequal. Furthermore, both TRxPs have different antennas, and we do not approach a perfect flat-fading channel in the wireless transmissions.

4.5. Conclusions RoFSO

In this section experimental trials of hybrid FSO/SSMF networks using photonically generated mmW signal in the frequency range of $26-40$ GHz have been done with different turbulent distributions along the RoFSO link. Optical carrier suppression at MZM was used to generate double frequency signals, i.e., the measured RF power at 26 GHz was -39.97 dBm. Moreover, 8 Gb/s 16-QAM data signal transmission at 42 GHz was demonstrated over hybrid links with an EVM as low as 5% providing enough capacity for considered transmission within 5G networks. Several turbulence distributions along the FSO link were implemented and their impact on the signal transmission was evaluated. We experimentally verified that the highest impact on RoFSO link transmission can be expected under turbulence evenly distributed along the link. The measured turbulence scenarios resulted in up to 5 dB power penalty in terms of received optical power for EVM level of 12.5% in comparison with the performance of the hybrid link without turbulence.

Moreover, transmission experiments of 20 MHz 4- and 64-QAM signals over 5 km of SSMF and a 2 m long FSO link confirm that turbulence distributions with higher strength in the middle of the considered link have a bigger impact in terms of power penalty on 64-QAM (1.9 dB penalty) compared to 4-QAM (1.3 dB penalty). For 4-QAM, higher EVM results have been measured for distributions with larger turbulence magnitude in the second half of the link. In spite of different bitrates and FSO link length, results agree on a 4% EVM difference between 4- and 64-QAM at a given received optical power, i.e., 0 dBm, when comparing equivalent links with uniform weak turbulence. Thus, the presented system needs careful attention when the FSO link is exposed to turbulences with high gradients along the optical path, e.g., in dense urban areas.

We also investigated a hybrid 25 GHz RoF and RoFSO downlink in a PON architecture using the MZM-based optical up-conversion technique and 4/16/64-QAM for ubiquitous BWA connectivity in urban and rural areas under a non-uniform turbulent FSO link for M-QAM and showed EVMs of 13, 9.2 and 7.3% with clear constellation diagrams, thus demonstrating the use of the proposed scheme for practical applications. Experimental trials have been also conducted in this section towards the comparison of two setups using a conventional DSB analog MPL approach with an externally modulated laser and a CS-DSB scheme to double the input carrier frequency, respectively, considering the SNR and AT. We evinced no significant difference in the performance at 27 and 39 GHz thus making it as an attractive solution for

higher frequency bands. Moreover, the CS-DSB scheme can be implemented with frequency n-multiplication to further relax the bandwidth requirements. Contrary, although the conventional DSB analog MPL approach is highly sensitive to dispersion-induced fading and requires higher bandwidth, it offers improved EVM performance since MZM is biased at the quadrature point instead of the null point as in CS-DSB, higher SNR, lower phase noise, and reduced complexity.

Finally, the section also includes experimental trials on bidirectional networks. An experimental demonstration of an LTE M-QAM signal transmission over the 60 and 25 GHz bands for the DL and UL, respectively, is presented over an optical heterogeneous fronthaul network consisting of 10 km of optical fiber, a 100 m FSO link and a 2 m seamless radio link. The EVM measurements for both link directions under different configurations in terms of the RoP, fully validate the network performance and also allow to identify their differences. Results show different power budgets and penalties mainly due to the different structure of DL and UL, where the latter implements electro-optical conversion after amplification of the radio link output signal. In order to fulfil the 9% EVM limit for the 64-QAM signals with 20 MHz bandwidth, the minimum received optical power has been determined as -2.7 dBm and -1 dBm in the DL and UL, respectively, for the full-link configuration. It was shown that the advantageous use of the low-frequency DML for the DL and high-frequency DML for the UL to maximize the system performance and simultaneously reduce the complexity. Finally, it has been experimentally demonstrated that the 100 m long FSO channel can be effectively used as the "last mile" access in bidirectional optical fronthaul networks operating at mmW bands to provide better flexibility in the network densification and paves the way to the deployment of future hybrid optical and mobile communication networks operating in the mmW band.

Moreover, a hybrid full-duplex microwave photonic link has been proposed and demonstrated for mmW 5G RAN to support the Industry 4.0 connectivity requirements in a cost-effective (e.g., DML deployment and mutual ODN between DL and UL) and flexible (e.g., OFM module) manner. The achieved EVMs for all DL and UL signals are well below the required limits defined by the 3GPP standards. The presented results confirm the potential use of the proposed three-stage system to provide high-speed broadband services in suburban areas, where most manufacturing plants and factories are typically located. Finally, we have proposed and demonstrated the remote delivery of a photonically generated LO signal for uplink down-conversion in the 5G C-RAN system using photonically generated mmW signals over optical fiber and FSO. A single intensity modulated MZM in the CS regime, enabling the use of only half the target mmW frequency at the MZM input, was employed in the CO to generate a mmW signal at 40 GHz, distributed over a hybrid optical fronthaul network composed of SSMF and FSO. At the RRH side, the photonically generated 40 GHz signal was used for both the DL up-conversion/transmission toward the user and the UL down-conversion of the wireless mmW signal coming from a user, which considerably reduces the RRH complexity of operation and corresponding costs for the duplex analog mmW fronthaul network equipment. In order to validate our proposed concept, 5G NR QPSK and 64-QAM signals with 100 MHz bandwidth were successfully transmitted using low-cost, i.e., low-frequency, DMLs in both the DL and UL directions. The minimal achieved EVM value for the full link in the UL transmission was 5.8% and 6% for 5G NR QPSK and 64-QAM/100 MHz, respectively. Based on the experimental measurements, estimations of the minimum RoP required for proper UL signal recovery using both modulation formats can be obtained. Therefore, the concept of duplex mmW transmission for 5G C-RAN, with reduced cost and complexity for UL simple IFoF and FSO is presented.

Finally, the LWIR has been demonstrated as a viable solution to address large bandwidth signals with low complexity antenna units. In this work, two setups were employed: the first one, that employed a DM-QCL laser modulated by 64 and 256-QAM symbols, provided the NR conformance testing of analog radio-over-LWIR FSO fronthaul link according to 3GPP requirements. The second one employed coherent transmission approach under a 2 TRxPs D-MIMO CJT scheme where, in spite of the critical time and phase signal alignment, the power gain and network diversity were greatly increased.

5. Optical Camera Communications for mid ranges
5.1. A 400 m Rolling-shutter-based OCC link

Optical camera communication (OCC) offers multiple functionalities of vision, data communications and localization, which can be used in a number of applications including all-optical Internet of things (OIoT) [84, 85]. OIoT-based applications include device-to-device communications, mobile atto cells, vehicle-to-everything (V2X), smart environments, etc. [86], which releases the needed radio frequency spectrum for use in areas most required. Inspired by IoT, the internet of vehicles (IoV) is currently of high interest within the research community [85]. OCC can be deployed in intelligent transportation systems (ITS) for vehicle to vehicle, infrastructure-to-vehicle and vehicle-to infrastructure (V2I) communications, therefore a long link-span helps to establish a robust system [86, 87]. In [88], global-shutter (GS)-based OCC with a data rate of 15 bps over a link range of 328 m was reported for use in smart city applications with ~4% wrongly decoded received bit streams. In [89], a rolling shutter (RS)-based OCC link for outdoor application with a maximum link span of 120 m, a bit error rate of $> 10^{-2}$ (at 120 m), and an achieved maximum data rate of 200 bps at a 4 m link span was reported.

In this work, we propose a novel reception technique in order to increase the transmission link-span of RS-based OCC by reducing camera's spatial bandwidth in the out-of-focus areas. This helps to have a larger footprint of the light source on the image sensor without reducing the field of view (FoV). We also develop a detection algorithm to effectively extract the received information from captured video frames. We have used a light source (i.e., 2.5×2.5 cm^2), which is 19 times smaller than the source that was adopted in [88]. The proposed system is attractive in distance critical applications requiring relatively low data rate as in ITS (e.g., exchange of safety and traffic messages and positioning-related information) for smart traffic management. In this work, we achieve a communication link of up to 400 m with 100% success rate in data transmission achieving a data rate of 450 bps. The demonstrated system, to the best of our knowledge, is the longest link-span achieved for a RS-based OCC link.
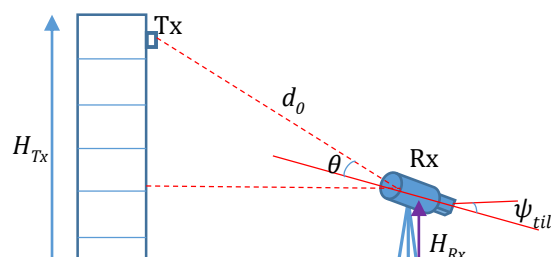

Fig. 5.1. Configuration of the long-distance OCC link 000 [34].

Fig. 5.2. Experimental setup [34].

The system configuration and experimental setup for the long-distance OCC are shown in Figs. 5.1 and 5.2. The Tx was located on the 6th floor (height of 25m) and Rxs was placed outdoor at a height of 1.40m above the ground. At the start of the measurement campaign, the weather was partly cloudy/sunny while by the end it was sunny, with a temperature range of 23-25°C and the wind speed and humidity of 2-6 mph and 51-65%, respectively. The key experimental parameters include the light emitting diode (LED) drive current, FoV and mare 0.33A, 122° and 0.96, respectively. The Tx data packet is 18 bits, the Rx's frame rate is set to 25 fps for all experimental configurations considered and the number of received data bits is ∼32 per frame. The Rx's video resolution, pixel size, lens aperture and focal length are 648×484 (RGB 32), 2.2×2.2μm2, f/10 and 1000 mm, respectively. Measurements were carried out for a range of link spans and exposure time T_{exp} of 150 to 400m and 100 to 800μs, respectively. Image frames of the transmitted data were captured with up to 100% success rate of received bits for all links considered in this work.

Figure 5.3 shows the peak signal-to-noise (PSNR) versus link span for a range of T_{exp}. As illustrated, PSNR improves with T_{exp} and decreases with the increasing link span e.g., for T_{exp} of 800μs, PSNR drops by 2.1dB when increasing link span from 200 to 400m. The maximum values of PSNR are 3.3 and 0.2dB for T_{exp} of 800μs and 100μs at link span of 150m.
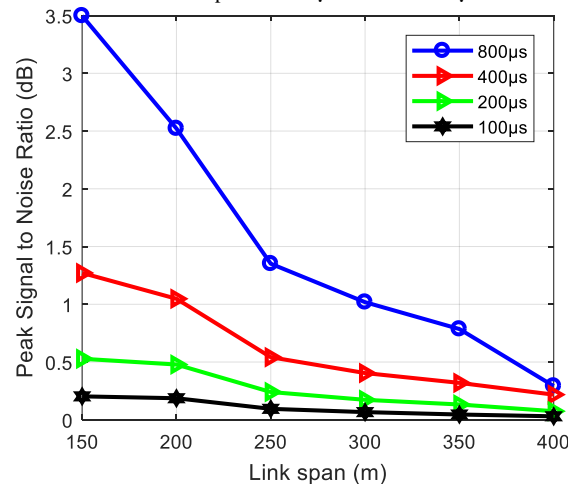

Fig. 5.3. PSNR versus link span for various exposure times [34].

Atmospheric turbulence, and oceanic turbulence in the case of underwater wireless optical communication (UWOC), has been extensively studied. Guo et al. introduced the traditional lognormal model into a simulated VLC link for ITS [91]. The authors proved that VLC wavelengths in ITS performed worse than longer ones (e.g., 1550 nm), which is straightforward, taking into account that the turbulence measured by Rytov's variance has a dependence on the wavelength. In the case of UWOC, in which the use of visible-range wavelengths is mandatory due to the water absorption spectrum, Kolmogorov's turbulence spectrum is substituted by Nikishov's [92]. This turbulence spectrum fits better with the experimental measurements since it takes into account not only temperature but salinity variations. Although the impact of turbulence has been characterized for classical optical detectors, its effect on OCC systems has not been adequately addressed yet. Works addressing channel characterization in outdoor OCC links [93] are still scarce compared to the amount of research on PD-based VLC. In the previous work [94], we evaluated the feasibility of a global shutter-based OCC link under fog conditions by the success rate of bits of vehicular link experimentally tested with a red brake light and a digital reflex camera. For a modulation index of 75%, the system showed high reliability under dense fog conditions up to a meteorological visibility of 20 m.

The contribution of this work is to experimentally derive the feasibility of OCC in emulated outdoor conditions of fog and heat-induced turbulence using commercially available LEDs and cameras. This work is the first to report an experimental investigation on the effects of such conditions on an RS-based system. The experiments carried out for this work were done using a laboratory chamber, and the conditions emulated were of heat-induced turbulence and the presence of fog in the air. The refractive index structure parameter (C_n^2) [95] is used to estimate the level of turbulence and the meteorological visibility (V_{M}) as a measure of the level of fog. The fog experiments are especially relevant because we utilize the camera's built-in amplifier to overcome the fog attenuation and mitigate the relative contribution of the quantization noise induced by the analog-to-digital conversion stage, ensuring an improvement of the signal quality without increasing the exposure time, and, thus, keeping a high bandwidth.

Figure 5.4 shows the experiment setup including the laboratory chamber used, the tools used for emulating hot and foggy weather conditions, the measurement devices used for estimating the levels of each condition, and the Tx and the Rx devices that comprise the OCC link. The block diagram of the experimental setup is shown in Fig. 5.5.
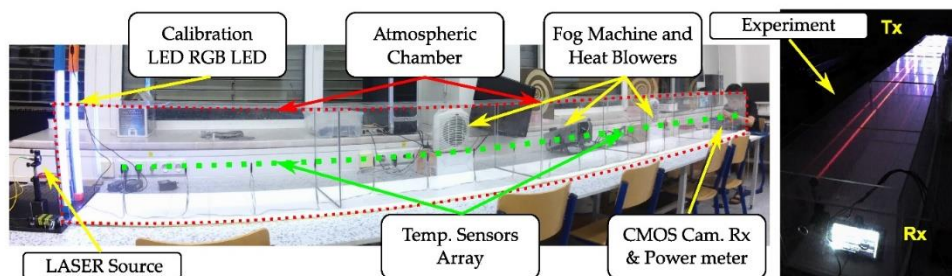

Fig. 5.4. Photos of the laboratory setup utilized in the experiments [90].
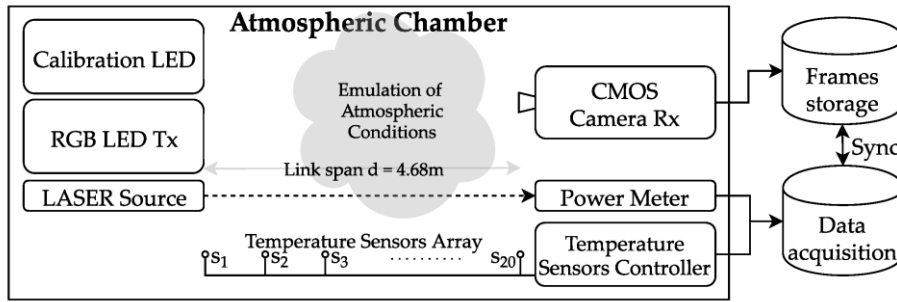
Fig. 5.5. Block diagram of the experimental setup [90].

The Pearson's maximum correlation coefficient r_{max}^{xy} values obtained for the test images sequence varying G_V and V_M are shown as a contour plot in Fig. 5.6. The high correlation area (r_{max}^{xy}>0.9) determines three important regions (highlighted in Fig. 5.6 by dashed circles). For the high values of visibility, the signal coming from the Tx is not affected by the fog attenuation and is received with the highest power. Then, the increase of gain causes saturation of the ADC, affecting the correlation. In the low visibility region, the presence of dense fog attenuates the received signal and lowers the correlation. It can be seen that, in this low-visibility region, the increase of gain gives a high correlation, meaning that the camera amplifier compensates the attenuation from fog. The region in between, around 50 m visibility, shows high values of correlation regardless of the variations of gain.
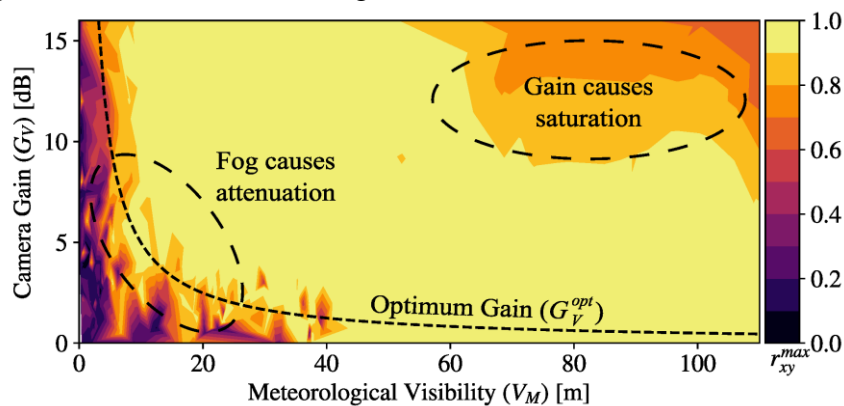

Fig. 5.6. Maximum correlation between test and reference signals varying camera gain under emulated fog conditions of different values of meteorological visibility [90].

The results obtained in this experiment show that the fog attenuation can make the power of the optical signal weaken down to the point that the noise induced by the ADC considerably affects the SNR. In other words, the conversion to digital corrupts the weak optical signal from dense fog conditions or long link spans. In these cases, the column amplifier of the camera is crucial to keep a high amplitude input at the ADC and reduce the effect of quantization.

A novel technique to increase the link span of RS-based OCC by reducing the spatial bandwidth of the camera in the out-of-focus regions was proposed and evaluated in [34]. The experimental analysis of the proposed scheme demonstrates a 100% success rate of received bits for a link span of up to 400 m using a small surface area Tx of 2.5×2.5 cm^2. The choice of the camera exposure time played a key role in determining the value of PSNR.

Furthermore, we presented an experimental study of the influence of two kinds of atmospheric conditions over an RS-based OCC link: the heat-induced turbulence due to random fluctuations of the refractive index of the air along the path, and the attenuation caused by the presence of fog particles in the air [90]. The image sequences captured under the two different conditions were compared to a reference sequence of images taken under clear conditions. For this, we used the maximum value of Pearson's correlation coefficient r_{xy}^{max} to determine their similarity. We have also evaluated the signal quality by the empirical SNR obtained from the image frames and showed its relationship with r_{xy}^{max} and its dependence on the product between fog attenuation and link span, known as the optical density. The most important findings in this work are, first, that the turbulence levels emulated do not affect the signal quality considerably. For the fog experiments, we have derived an expression for the theoretical SNR as a function of the analog camera gain, showing that a CMOS camera-based OCC system can improve the SNR by using the column amplifier. In the fog experiments, the correlation r_{xy}^{max} was impaired in two different cases: for high values of V_M, when the gain is increased, the correlation drops because of the saturation of the signal, and, for low visibility, the attenuation caused by the fog impairs the similarity to the reference when the gain is low, because of the loss due to quantization noise at the ADC. It was found for the latter case that by increasing the gain of the camera, the attenuation can be compensated, allowing the OCC link to receive signal with a $r_{xy}^{max} > 0.9$ for V_M values down to 10 m. Our findings show that there is an inverse proportionality relationship between the optimum camera gain and the visibility, and that the empirical SNR decays at a rate a with the optical density. This utilization of the CMOS camera's built-in amplifier opens a new possibility for OCC systems, extending the control strategy, and allowing to keep low exposure times and, thus, a high bandwidth, even in dense fog scenarios.

4. References

[1] R. Blasco-Serrano, R. Thobaben, V. Rathi, and M. Skoglund, "Polar codes for compress-and-forward in binary relay channels," in 2010 Conference Record of the Forty Fourth Asilomar Conference on Signals, Systems and Computers, 2010: IEEE, pp. 1743-1747.

[2] P. Jouguet and S. Kunz-Jacques, "High performance error correction for quantum key distribution using polar codes," arXiv preprint arXiv:1204.5882, 2012.

[3] J. Fang et al., "Performance investigation of the polar coded FSO communication system over turbulence channel," Applied Optics, vol. 57, no. 25, pp. 7378-7384, 2018.

[4] J. Fang et al., "Neural network decoder of polar codes with tanh-based modified LLR over FSO turbulence channel," Opt. Express, vol. 28, no. 2, pp. 1679-1689, 2020.

[5] J. Fang et al., "Polar-coded MIMO FSO communication system over gamma-gamma turbulence channel with spatially correlated fading," Journal of Optical Communications and Networking, vol. 10, no. 11, pp. 915-923, 2018.

[6] I. Tal and A. Vardy, "How to construct polar codes," IEEE Transactions on Information Theory, vol. 59, no. 10, pp. 6562-6582, 2013.

[7] J. Lin and Z. Yan, "An efficient list decoder architecture for polar codes," IEEE Transactions on Very Large Scale Integration (VLSI) Systems, vol. 23, no. 11, pp. 2508-2518, 2015.

[8] Z. Ghassemlooy, W. Popoola, and S. Rajbhandari, Optical wireless communications: system and channel modelling with Matlab®. CRC press, 2019.

[9] N. Mohan, M. M. Abadi, Z. Ghassemlooy, S. Zvanovec, R. Hudson, and M. R. Bhatnagar, "Sectorised base stations for FSO ground-to-train communications," IET Optoelectronics, vol. 14, no. 5, pp. 312-318, 2020.

[10] P. Kaur, V. K. Jain, and S. Kar, "Performance of free space optical links in presence of turbulence, pointing errors and adverse weather conditions," Optical and Quantum Electronics, vol. 48, no. 1, p. 65, 2016.

[11] I. Tal and A. Vardy, "List decoding of polar codes," IEEE Transactions on Information Theory, vol. 61, no. 5, pp. 2213-2226, 2015.

[12] W. Song et al., "Influence of fog on the signal to interference plus noise ratio of the imaging laser radar using a 16-element APD array," Optics Express, Vol. 26, Issue 17, pp. 22030-22045, vol. 26, no. 17, pp. 22030–22045, Aug. 2018, doi: 10.1364/OE.26.022030.

[13] M. Komanec, W. O. Popoola, Z. Ghassemlooy, S. Zvanovec, J. Libich, and P. Pesek, "Experimental verification of an all-optical dual-hop 10 Gbit/s free-space optics link under turbulence regimes," Optics Letters, Vol. 40, Issue 3, pp. 391-394, vol. 40, no. 3, pp. 391–394, Feb. 2015, doi: 10.1364/OL.40.000391.

[14] M. Singh and J. Malhotra, "Performance comparison of M-QAM and DQPSK modulation schemes in a 2 × 20 Gbit/s–40 GHz hybrid MDM–OFDM-based radio over FSO transmission system," Photonic Network Communications, vol. 38, no. 3, pp. 378–389, Dec. 2019, doi: 10.1007/S11107-019-00861-Z/METRICS.

[15] K. Anbarasi, C. Hemanth, and R. G. Sangeetha, "Block error rate performance analysis of RS coded M-QAM modulated coherent OFDM-FSO system," Opt Quantum Electron, vol. 55, no. 1, pp. 1–15, Jan. 2023, doi: 10.1007/S11082-022-04328-W/METRICS.

[16] W. O. Popoola and Z. Ghassemlooy, "BPSK Subcarrier Intensity Modulated Free-Space Optical Communications in Atmospheric Turbulence," Journal of Lightwave Technology, Vol. 27, Issue 8, pp. 967-973, vol. 27, no. 8, pp. 967–973, Apr. 2009, Accessed: Jan. 29, 2023. [Online]. Available: https://opg.optica.org/abstract.cfm?uri=jlt-27-8-967

[17] M. Capelle, M. J. Huguet, N. Jozefowiez, and X. Olive, "Optimizing ground station networks for free space optical communications: Maximizing the data transfer," Networks, vol. 73, no. 2, pp. 234–253, Mar. 2019, doi: 10.1002/NET.21859.

[18] Z. Htay, Z. Ghassemlooy, M. M. Abadi, A. Burton, N. Mohan, and S. Zvanovec, "Performance Analysis and Software-Defined Implementation of Real-Time MIMO FSO with Adaptive Switching in GNU Radio Platform," IEEE Access, vol. 9, pp. 92168–92177, 2021, doi: 10.1109/ACCESS.2021.3092968.

[19] J. Chen, J. Shi, J. Hu, C. Shen, and N. Chi, "DC-balanced even-dimensional CAP modulation for visible light communication," Journal of Lightwave Technology, vol. 40, no. 15, pp. 5041–5051, 2022.

[20] P. A. Haigh, P. Chvojka, S. Zvánovec, Z. Ghassemlooy, and I. Darwazeh, "Analysis of Nyquist Pulse Shapes for Carrierless Amplitude and Phase Modulation in Visible Light Communications," Journal of Lightwave Technology, vol. 36, no. 20, pp. 5023–5029, Oct. 2018, doi: 10.1109/JLT.2018.2869022.

[21] A. M. Shah et al., "Characterization of RF signal transmission using FSO links considering atmospheric effects," in Free-Space Laser Communication Technologies XX, 2008, pp. 112–121.

[22] C. Ben Naila, A. Bekkali, K. Wakamori, and M. Matsumoto, "Performance analysis of CDMA-based wireless services transmission over a turbulent RF-on-FSO channel," Journal of Optical Communications and Networking, vol. 3, no. 5, pp. 475–486, 2011.

[23] P. T. Dat et al., "Studies on characterizing the transmission of RF signals over a turbulent FSO link," Opt Express, vol. 17, no. 10, pp. 7731–7743, 2009.

[24] T. Wang, S. Bin Ali Reza, F. Buldt, P. Bassène, and M. N'Gom, "Structured light signal transmission through clouds," J Appl Phys, vol. 133, no. 4, 2023.

[25] N. Cvijetic, D. Qian, J. Yu, Y.-K. Huang, and T. Wang, "Polarization-multiplexed optical wireless transmission with coherent detection," Journal of Lightwave Technology, vol. 28, no. 8, pp. 1218–1227, 2010.

[26] D. S. Kim, "Hybrid Free-Space and Radio Frequency Switching," 2008.

[27] I. I. Kim, B. McArthur, and E. J. Korevaar, "Comparison of laser beam propagation at 785 nm and 1550 nm in fog and haze for optical wireless communications," *https://doi.org/10.1117/12.417512*, vol. 4214, pp. 26–37, Feb. 2001, doi: 10.1117/12.417512.

[28] M. Safari and M. Uysal, "Relay-assisted free-space optical communication," IEEE Trans. Wireless Commun., vol. 7, no. 12, pp. 5441–5449, Dec. 2008.

[29] O. Narmanlioglu, B. Turan, S. C. Ergen, M. Uysal, Cooperative MIMO-OFDM based inter-vehicular visible light communication using brake lights, Computer Communications, Volume 120, 2018, Pages 138-146.

[30] Z. Wu, Free space optical networking with visible light: A multi-hop multi-access solution. Boston University, 2012.

[31] C. B. Liu, B. Sadeghi, and E. W. Knightly, "Enabling vehicular visible light communication (V2LC) networks," in Proc. 8th ACM int. Workshop on Vehicular Inter-Netw. ACM, 2011, pp. 41–50.

[32] E. Eso, P. Pesek, P. Chvokja, Z. Ghassemlooy, S. Zvanovec and J. Sathian. 'A Relay-Assisted Vehicular Visible Light Communications Network'. IEEE Photonics Conference, 2020.

[33] E. Eso, Z. Ghassemlooy, S. Zvanovec, J. Sathian and A. Gholami, "Fundamental Analysis of Vehicular Light Communications and the Mitigation of Sunlight Noise," in IEEE Trans. on Veh. Tech., 2021.

[34] E. Eso, S. Teli, N. B. Hassan, S. Vitek, Z. Ghassemlooy and S. Zvanovec, "400 m Rolling Shutter based Optical Camera Communications Link. Optics Letters, 2020.

[35] ITU-R, "Report ITU-R M.2370-0; IMT traffic estimates for the years 2020 to 2030", 2015 Available: https://www.itu.int/dms_pub/itu-r/opb/rep/R-REP-M.2370-2015-PDF-E.pdf

[36] W. Jiang, B. Han, M. A. Habibi and H. D. Schotten, "The Road Towards 6G: A Comprehensive Survey," IEEE Open J. Commun. Soc. 2, 334-366, 2021.

[37] H. Tataria, M. Shafi, M. Dohler and S. Sun, "Six Critical Challenges for 6G Wireless Systems: A Summary and Some Solutions," in *IEEE Vehicular Technology Magazine*, vol. 17, no. 1, pp. 16-26, March 2022, doi: 10.1109/MVT.2021.3136506.

[38] J. Beas, G. Castanon, I. Aldaya, A. Aragon-Zavala and G. Campuzano, "Millimeter-Wave Frequency Radio over Fiber Systems: A Survey," in IEEE Commun. Surv. Tutor., vol. 15, no. 4, pp. 1593-1619, 4Q 2013.

[39] M.A. Khalighi, M. Uysal, Survey on free space optical communication: a communication theory perspective, IEEE Commun. Surv. Tutor. 16 (4) (2014) 2231–2258.

[40] J. Bohata, M. Komanec, J. Spácil, Z. Ghassemlooy, S. Zvánovec, and R. Slavík, "24-26 GHz radio over fiber and free space optics for 5G systems," Opt. Lett., vol. 43, no. 5, pp. 1035–1038, Mar. 2018.

[41] J. Bohata, S. Zvanovec, P. Pesek, T. Korinek, M. Mansour Abadi, and Z. Ghassemlooy, "Experimental verification of long-term evolution radio transmissions over dual-polarization combined fiber and free-space optics optical infrastructures," Appl. Opt., vol. 55, no. 8, pp. 2109–2116, Mar. 2016.

[42] H.H. Refai, J.J. Sluss Jr., H.H. Refai, Comparative study of the performance of analog fiber optic links versus free-space optical links, Optim. Eng. 45 (2) (2006) 025003

[43] D. K. Borah and D. G. Voelz, "Pointing error effects on free-space optical communication links in the presence of atmospheric turbulence," J. Lightw. Technol. 27, 3965–3973 (2009).

[44] M. A. Esmail, A. Ragheb, H. Fathallah, and M.-S. Alouini, "Investigation and demonstration of high speed full-optical hybrid FSO/fiber communication system under light sandstorm condition," IEEE Photon. J. 9, 1–12 (2017).

[45] J. Libich and S. Zvanovec, "Influences of turbulences in near vicinity of buildings on free-space optical links," IET Microw. Antennas Propag., vol. 5, no. 9, pp. 1039–1044, 2011.

[46] K. Niachou, I. Livada, and M. Santamouris, "Experimental study of temperature and airflow distribution inside an urban street canyon during hot summer weather conditions—Part I: Air and surface temperatures," Build. Environ., vol. 43, no. 8, pp. 1383–1392, Aug. 2008.

[47] P.T. Dat, et al., Studies on characterizing the transmission of RF signals over a turbulent FSO link, Opt. Express 17 (10) (2009) 7731.

[48] S. Bloom, E. Korevaar, J. Schuster, and H. Willebrand, "Understanding the performance of free-space optics [Invited]," J. Opt. Netw. 2, 178–200 (2003).

[49] H. R. Anderson, Fixed Broadband Wireless System Design, 1st ed. (Wiley, 2003).

[50] D.-N. Nguyen, J. Bohata, J. Spacil, D. Dousek, M. Komanec, S. Zvanovec, Z. Ghassemlooy, and B. Ortega, "M-QAM transmission over hybrid microwave photonic links at the K-band," Opt. Express 27, 33745–33756 (2019).

[51] D.-N. Nguyen, J. Bohata, M. Komanec, S. Zvanovec, B. Ortega, and Z. Ghassemlooy, "Seamless 25 GHz transmission of LTE 4/16/64-QAM signals over hybrid SMF/FSO and wireless link," J. Lightw. Technol. 37, 6040–6047 (2019).

[52] J. Bohata, M. Komanec, J. Spacil, R. Slavik, and S. Zvanovec, "Transmitters for combined radio over a fiber and outdoor millimeter-wave system at 25 GHz," IEEE Photonics J. 12(3), 1–14 (2020).

[53] L. Vallejo, B. Ortega, J. Bohata, S. Zvanovec, and V. Almenar, "Photonic multiple millimeter wave signal generation and distribution over reconfigurable hybrid SSMF/FSO links," Opt. Fiber Technol. 54, 102085 (2020).

[54] H. Zhang, L. Cai, S. Xie, K. Zhang, X.Wu, and Z. Dong, "A novel radio-over-fiber system based on carrier suppressed frequency eightfold millimeter wave generation," IEEE Photonics J. 9(5), 1–6 (2017).

[55] K. Kanta, A. Pagano, E. Ruggeri, M. Agus, I. Stratakos, R. Mercinelli, C. Vagionas, P. Toumasis, G. Kalfas, G. Giannoulis, A. Miliou, G. Lentaris, D. Apostolopoulos, N. Pleros, D. Soudris, and H. Avramopoulos, "Analog fiber-wireless downlink transmission of IFoF/mmWave over in-field deployed legacy pon infrastructure for 5G fronthauling," J. Opt. Commun. Netw. 12(10), D57–D65 (2020).

[56] C. H. d. S. Lopes, E. S. Lima, L. A. M. Pereira, R. M. Borges, A. C. Ferreira, M. Abreu, W. D. Dias, D. H. Spadoti, L. L. Mendes, and A. C. S. Junior, "Non-standalone 5G NR fiber-wireless system using FSO and fiber-optics fronthauls," J. Lightwave Technol. 39(2), 406–417 (2021).

[57] Y. Alfadhli, P.-C. Peng, H. Cho, S. Liu, R. Zhang, Y.-W. Chen, and G.-K. Chang, "Real-time FPGA demonstration of hybrid bidirectional MMW and FSO fronthaul architecture," in Optical Fiber Communication Conference (2019), paper W2A.39.

[58] P. T. Dat, A. Kanno, K. Inagaki, F. Rottenberg, J. Louveaux, N. Yamamoto, and T. Kawanishi, "High-speed radio-on-free-space optical mobile fronthaul system for ultra-dense radio access network," in Optical Fiber Communication Conference (2020), paper W2A.37.

[59] L. Vallejo et al., "Impact of Thermal-Induced Turbulent Distribution Along FSO Link on Transmission of Photonically Generated mmW Signals in the Frequency Range 26–40 GHz," in IEEE Photonics Journal, vol. 12, no. 1, pp. 1-9, Feb. 2020, Art no. 5500309, doi: 10.1109/JPHOT.2019.2959227.

[60] M. A. Khalighi and M. Uysal, "Survey on free space optical communication: a communication theory perspective," IEEE Commun. Surveys Tuts., vol. 16, no. 4, pp. 2231–2258, Oct.–Dec. 2014.

[61] J. Libich and S. Zvanovec, "Influences of turbulences in near vicinity of buildings on free-space optical links," IET Microw. Antennas Propag., vol. 5, no. 9, pp. 1039–1044, 2011.

[62] L. Vallejo, D. N. Nguyen, J. Bohata, B. Ortega, and S. Zvanovec, "M-QAM signal transmission at the photonically generated K-band over thermal-induced turbulent FSO links with different turbulence distributions," Appl. Opt. 59, 4997-5005 (2020)

[63] D.N. Nguyen, L. Vallejo, J. Bohata, B. Ortega, Z. Ghassemlooy, S. Zvanovec, "Wideband QAM-over-SMF/turbulent FSO downlinks in a PON architecture for ubiquitous connectivity", Optics Communications, Volume 475, 2020, https://doi.org/10.1016/j.optcom.2020.126281.

[64] J. Bohata, D. N. Nguyen, J. Spáčil, M. Komanec, B. Ortega, L. Vallejo, Z. Ghassemlooy, and S. Zvánovec, "Experimental comparison of DSB and CS-DSB mmW formats over a hybrid fiber and FSO fronthaul network for 5G," Opt. Express 29, 27768-27782 (2021)

[65] L. Vallejo, B. Ortega, J. Mora, D.-N. Nguyen, C. Guerra, J. Bohata, J. Spacil, S. Zvanovec, Demonstration of M-QAM OFDM bidirectional 60/25 GHz transmission over 10 km Fiber, 100 m FSO and 2 m radio seamless heterogeneous fronthaul link, Optical Fiber Technology, Volume 77, 2023, https://doi.org/10.1016/j.yofte.2022.103161.

[66] J. Kreissl, V. Vercesi, U. Troppenz, T. Gaertner, W. Wenisch, M. Schell, Up to 40- Gb/s Directly modulated laser operating at low driving current: buried-heterostructure passive feedback laser (BH-PFL), IEEE Photon. Technol. Lett. 24 (5) (2012) 362–364.

[67] D.-N. Nguyen, L. Vallejo, V. Almenar, B. Ortega, P. T. Dat, S. T. Le, J. Bohata, and S. Zvanovec, "Full-duplex transmission of multi-Gb/s subcarrier multiplexing and 5G NR signals in 39 GHz band over fiber and space," Appl. Opt. 61, 1183-1193 (2022).

[68] G. Qi, J. Yao, J. Seregelyi, S. Paquet, C. Belisle, X. Zhang, K.Wu, and R. Kashyap, "Phase-noise analysis of optically generated millimeterwave signals with external optical modulation techniques," J. Lightwave Technol. 24, 4861–4875 (2006).

[69] J. Bohata, D. N. Nguyen, J. Spáčil, M. Komanec, B. Ortega, L. Vallejo, Z. Ghassemlooy, and S. Zvánovec, "Experimental comparison of DSB and CS-DSB mmW formats over a hybrid fiber and FSO fronthaul network for 5G," Opt. Express 29, 27768–27782 (2021).

[70] L. Vallejo, J. Bohata, J. Mora, S. Zvanovec and B. Ortega, "Remote mmW photonic local oscillator delivery for uplink down-conversion in DML-based optical hybrid C-RAN fronthaul," in *Journal of Optical Communications and Networking*, vol. 15, no. 6, pp. 357-366, June 2023, doi: 10.1364/JOCN.482085.

[71] ETSI, "5G; NR; Base station (BS) conformance testing Part 2: Radiated conformance testing," 3GPP TS 38.141-2, version 15.8.0, Release 15 (2021).

[72] L. Vallejo, J. Mora, D.-N. Nguyen, J. Bohata, V. Almenar, S. Zvanovec, and B. Ortega, "On the 40 GHz remote versus local photonic generation for DML-based C-RAN optical fronthaul," J. Lightwave Technol. 39, 6712–6723 (2021).

[73] ITU-R, Resolution ITU-R 56-3: Naming for International Mobile Telecommunications," 2023.

[74] ITU-R, "Report ITU-R M.2516-0: Future technology trends of terrestrial International Mobile Telecommunications systems towards 2030 and beyond," Nov. 2022.

[75] ITU-R, "Recommendation ITU-R M.2083-0: IMT Vision – Framework and overall objectives of the future development of IMT for 2020 and beyond," Sep. 2015.

[76] G. Interdonato, E. Björnson, H. Q. Ngo, P. Frenger, and E. G. Larsson, "Ubiquitous cell-free massive MIMO communications," EURASIP J. Wireless Commun. Netw., vol. 2019, no. 1, pp. 1–13, Dec. 2019.

[77] Delga, and L. Leviandier, "Free-space optical communications with quantum cascade lasers," in Proc. SPIE 10926, p. 1092617, (2019).

[78] X. Pang et al., "11 Gb/s LWIR FSO Transmission at 9.6 µm using a Directly-Modulated Quantum Cascade Laser and an Uncooled Quantum Cascade Detector," OFC'22, Th4B.5.

[79] M. Han et al., "Long-Wave Infrared Discrete Multitone Free-Space Transmission Using a 9.15-µm Quantum Cascade Laser," IEEE Photonics Technology Letters, vol.35, pp. 489-492, 2023.

[80] M. Joharifar et al., "8.1 Gbps PAM8 Long-Wave IR FSO Transmission using a 9.15-µm Directly-Modulated QCL with an MCT Detector," OFC'23, Th1H.1.

[81] 3GPP, TS 38.104 V16.7.0: "NR Base Station (BS) radio transmission and reception," Apr. 2021.

[82] 3GPP, TS 38.141-1 V16.7.0: "NR, Base Station (BS) conformance testing, Part 1: Conducted conformance testing," Apr. 2021.

[83] T. W. C. Brown, D. A. Humphreys, M. Hudlicka, and T. H. Loh, "Prediction of SINR using BER and EVM for massive MIMO applications," in Proc. 12th Eur. Conf. Antennas Propag., 2018, p. 5.

[84] Hasan, M.K.; Chowdhury, M.Z.; Shahjalal, M.; Nguyen, V.T.; Jang, Y.M. Performance Analysis and Improvement of Optical Camera Communication. Appl. Sci. 2018, 8, 2527.

[85] S. R. Teli, S. Zvanovec and Z. Ghassemlooy, "Optical Internet of Things within 5G: Applications and Challenges," 2018 IEEE International Conference on Internet of Things and Intelligence System (IOTAIS), Bali, Indonesia, 2018, pp. 40-45.

[86] Z. Ghassemlooy, L. N. Alves, S. Zvanovec, and M.-A. Khalighi, Visible light communications: Theory and Applications (2017).

[87] P. Luo et al., "Experimental Demonstration of a 1024-QAM Optical Camera Communication System," in IEEE Photonics Technology Letters, vol. 28, no. 2, pp. 139-142, 15 Jan.15, 2016.

[88] P. Chavez-Burbano, V. Guerra, J. Rabadan, and R. Perez-Jimenez, "Optical camera communication for smart cities," in 2017 IEEE/CIC International Conference on Communications in China (ICCC Workshops), Qingdao, China, 22 October 2017, pp. 1–4.

[89] P. Chavez-Burbano, S. Vitek, S. R. Teli, V. Guerra, J. Rabadan, R. Perez-Jimenez, and S. Zvanovec, "Optical camera communication system for Internet of Things based on organic light emitting diodes," Electron. Lett. 55, 334 (2019).

[90] V. Matus, E. Eso, S. R. Teli, R. Perez-Jimenez, and S. Zvanovec, "Experimentally Derived Feasibility of Optical Camera Communications under Turbulence and Fog Conditions," Sensors, 2020, 20(3):757.

[91] L.-D. Guo, M.-J. Cheng, and L.-X. Guo, "Visible light propagation characteristics under turbulent atmosphere and its impact on communication performance of traffic system," In Proceedings of the 14th National Conference on Laser Technology and Optoelectronics (LTO 2019), Shanghai, China, 17 May 2019; p. 1117047.

[92] V. V. Nikishov, and V. I. Nikishov, "Spectrum of Turbulent Fluctuations of the Sea-Water Refraction Index," Int. J. Fluid Mech. Res. 2000, 27, 82–98.

[93] A. Islam, M. T. Hossan, and Y. M. Jang, "Convolutional neural network scheme–based optical camera communication system for intelligent Internet of vehicles," Int. J. Distrib. Sens. Netw. 2018, 14, 1550147718770153.

[94] E. Eso, A. Burton, N. B. Hassan, M. M. Abadi, Z. Ghassemlooy, and S. Zvanovec, "Experimental Investigation of the Effects of Fog on Optical Camera-based VLC for a Vehicular Environment," In Proceedings of the 2019 15th International Conference on Telecommunications (ConTEL), Graz, Austria, 3–5 July 2019; pp. 1–5.

[95] J. Bohata, S. Zvanovec, T. Korinek, M. M. Abadi, and Z. Ghassemlooy, "Characterization of dual-polarization LTE radio over a free-space optical turbulence channel," Appl. Opt. 2015, 54, 7082–7087.

[96] E. Eso, Z. Ghassemlooy, S. Zvanovec, J. Sathian, M. M. Abadi, O. Younus, Performances of Vehicular Visible Light Communications under the Effects of Atmospheric Turbulence with Aperture Averaging, Sensors, vol. 21, issue 8, pp. 1-17, 2021.